ABSTRACT

Title of Dissertation: EMERGENT NETWORK ORGANIZATION IN LINEAR AND DENDRITIC ACTIN NETWORKS REVEALED BY MECHANOCHEMICAL SIMULATIONS

Aravind Chandrasekaran,
Doctor of Philosophy, 2021

Dissertation directed by: Professor Garegin Papoian
Department of Chemistry and Biochemistry

Cells employ networks of filamentous biopolymers to achieve shape changes and exert migratory forces. As the networks offer structural integrity to a cell, they are referred to as the cytoskeleton. Actin is an essential component of the cellular cytoskeleton. The organization of the actin cytoskeleton is through a combination of linear and branched filaments. Despite the knowledge of various actin-binding proteins and their interactions with individual actin filaments, the network level organization that emerges from filament level dynamics is not well understood. In this thesis, we address this issue by using advanced computer simulations that account for the complex mechanochemical dynamics of the actin networks. We begin by investigating the conditions that stabilize three critical bundle morphologies formed of linear actin

filaments in the absence of external forces. We find that unipolar bundles are more stable than apolar bundles. We provide a novel mechanism for the sarcomere-like organization of bundles that have not been reported before. Then, we investigate the effect of branching nucleators, Arp2/3, on the hierarchical organization of actin in a network.

By analyzing actin density fields, we find that Arp2/3 works antagonistic to myosin contractility, and excess Arp2/3 leads to spatial fragmentation of high-density actin domains. We also highlight the roles of myosin and Arp2/3 in causing the fragmentation. Finally, we understand the cooperation between the linear and dendritic filament organization strategies in the context of the growth cone. We simulate networks at various concentrations of branching molecule Arp2/3 and processive polymerase, Enabled to mimic the effect of a key axonal signaling protein, Abelson receptor non-tyrosine kinase (Abl). We find that Arp2/3 has a more substantial role in altering filament lengths and spatial actin distribution. By looking at conditions that mimic Abl signaling, we find that overexpression mimics are characterized by network fragmentation. We explore the consequence of such a fragmentation with perturbative simulations and determine that Abl overexpression causes mechanochemical fragmentation of actin networks. This finding could explain the increased developmental errors and actin fragmentation observed *in vivo*. Our research provides fundamental self-assembly mechanisms for linear and dendritic actin networks also highlights specific mechanochemical properties that have not been observed earlier.

EMERGENT NETWORK ORGANIZATION IN LINEAR AND DENDRITIC ACTIN NETWORKS REVEALED BY MECHANOCHEMICAL SIMULATIONS

by

Aravind Chandrasekaran

Dissertation submitted to the Faculty of the Graduate School of the
University of Maryland, College Park, in partial fulfillment
of the requirements for the degree of
Doctor of Philosophy
2021

Advisory Committee:

Professor Garegin Papoian, Chair/Advisor

Professor Arpita Upadhyaya. Dean's representative

Professor Christopher Jarzynski

Dr. Pratyush Tiwary

Dr. Edward Giniger

Dedication

To the women in my family, Gowri Sundaram, Jayalakshmi Sundaresan, Annapoorna Visalakshi Sundaram, and Vaidehi V. Chandrasekaran, on whose grit, and sacrifices, rests my future doctoral privilege.

Acknowledgments

There are many people I need to thank for helping me reach this point in my academic career. To my adviser, Garyk Papoian, it has been an honor and a privilege to work under your guidance. During my time, I have learned a lot about viewing biology through the lens of physics. I have also had the opportunity to develop and work on original ideas, and I greatly appreciate the independence you give to our lab members.

I want to thank Edward Giniger for his support and mentorship. I have learned to appreciate the complexity and diversity in biological phenomena from you. I am always amazed at your acumen to parse complex biological data searching for meaningful, physically relevant patterns.

I would like to thank my committee members, Prof. Arpita Upadhyaya, Dr. Edward Giniger, Prof. Christopher Jarzynski, and Dr. Pratyush Tiwary, for graciously volunteering their time to assist with my defense.

I would like to thank all the Papoian lab members: Haoran Ni, Carlos Floyd, Mary Pitman, and alumni Qin Ni, Hao Wu, James Komianos, Haiqing Zhao. I learned a lot about academic research and scientific rigor from you guys. Thank you for being there whenever I needed feedback or assistance to get over bottlenecks. I will miss the evenings spent playing Mahjong. I wish you all the best and cannot wait to see what the future offers us all.

To the faculties and staff at the University of Maryland and the people who make the NCI-UMD partnership possible. I thank the Physics of Living Systems

network for creating a space for graduate students to engage in thoughtful discussions and meaningful collaborations to expand our understanding of the biophysical world. I would like to thank Prof. Arpita Upadhyaya for organizing the POLS-SRN and the Biophysics seminar series, Prof. Amy Mullin, Dr. Pratyush Tiwary, and Prof. Dorothy Beckett for engaging with the Chemistry graduate students in questions about career, research, and graduate life.

To the wonderful fellow graduate students, I met at UMD, particularly Onur Kara and Samuel Cohen. Thank you for being a sounding board for ideas around science and career.

Special thanks to my masters' advisor, Prof. Lee-Wei Yang, for believing in me and giving me the opportunity to learn the basics of scientific research. My master's in Taiwan helped me grow as a student, researcher, and human being. Thank you for teaching me the process of scientific thought and inquiry.

I would like to thank my friends from undergrad. Particularly Dr. Ashwin Ravichandran for always being there to discuss polymers, career, and life. I would like to thank the pragmatic Dr. Sriram Vignesh, and the meticulous Dr. Swaminath Bharadwaj for helping me hop out of the frustrated energy minima that I so often find myself in. My graduate career would have been impossible without you guys. Special mention to Dr. Srinivasan Raman, who played a key role in my academic career.

This will not have been possible without my family away from home, soon-to-be-doctor Teodora Kljaic, Brandon Bedford, Yasin Bin Rahmatullah, Saravana Rajakumar, and Dr. Leonardo Martinez-Diaz. Thank you for celebrating my successes,

consoling me in distress, and enjoying my company. You all mean the world to me. Thank you, Leo, for being a rock in my life.

Finally, this would not have been possible without my family, who supported me throughout. To my parents, Annapoorna Visalakshi Sundaram, Chandrasekaran Sundaresan, thank you for teaching me the value of hard work and perseverance. To my sister Vaidehi Chandrasekaran for constantly inspiring me to reach for the skies. You paved the way for me to walk on. I thank you all for the support you have given me.

Table of Contents

List of Tables

List of Figures

List of Abbreviations

in vivo	In the living – in organisms
in vitro	In the glass – in the lab environment
in silico	In silicon – performed on a computational framework
G-actin	Globular actin (Monomeric)
F-actin	Filamentous actin (Polymeric)
ATP	Adenosine triphosphate
ADP	Adenosine diphosphate
Arp2/3	Actin-related protein 2 and 3 complex
WASP	Wiskott-Aldrich Syndrome Protein
AFM	Atomic Force Microscopy
MEDYAN	Mechanochemical Dynamics of Active Matter
RDME	Reaction-Diffusion Master Equation
NMII	Non-muscle myosin II
Ena	Enabled
Mena	Mammalian Ena
DEna	Drosophila Ena
VASP	Vasodilator-stimulated phosphoprotein
Abl kinase	Abelson tyrosine kinase
Rac	Ras-related C3 botulinum toxin substrate
Rho	Ras homolog family member
Cdc42	Cell division control protein 42
TSM1 neuron	Twin sensilla of the margins neuron

Chapter 1 Introduction and background

Filamentous proteins that can dynamically polymerize and depolymerize are ubiquitous in all domains of life, providing both structural and functional stability to cells. Complex, interlinked networks of such filamentous proteins and other components span the cellular cytoplasm from cell membrane to nucleus and are referred to as the cytoskeleton. Just as the skeletal system provides support and shape to an organism, the cytoskeleton is essential for cellular morphology and functions. Cytoskeleton offers dynamic and adaptive features to the cell by enabling shape changes, intracellular transport, and cellular motility. Advances in experimental techniques such as super-resolution microscopy have enabled a tremendous wealth of knowledge on the structural features of various cytoskeletal components and their functional importance. Despite this, fundamental gaps remain in our understanding of the mechanisms by which individual cytoskeletal components come together to form various functional higher-order architectures. This dissertation investigates the organizational principles behind linear and dendritic actin networks through computer simulations. We find the necessary conditions for a stable bundle of linear actin filaments and look at the impact of branching nucleation on network morphology. Finally, we find the emergent network behavior resulting from a critical signaling pathway that throttles the balance between linear and dendritic actin filaments to ensure axonal growth and stability.

The introduction is organized into five main sections. I start by introducing the readers to the beautiful complexity of the actin cytoskeleton and highlight the different molecules that mechano-chemically interact either with individual actin filaments or a pair of actin filaments. Second, I would introduce the biological emergent structures and the necessary signaling cascades that sustain and alter such biological actin structures.

How do we faithfully model such a complicated system? To address this, I will introduce the computational framework used in this dissertation and the sustained improvements made towards simulating cell-scale networks. I will end the introduction by outlining the subsequent chapters of the thesis.

1.1. Actin cytoskeleton – a brief overview

The eukaryotic cell is made of complex, dynamic structures with specific functional roles. While the essential genetic information in DNA is securely modularized inside the nucleus, the mitochondria acts as the energy production hub of the cell, and the plasma membrane envelopes and protects the cell from the exterior. Additionally, a critical class of scaffolding proteins, consisting primarily of actin, microtubule, and intermediate filaments, collectively referred to as the cytoskeleton, plays a crucial role in mechanotransduction, maintaining cell shape and function. Among the cytoskeletal components, actin represents the most functionally diverse and well-understood class of substructures. The actin cytoskeleton plays a vital role in cellular processes migration, growth, cell division, and wound healing.

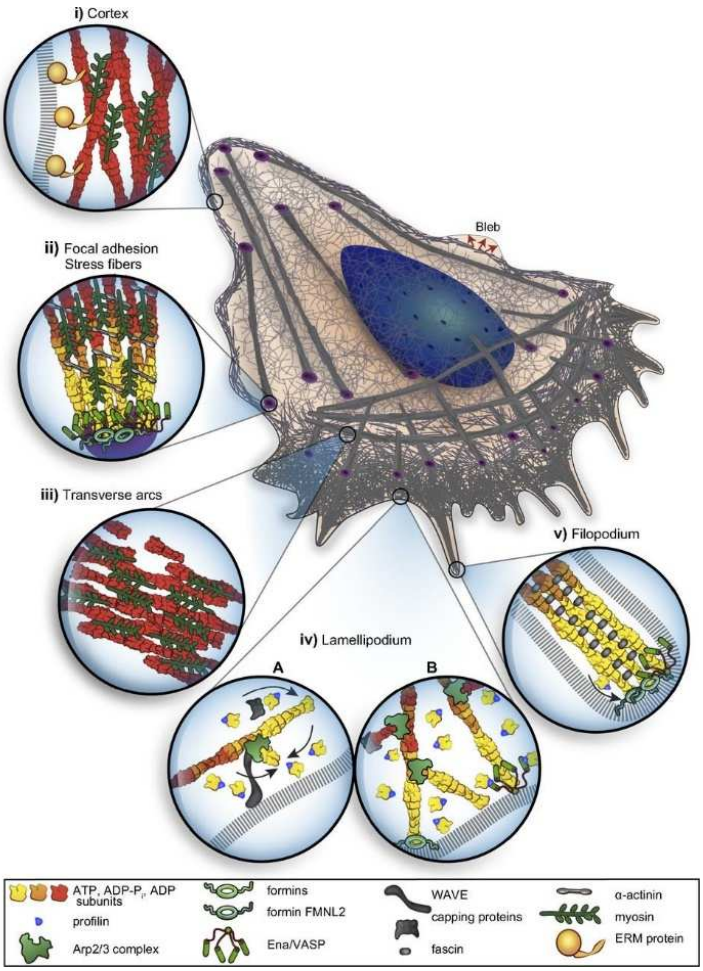

Figure 1-1 Actin architecture in a migrating cell. The cartoon shows a rendition of a cell with actin filaments shown in gray. Zoomed insets show various salient emergent network architectures such as actin i) cortex, ii) stress fibers along with focal adhesions, iii) transverse arc stress fibers, iv A and B) dendritic lamellipodial networks, and v) filopodium. Actin, along with relevant actin-binding proteins, is rendered within each inset. The legend at the bottom shows various components of the actin cytoskeleton. Figure reprinted from [1], with permission from The American Physiological Society.

Actin filaments are polymeric, semi-flexible assemblies of actin monomers. Actin filaments have a persistence length of ~17μm and a diameter of ~7nm.[2] Actin filaments assemble and disassemble readily in response to cellular signals and enable the cells to mount a quick response to changes in the extracellular environment. Figure

1-1 shows key actin architectures that have been recognized both *in vitro* and *in vivo*. Actin filaments can be bundled together by accessory proteins called crosslinkers to enable small, finger-like protrusions called filopodia at the leading edge of a spreading cell. Filaments can form branched architecture and organize into fan-shaped networks called lamellipodia to generate protrusive forces from actin polymerization. Also, long bundles of actin filaments called stress fibers aid in mechanotransduction and migration in certain cells. How are such diverse network states achieved with spatial and temporal precision? What mechanisms does the cell use to modify the network level organization of actin? We address these questions in this overview of the actin cytoskeleton.

1.1.1 Filament level organization of actin – chemical and mechanical aspects

Actin is ubiquitous in all living cells dating back to common ancestors of life such as bacteria and archaea.[3] Actin is extremely conserved among eukaryotes with minor sequence variation. This level of conservation is partly due to the limitations posed by the conditions required to form actin-actin interactions to form stable polymeric filaments.[4] Actin is the most abundant protein in a cell, contributing up to 10% of total proteins. Actin filaments are polymers of monomeric G-actin arranged in a double helical fashion. Actin monomers are arranged with a rotation of 166^{o} per molecule (short pitch) and an axial translation of 2.75nm resulting in 13 monomers per 6 turns of the helix.(long pitch) [5,6]

1.1.1.1 Linear actin filaments

Spontaneous polymerization of actin into filaments happens once the monomers form stable trimers. While ATP-bound dimers dissociate at 10^6 s^{-1}, trimers dissociate at a rate of 100 s^{-1}. As the number of monomers in the filament increases further, the dissociation reaction becomes asymmetric at both ends and is ~1s^{-1}. The kinetic data suggest that the formation of dimer and trimer limits the *de novo* nucleation. The differences in association and dissociation rates of actin to the ends of actin filaments that are longer than a trimer make actin a polar molecule. The filament ends are distinguished structurally as the minus/pointed end and the plus/barbed end. This chirality lends to an essential steady-state characterized by net depolymerization of actin filaments in the minus ends depolymerize in time while the actin filaments in the plus end polymerize in time. The structural basis for the kinetic differences was obtained by comparing the contacts made by the DNAse-I loop and the hydrophobic plug of the monomer. Within a given filament, the DNAse-I loop from monomer P and the hydrophobic plug loops form P-1form contacts with monomer P+1. Contrasting this with the pointed end, the DNAse-I loop of monomer P-1 instead interacts with the hydrophobic plug of monomer P. This difference poses additional enthalpic rearrangement cost when a monomer P+1 is added to the plus end. Additionally, barbed ends lack such inter-subunit contacts. Such contact differences explain the slow dissociation rate and association rate for actin at the pointed end. The absence of these interactions in the barbed end explains the faster dissociation and association rate in the barbed end. Why are inter-monomer contacts different between the two ends? The

ATPase activity of actin can explain this facet. ATP-bound filamentous actin (F-actin) readily dephosphorylates ATP to form ADP and Pi. The ADP.Pi bound state has a half time of 350s.[3] As the filament grows and reaches a steady-state, the minus end of the filament is rich in ADP.Pi bound actin while the barbed end is rich in ATP bound actin.

1.1.1.2 Dendritic nucleation of actin filaments

While linear filament organization is crucial for long-range force transmission in a cell, alternate mechanisms are also employed to produce carpets of actin filament networks. Branched filament organization is a key mechanism where new filaments are nucleated on the sides of preexisting filaments. These branches are at a 70^{o} angle with the parent filament.[7] Spontaneous branching ability helps the cytoskeleton reinforce mechanical elements where needed and also helps maintain a polarized architecture of filaments. Arp2/3 is the key branching nucleator and crucial for cellular processes such as cellular motility, clathrin-mediated endocytosis[8], and axonal guidance.[9,10]

It is interesting to note that Arp2/3 evolved from eukaryotic actin through a divergent evolution process.[11] There are 11 commonly known variants of Arp and are named based on their sequence divergence from actin. Arps share the same folds as actin, and the residues that bind to ATP are conserved. While Arp4-Arp9 complexes have chromatin-modifying functions, Arp2 and Arp3 form an important Arp2/3 complex. The other five subunits are made of proteins ArpC1, ArpC2, ArpC3, ArpC4, and ArpC5. The nucleation of an offspring filament requires specific interactions between subunits Arp2 and Arp3, which are absent in the native state rendering the complex inactive.[12,13] Activation of Arp2/3 requires nucleation promotion factors

(NPFs) such as Wiskott-Aldrich syndrome protein (WASp). [14,15] These NPFs share a key domain called the VCA domain consisting of verprolin(V) homology (or WASp homology 2 or WH2), hydrophobic central (C), and acidic (A) regions. Arp2/3 binding to 2 VCAs triggers conformational changes that render Arp2/3 active.[16] While the exact mechanism of branch nucleation is still an active area of research,[17] substantial evidence favors the nucleation scheme shown in Figure 1-2. [13]

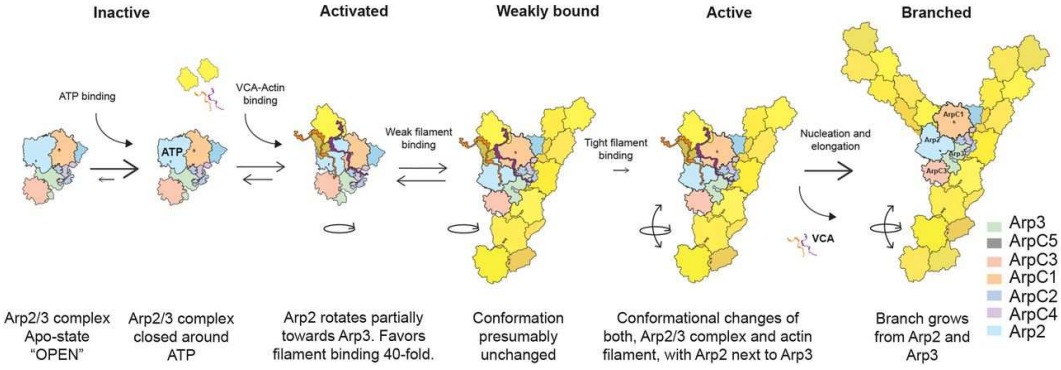

Figure 1-2 Mechanism of branched nucleation by Arp2/3. The seven Arp-related proteins that form the Arp2/3 complex are shown. ATP and proteins containing the VCA domain bind to activate the Arp2/3 complex. This enables binding to parent filament. Subsequent conformational changes enable contacts between Arp2 and Arp3 subunits, thereby triggering nucleation of offspring filament. Figure reprinted from [13] with permission from the Proceedings of the National Academy of Sciences.

NPF binding to Arp2/3 causes conformational changes that bring Arp2 closer to Arp3. Binding of Apr2/3-NPF to actin filament triggers further conformational changes to the complex. Finally, the V region of VCA bound to Arp2 and Arp3 has a high affinity to actin monomers. The binding of actin to the V region reduces the activation barrier to nucleation as the Arp2/3-actin complex mimics the nucleation trimer, thereby nucleating an offspring filament. Subsequent actin monomer addition causes elongation of offspring filament.

1.1.2 Linear actin Nucleators

The cytoskeleton also employs other nucleators that can form linear actin filaments without nucleating on the side of a parent filament. Out of such linear nucleators, formin is the most widely studied and most abundant one. Formin dimers stabilize dimers of actin, thereby lowering the energy barrier for the nucleation of filaments. Formin nucleates through interactions of the two formin homology domains, FH1 and FH2.[18] Also, formin is known to act as processive polymerase, which aids in the elongation of actin filaments.[1] In addition to Arp2/3, many more linear actin nucleators share the WH2 homology domain, namely Spire, Cobl, and Liemodin. Spire proteins, first found in Drosophila, have two human isoforms, namely Spire 1 and Spire2.[19] Spire consists of four WH2 domains and promotes nucleation by stabilizing tetramers of actin. There are pronounced lag times before Spire-driven nucleation occurs, suggesting rate-limiting mechanisms in the formation of dimers.[20] Cobl, a vertebrate-specific nucleator, contains three WH2 domains. Cobl has a high nucleation efficiency that can rival the nucleation rates of Arp2/3. Both Cobl and Spire are restricted to the brain. Unlike Cobl, and Spire, Leiomodin nucleates filaments by stabilizing the pointed end and does so through a single WH2 domain. Additionally, Leiomodin also has a tropomyosin binding domain highlighting a collaborative mechanism of actin nucleation.[21,22]

1.1.3 Filament length modifiers

Just as formins, there are other processive polymerases that enhance filament elongation. Another well-known processive polymerase family of proteins is Enabled/Vasodilator-stimulated phosphoprotein (VASP). They consist of three key domains, namely EVH1 (Ena/VASP homology 1), poly-proline repeat domain, and EVH2 domain. EVH1 targets Ena to focal adhesion proteins, while the proline-rich domain targets Ena to several signaling proteins such as Abl, Src, and IRsp53. The EVH2 domain consists of F-actin and G-actin binding domains. Finally, the C-terminal EVH2 domain also has a coiled-coil domain involved in the tetramerization of Ena/VASP. Tetramerization is crucial for the processive polymerase activity of Ena/VASP proteins.[23,24] Each of the four actin-binding domains in tetrameric Ena can bind to filament barbed ends, sides of filaments, or G-actin monomers.[24,25] In the G-actin bound state, Ena increases the local concentration of actin around a filament tip enabling processive polymerase activity.[26] Ena's ability to bind to sides of filaments is crucial to stabilize confined bundles of actin filaments from destruction.[27] Ena can also interact with profilin-actin taking advantage of multiple G-actin pools in the cytoplasm.[28]

Ena kinetically competes for actin barbed ends with specialized barbed end stabilizing proteins called Capping proteins.[26,29–31] Capping proteins are dimers that bind to barbed ends of filaments and stabilize them from chemical perturbations. Capping proteins are present in micromolar concentrations in the cytoplasm. As a result, most barbed ends in the cytoplasm are capped and stabilized for a long time as

the dissociation half-time is ~30min for capping bound filament barbed ends.[3] Similarly, pointed ends of filaments are stabilized by tropomodulin.[32] It is also important to note that, Arp2/3 can also be considered a minus-end stabilizing protein.

Actin filaments can be destabilized by severing proteins that sever filaments in two. Cofilin and gelosin are the two commonly known severing proteins. Cofilin binds cooperatively to the sides of actin filaments. Upon binding, cofilin-actin interactions force the flat actin monomer to rotate by 30^{o}. This changes the helical configuration by reducing the rotation angle between two monomers to 162^{o} (from 167^{o}). Additionally, the long pitch is changed from 13 monomers per 6 turns to 10 monomers per 6 turns.[33] These changes make the filament more flexible, eventually leading to destabilization due to local stress accumulation.

1.1.4 Monomeric-actin binding proteins – the brake pedal to attenuate actin assembly

Even though actin nucleation is not very favorable, once nucleated, spontaneous actin polymerization occurs rapidly, bringing the reservoir of unpolymerized actin to the barbed end critical concentration (the value is 0.1μM for linear actin networks). As cells contain anywhere in the few tens to hundreds of micromolar actin [7,34], the majority of actin would be polymerized under this paradigm, reducing the leverage for fast remodeling of the network. In contrast, about half of the total actin in cells is in the unpolymerized state.[3] These differences can only be accounted for by actin monomer binding proteins that bind to diffusing actin (G-actin) and sequester it to prevent

polymerization. Profilin (~16kDA) and thymosin-β4(~43aa) are the most common G-actin binding proteins. The relative abundance of these two proteins is dependent on cell types.[3,35] Both profilin and thymosin-β4 compete for G-actin in cells [36], reducing the pool of actin available for polymerization. Thymosin-β4 is found in the 100-500μM range, and its affinity to ATP- and ADP- actin is characterized by dissociation constant (K_d) 0.1-3.9, and 80-100 μM, respectively.[37–40] Profilin is known to have a cellular concentration of 8.4μM, while other studies point to a range anywhere between 14 and 100% of total actin.[41,42] Profilin-actin interaction has a K_d of 0.1 and 0.17 μM for ATP- and ADP- bound forms.[43] Thus, ADP bound actin is mostly sequestered by profilin. ADP-profilin has an accelerated nucleotide exchange rate (exchanging ADP for ATP), which then lends for the competition from thymosin-β4 (similar K_d values).[44]

The competition between profilin and thymosin-β4 also alters actin filament dynamics. While thymosin-β4 bound G-actin cannot be added to filaments, profilin bound G-actin monomers can be added to filament barbed ends but not the pointed ends.[45] Thus filament elongation rate can be accelerated selectively at the barbed ends leading to polarized growth. Profilin-actin also competes with diffusing G-actin by selectively favoring specific actin modifying proteins. Recent evidence also suggests that profilin-actin does not participate in dendritic nucleation by Arp2/3 [46,47]. Instead, filament proteins like VASP and formin require profilin-actin for effective elongation.[24,48–50] Recently, Ca^{2+}-Calmodulin-dependent protein kinase II (CamKII), a dodecameric

synaptic protein, has been found to bind actin filaments. It has been known to inhibit actin polymerization suggesting a role for G-actin sequestration.[51]

1.1.5 From filaments to networks – the role of filament-filament interactions in determining actin network architecture

So far, we have discussed several aspects of the cytoskeleton that affect the properties of individual actin filaments. There are other actin-binding proteins, which can bind to two actin filaments simultaneously, resulting in actin gels or bundles.[52] These crosslinker molecules bind two actin filaments separated by 10s of nm length scales to couple them kinetically and alter the viscoelastic properties of the network. Such crosslinkers play a key role in force amplification. For example, filaments can produce piconewton range of forces from leveraging actin polymerization.[53] These forces are short-lived as sustained elongation of filaments causes buckling of filaments (longer than 0.7μm). Such buckling events reduce the force transmission from polymerization. However, cross-linked bundles can produce forces of larger magnitude by increasing the collective stiffness of the network.[54,55] Crosslinker proteins consist of two actin-binding domains that share calponin homology[56], but there is a great deal of diversity in the distance between the domains. For example, in Fascin, actin-binding domains are separated by about 10nm, while in the case of α-actinin, it is between 30 and 40nm. Filamin has a larger separation of about 160nm.[57,58] The nature and level of crosslinking also alter the viscoelastic behaviors observed *in vitro*. If the crosslinks are less likely to unbind (very low $K_{d,}$ e.g., scruin, heavy muscle meromyosin), the viscous

behavior of the cytoskeleton is diminished, and the networks behave as elastic solids.[59] An increase in the dissociation rate of crosslinkers leads to viscous response at higher frequency strain rates. Additionally, crosslinker unbinding allows local relaxation of stress in the network, suggesting that crosslinkers act as dissipative elements. Such changes could help the actin cytoskeleton in tuning its viscoelastic response by behaving as rigid elastic solids under deformations that act on the short timescales while behaving as viscous liquids at long time scales.

In addition to passive crosslinkers, ATP consuming myosins play a crucial role in key biological functions such as cytokinesis, wound healing, and muscle contraction. The key isoforms of myosins are myosin I, II, V, VI, and X.[60] All isoforms can catalyze the dephosphorylation of ATP but differ widely in structure and function. Out of the many isoforms, myosin II is of particular interest consisting of sub-classes such as non-muscle, skeletal muscle, cardiac muscle, and smooth muscle myosins. These myosins are two-headed walkers (rather bipedal) that can polymerize to form bipolar filaments of myosins. Non-muscle myosins form bipolar filament consisting of 10-30 myosins and are referred to as minifilaments.[61] While individual myosin II molecules have a low affinity to actin, the bipolar filaments can bind and walk directionally towards the barbed (plus) ends on actin filaments with higher processivity.[62] Walking is achieved by a constant switch between weak and strong-binding states. While all isoforms produce similar forces and displacements per step, they vary significantly in their intermediary kinetic rates giving rise to functional diversity and spatial heterogeneity within a single cell.[63] Myosins have been shown to enable the

stress-stiffening behavior observed in crosslinked actin networks under large strain rates.[64] Thus, myosins also have a crucial role in conjunction with crosslinkers in altering the mechanical properties of the actin network through contraction, polarity sorting, and stress-driven network disassembly.

1.2. Emergent biological network architectures – structure, function, and signaling-driven control

To achieve directional motility, cells use two unique actin network organizations, namely linear and dendritic, to effectively mount traction forces on the extracellular medium. The two have their advantages. Linear actin filaments can be organized as bundles that aid in the focused transmission of forces over long distances. On the other hand, dendritic actin networks can be effective when cells also require displacements over large length scales. It is important to point out that this division of labor is not without significant overlap, i.e., cell migration is due to a combination of forces generated by linear and dendritic actin networks.[65] This section outlines the biological relevance of linear actin stress fibers (explored in Chapter 2), dendritic actin networks (studied in Chapter 3). Finally, we provide the contexts in which cooperation between these two network organizations is essential (examined in Chapter 4).

1.2.1 Linear actin networks – Stress fiber bundles

The most studied bundled actin structure is the filopodia. They are finger-like projections formed of linear actin filaments that are bundled together by crosslinkers

such as fascin.[1] Filopodia play a vital role in helping the cell explore the extracellular environment to determine the optimal direction of migration. Typical filopodial protrusions are ~100nm in diameter and range up to a couple of microns in length. Electron microscopic images have shown that the filopodial protrusions emerge from the underlying lamellipodial dendritic network, which we will explain below.[66] A subset of lamellipodial filaments grows longer than the average (~100nm) to initiate protrusions against the membrane. This process happens in a fascin independent manner.(Figure 1-3A) Subsequent crosslinking by fascin causes the long filaments to segregate into bundled configuration.[65] The sustained elongation of filopodia by the filopodial tip complex includes linear polymerases such as Ena/VASP family proteins known to aid in the formation of filopodial protrusions.

Stress fibers are another major class of actin bundles that have received renewed attention recently thanks to high-resolution microscopy techniques.[67] These bundled actin structures are found in cultured fibroblasts and endothelial cells.[68] Stress fibers consist of 10-30 actin filaments bundled together with crosslinkers or crosslinkers and myosins. As actin filaments are polar, the resulting bundle can be unipolar (both barbed and pointed ends are clustered), apolar (no specific orientational preference for the filaments), graded polarity (net polarity of bundle changes along the bundle axis), and sarcomeric (pointed ends are clustered, shown in Figure 1-3C). Stress fiber bundles are anchored through focal adhesions to the substrate at either one or both ends. Depending on the nature of the bundles, there are three main classes of actin stress fibers, namely dorsal, ventral and transverse arcs (Figure 1-3B).[69] Dorsal stress fibers form near the

leading edge of the cell from focal adhesions. Focal adhesions are rich in formin nucleators which result in the formation of unipolar bundles that are crosslinked by α-

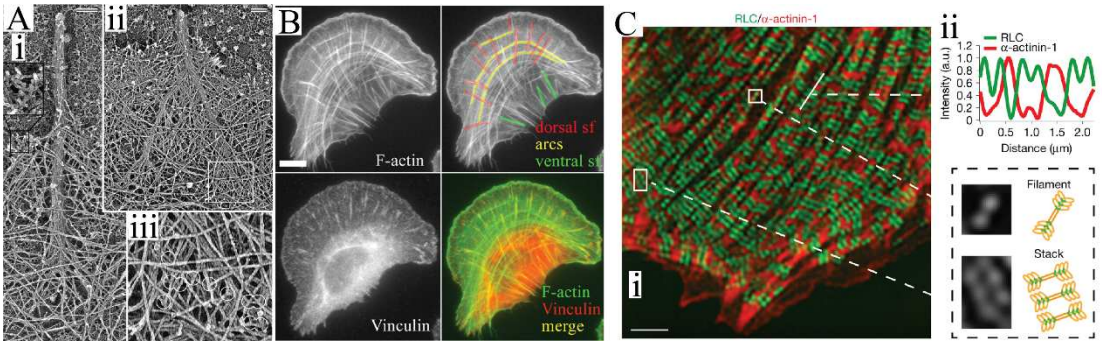

Figure 1-3 Figure shows key actin architectures formed from linear actin filaments A) Platinum Replica electron micrograph shows filopodia emerging from underlying dendritic, lamellipodial network in B16F1 melanoma cells. i) Filopodia diffuses and merges into the surrounding network. ii) Figure shows recently formed filopodia made of two bundles that are spliced together. iii) The box shown in panel ii is enlarged to show the dendritic architecture of actin filaments (branching points highlighted as green circles). Bar=0.2μm. B) TIRF microscopy images of U2OS human osteosarcoma cells spreading on the fibronectin-coated surface. Focal adhesions and F-actin were visualized using anti-vinculin and phalloidin stains. The top right panel shows dorsal, transverse arc, and ventral stress fibers in red, yellow, and green. Bar=10μm C) Structured illumination microscopy images of REF52 cells on the fibronectin-coated surface reveal spatial localization of α-actinin and myosin along with a stress fiber. Staining is achieved by simultaneously coexpressing α-actinin-1-mCherry (red) and TLC-GFP (green). Zoomed insets show local abundances of myosin. Panel Cii) Line scans along the white line in panel Ci reveal striated spatial localization patterns for myosin and α-actinin. Scale bar = 2μm. Panel A: Republished from [66] with permission of Rockefeller University Press; permission conveyed through Copyright Clearance Center, Inc.Panel B: Republished from [69] with permission of Rockefeller University Press; permission conveyed through Copyright Clearance Center, Inc. Panel C: Reprinted from [70] by permission from Springer Nature: Nature Cell Biology.

actinin but are devoid of myosin molecules. Both transverse arcs and ventral stress fibers are formed of graded polarity bundles and are decorated by periodic bands of α-actinin and myosin resembling the sarcomeric organization found in muscle fibers.[71] The stress fibers span tens of microns in length and are made of filaments of diverse filament lengths. Thus the sarcomeric organization is achieved by the local ordering of filaments where the pointed ends are clustered together by myosin and the crosslinkers

interact with the barbed end rich regions of the sub-structure (Figure 1-3C).[70] While these are major contractile elements in certain cell types in stiff substrates, stress-fiber free migration mechanisms have been observed in cells such as *Dictyostelium discoideum* amoeba and leukocytes.[72,73] While we understand the structural organization of the stress fibers, we do not fully understand the self-organization mechanism of such sarcomeric bundles. Chapter 2 explores this by studying the requirements for forming stable actin bundles of unipolar, apolar, and sarcomere-like organization.

1.2.2 Dendritic actin network

Lamellipodia and actin cortex are the two commonly studied dendritic actin networks. The actin cortex is formed of short actin filaments that are tethered to the plasma membrane. These short filaments are crosslinked by α-actinin and motor proteins. The viscoelastic properties of this network help control cell shape and volume against osmotic pressure. Under the cortical layer, Arp2/3 driven networks form lamellipodial protrusions that leverage forces from actin polymerization to generate migratory forces against the extracellular medium. Such structures consist of crosslinkers and myosins and play a crucial role in forming filopodial protrusions, as described earlier.[74] Lamellipodial dynamics involves a spatially heterogeneous organization of actin modifiers with Arp2/3 and Capping cooperating to promote filament assembly at the leading edge and severing proteins promoting filament disassembly towards the back.[74,75] While the organization of such quasi-two-

dimensional networks has been well studied, the three-dimensional organization of dendritic networks is still lacking. In contrast, the spatial organization of linear actin networks has been explored by a series of *in vitro* experiments with purified components such as crosslinkers and myosins. To understand the complex organization of the cellular cytoskeleton, we need to understand the roles of Arp2/3 and other proteins in sub-micron actin organization. In Chapter 3, we investigate the role that Arp2/3 plays in actin organization and find that excess branching activity leads to network fragmentation.

1.2.3 Growth cones - cooperation between linear and branched actin architecture

During neuronal development, nerve cells project axons over large distances to initiate neuronal patterning. Growth cones are specialized cytoskeletal structures found in the tips of growing axons. Growth cones sense and respond to soluble extracellular cues. Such cues can be attractive or repulsive. Thus, the growth process of the axon is a chemically guided search process that is steered by changes to the cytoskeleton. These structures are rich in actin and microtubule (Figure 1-4). Trans-membrane proteins sense extracellular cues and respond by activating a cascade of proteins that alter the structure of the cytoskeleton. The exact nature of the signaling cascade is challenging to ascertain, given that most upstream signals target multiple actin-binding proteins.

Neuronal development in the Drosophila wing is initiated by pioneer neurons that traverse the embryonic imaginal wing disc tissue to reach the wing base.[76] This

process initiates a cascade of subsequent growth processes of several other axons that fasciculate near the wing disc base to form two key nerve fibers L1 and L3, to interface with the central nervous system.[77,78]

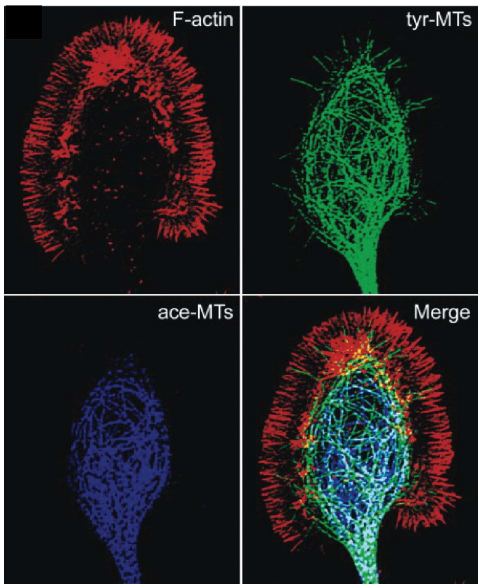

Figure 1-4 Distribution of cytoskeletal actin and microtubule filaments in growth cones. A. Hippocampal neuron growth cone was fixed and stained for actin, acetylated microtubules, and tyrosinated microtubules. B. Reprinted form [79], with permission from Elsevier.

Actin and microtubule have been known to play a critical role in the axonal growth process by orchestrating a coordinated growth response to biochemical signals. Biochemical evidence suggests that Abelson non-tyrosine receptor kinase (Abl) is a key signaling protein that controls growth cone motility and guidance. Abl signaling affects growth cone architecture by promoting branched filament organization while inhibiting the processive linear polymerase, Enabled (Ena). Such bifurcated signaling pathways have been recognized in other organisms; for example, in Listeria, motility is ensured by a balance between Arp2/3 and VASP.[80] Given the impact of Abl

signaling in growth cones, cooperation between nucleation and elongation has been an area of growing interest.[81] Chapter 4 explores the effect of the Abl signaling pathway in axonal architecture and proposes arguments based on changes to actin network architecture that explain the properties of growth cones measured experimentally under wild-type and overexpressed conditions.

1.3. MEDYAN: an active matter simulation platform

This section is partly adapted from Aravind Chandrasekaran, Arpita Upadhyaya, and Garegin A. Papoian. "Remarkable structural transformations of actin bundles are driven by their initial polarity, motor activity, crosslinking, and filament treadmilling" ***PLOS Computational Biology*** *15(7): e1007156 (2019).*[82]

MEDYAN is a mechanochemical force field for simulating active matter, including cytoskeletal networks. It deeply integrates chemical and transport dynamics with network mechanics, treating these phenomena on equal footing. MEDYAN has emerged from earlier efforts to model actin bundle growth in filopodia [83–87], where both active and passive transport was shown to influence growth dynamics [117,119,120] critically. MEDYAN's time evolution protocol is based on alternating reaction-diffusion and mechanical equilibration steps, where the one-time events are stochastically generated according to the *next reaction method* [88], while the conjugate gradient approach is used to achieve mechanical equilibration [89]. This propagation scheme takes advantage of the wide timescale separation between slow chemical processes and fast mechanical equilibration speeds within sub-micron length

scale volumes containing a portion of an actin network [90]. Furthermore, MEDYAN can effectively model actin filament polymerization processes and explicit α-actinin (crosslinker), myosin minifilament (motor) binding, and unbinding events in addition to myosin walking and mechanochemical feedbacks such as catch and slip bond behaviors (Figure 1-5).

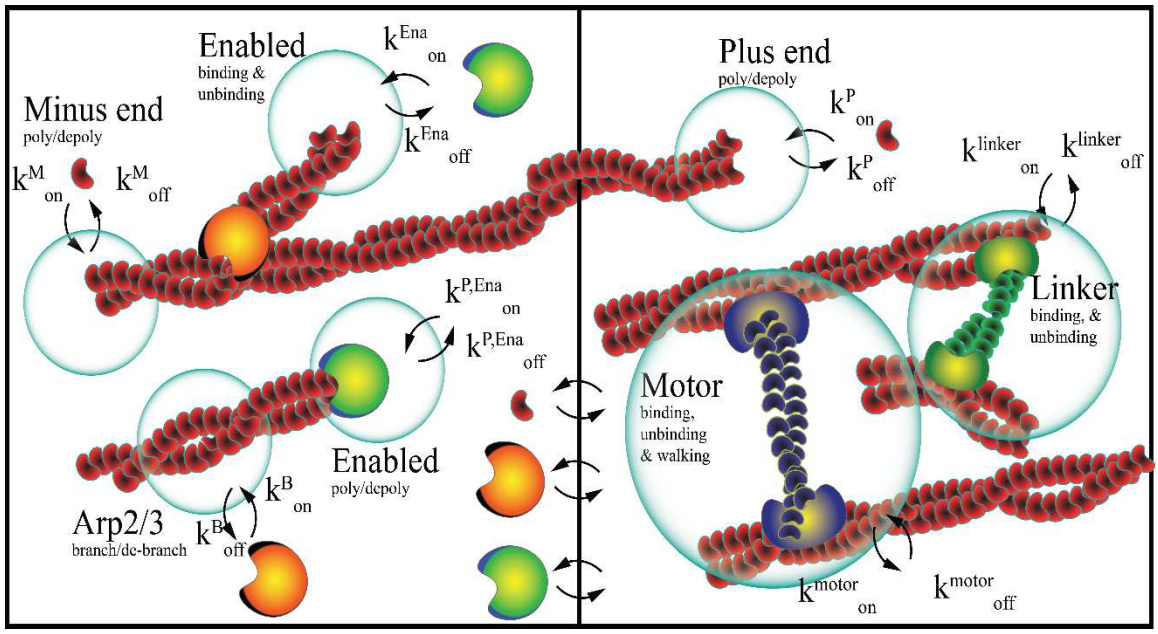

Figure 1-5 Schematic shows reaction and diffusion events that are modeled in studies discussed in this dissertation. A simplified view of chemical events in MEDYAN is shown in a two-compartment model. Diffusion reactions are modeled as species transfer reactions between neighboring compartments. Reactive events are modeled according to propensities calculated in their local environment (each compartment). For example, actin polymerization on the filament end circled in the right compartment only depends on the number of G-actin monomers available within the compartment.

In contrast to MEDYAN, other cytoskeletal modeling strategies, such as Cytosim (Cytoskeletal Simulation) [91,92], AFINES (Active Filament Network Simulation) [93], and the model by Kim and coworkers [94] rely on the Langevin dynamics of cytoskeletal components, explicitly simulating thermal undulations at the

expense of significant diminution of computational efficiency. Among these models, MEDYAN's treatment of general reaction-diffusion processes is most comprehensive (particularly regarding G-actin's diffusion and reactions). MEDYAN's mechanical potentials are the most elaborate, for example, having an analytical excluded-volume potential representing steric repulsions and complex dihedral angle potentials at the dendritic actin network branch points (Figure 1-7). A detailed comparison of different cytoskeletal modeling approaches can be found in Popov et al. (particularly, see Table S1 of [89]).

In MEDYAN, the reaction volume is divided into voxels based on the Kuramoto length [89,95]. Diffusing molecules are assumed to be uniformly mixed within each voxel and diffuse from one voxel to another. Actin filaments can polymerize and depolymerize from both plus and minus ends based on experimentally determined rate constants [96]. Filaments that polymerize towards the boundary experience a reduction in polymerization rate based on the Brownian ratchet model [97]. In MEDYAN, the growing propensity for an actin filamentous tip is based on the local, instantaneous concentration of diffusing G-actin in the tip's neighborhood [89], while, in comparison, actin filaments grow/shrink at a constant rate in Cytosim, [98]. Furthermore, MEDYAN can explicitly account for ATP, ADP.Pi and ADP bound actin monomeric states, enabling more elaborate simulations of F-actin polymerization dynamics [99,100]. In summary, filament length fluctuations and filament treadmilling can be studied using MEDYAN at the resolution of a single actin monomer. As elaborated below, we found that these fluctuations play an important role in

determining whether the bundle stays coherent or undergoes a morphological transformation.

The most common method to represent a reaction network such as one described above is by a series of differential equations coupled with one another based on continuously varying concentrations of reacting species. However, this approach fails in biologically relevant cases as the concentration of reacting species reduces extremely low values. Hence, we resort to a stochastic framework based on the number of each species to represent N reactions based on mesoscopic reaction constants (c_μ, $\mu \in [1,N]$). Both stochastic and deterministic methods converge at the thermodynamic limit [247]. The set of all copy numbers of each reacting species ($\{X_j\}$, $j \in [1,M]$) represents the instantaneous state of such a network of dimension M equal to the number of reacting species. One of the ways of solving such a network is to write a master equation [248,249]. Such methods often tend to be analytically intractable. Hence, Gillespie proposed a method [250] through which trajectories are obtained by picking the time and the reaction at random in each step based on a propensity (a_μ). The propensity is defined as, $a_\mu = \gamma_\mu c_\mu$, where γ_μ is the degeneracy in the number of ways the reaction could be executed. For example, in the case of $2A \rightarrow B$ with X_A copies of A, $\gamma = X_A(X_A - 1)/2$. Mesoscopic rate constant c_μ can be obtained from deterministic rate constant k_μ corresponding to a reaction of order n in a reaction volume V_r by, $c_\mu = k_\mu \left(\frac{V_r}{N_A}\right)^{n-1}$ where N_A represents Avagadro number. In this study, we use the *next reaction method* to simulate the actomyosin reaction network.

The *Next reaction method* [88], involves the following steps. Initially, both the time step τ_μ ($\tau_\mu = (1/a_\mu)ln(1/r_\mu)$) and propensity a_μ are calculated for each reaction where r_μ is a random number between 0 and 1. The reaction R with the smallest τ_μ is executed and the $\{a_\mu\}$ that depend on R alone are updated. This is made possible by the use of a dependency graph for the reaction network. Then, the reactions are efficiently sorted based on their τ_μ using an indexed priority queue data structure. This algorithm offers a significant reduction in computational complexity for the simulation of a reaction network. This method is used to simulate unipolar actomyosin bundles in this study.

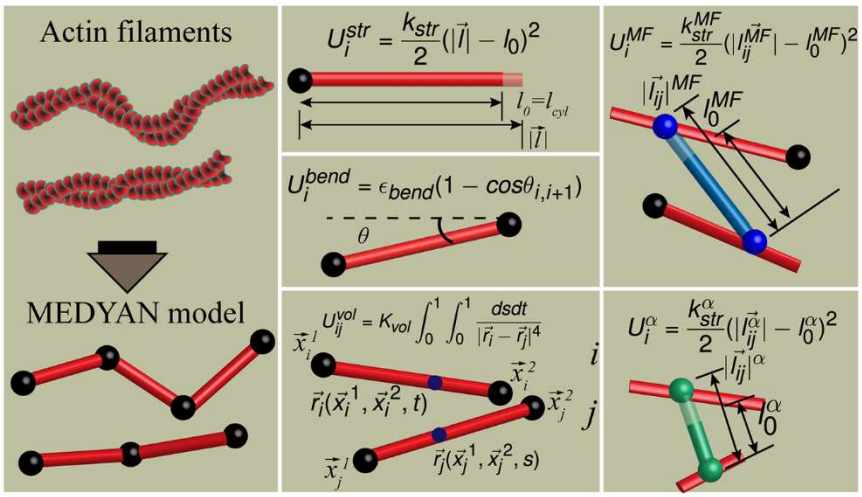

Figure 1-6 The mechanical model of actin, α-actinin and myosin minifilaments in MEDYAN. Double helix structure of actin filament is represented as a series of cylinders (red) connected together at hinges (black spheres). Stretching (U_i^{str}), bending (U_i^{bend}) and cylinder-cylinder excluded volume (U_{ij}^{vol}) interactions are elaborated. Crosslinkers (green) and myosin MF (blue) experience stretching potentials (U_i^{α} and U_i^{MF} respectively). More details are provided in the Methods section and the Supporting Methods (section 2).

In MEDYAN, mechanical modeling of actin filaments is based on cylinder units with equilibrium spacing $l_0^m \ll l_p$ (l_0^m= 108 nm in this study, l_p-persistence

length) connected with neighboring cylinders at flexible hinges. The persistence length of actin was reported from experiments as 17μm [101]. The MEDYAN force-field prevents filaments from passing through each other via a novel cylinder-cylinder repulsion potential that is analytical, in contradistinction to the more widely employed technique of other comparable force fields, which relies on finding the closest distance between two cylinders that is used to compute their mutual repulsion [89] (Figure 1-6). Various MEDYAN mechanical potentials, such as intra-cylinder stretching and inter-cylinder bending, are shown in Figure 1-6. α-actinin and myosin molecules bound to actin filaments are modeled as springs connecting two actin filament sites within their respective binding distances (α-actinin binding distance is in the range 30-40 nm, and minifilament binding distance is in the range 175-225 nm). For example, those Motor/crosslinker binding and unbinding are modeled as a single-step chemical reaction in MEDYAN. In contrast, in other force fields, such as Cytosim, these processes occur via two elementary steps, comprising separate reactions for each end of the motor or crosslinker [102]. Please refer to Figure 1-5 for more details on the chemical reaction events Figure 1-7 for mechanical interactions relevant to this dissertation.

In MEDYAN, crosslinker unbinding kinetics is modeled as a slip bond, while myosin unbinding kinetics is modeled as a catch bond based on the parallel cluster model [62]. A linear force-velocity relationship gives the motor walking rate for motor walking events. Further aspects of mechanical equilibration and mechanochemical

feedback loops in MEDYAN and the implementation details of the chemical model are provided in Appendix A, Supplementary Methods.

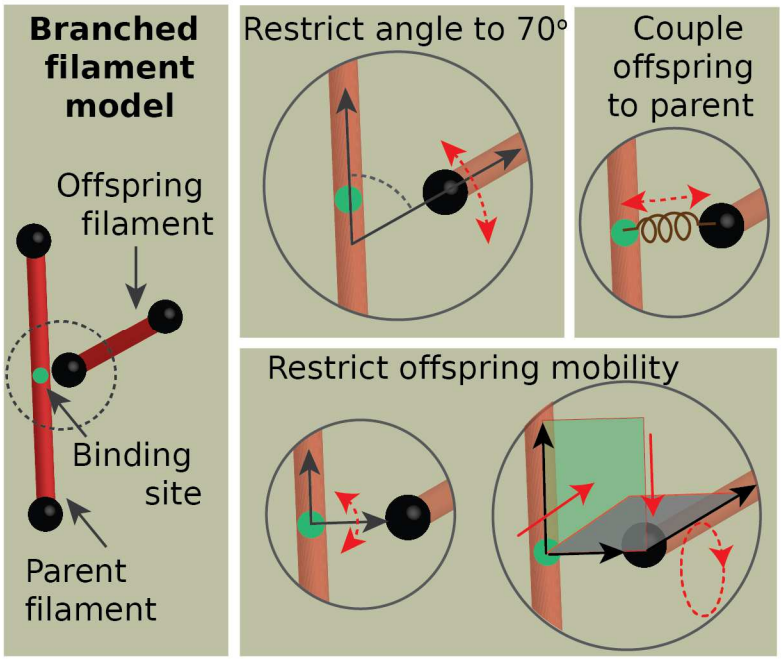

Figure 1-7 The mechanical model for a dendritic filament in MEDYAN. The figure shows a parent filament nucleating a daughter filament along its side at a particular binding site (green, filled circle). The panels to the right show the mechanical forcefield employed in MEDYAN to model essential features of dendritic filament architecture. Vectors considered for each potential are shown as black arrows. Red dotted lines with arrows show the degree of freedom that is restricted by the potential. A bending potential is used to restrict the angle between offspring and parent filament. Also, a harmonic stretching potential is used to couple the offspring filament to the parent filament. Position of the offspring pointed end, and the out-of-plane rotation of offspring filament is also restrained with suitable potentials.

The detailed modeling principles employed in MEDYAN reproduce essential features of active cytoskeletal matter such as contractility and treadmilling, but it comes with a computational cost. As a result, simulation of cell-scale complex reaction-diffusion networks of relevant time scales could not be achieved on single-core CPUs. We will see in Chapter 2 that MEDYANv3.2 also helps understand the stability and dynamics of actin bundles. To improve the performance of MEDYAN, we have made

significant algorithmic improvements and memory optimizations to take advantage of data locality in the new version, MEDYAN4.2 (employed in Chapters 3 and 4). In addition, we have also added SIMD algorithms were needed to accelerate the performance further. Table 1-1 shows the number of monomers and the projected time to generate 1000s of trajectories in the two versions of the MEDYAN codebase. Taken together, MEDYAN4.2 is 6-30x faster depending on system size and complexity (Table 1-1). To enable simulation of longer time scales, we have also implemented a protocol to restart trajectories. This novel feature recreates the stochastic chemical reaction network with exact propensities and mechano-chemical dependencies, thereby improving the ability of MEDYAN4.2 to study the long-time scale dynamics of cytoskeletal networks. The simulations described in Chapters 3 and 4 benefit from this key feature to simulate large cytoskeletal networks to the 2000s timescale. Taken together, these efforts significantly improve the performance of MEDYAN taking us closer to our goal to simulate cell-scale networks. We also discuss further improvements required both from physical modeling and computational efficiency points of view to realize simulations of cell-scale networks.

System size		Time to simulate 10^3 s MEDYAN version		Speed up
Volume (μm^3)	# actin monomers (20μM)	v3.2	v4.2	v4.2 vs v3.2
1	1.2×10^4	11h	2h	5.5
8	9.6×10^4	6d, 16h	15h	11
27	3.2×10^5	55d, 6h	2d, 6h	25
125	1.5×10^6	373d, 14h	13d, 13h	28

Table 1-1 Table of wall time required to simulate 20μM actin networks with M: A=0.05, and α:A=0.01 for 10^3s. The table shows various cubic system sizes initialized with 20μM actin

(95% F-actin, 5% G-actin). The time required to generate 10^3s of trajectories was extrapolated from three trajectories, each lasting 5s. The expected wall time required is shown in days (d) and hours (h). Finally, the fold increase in computational efficiency is also shown.

1.4. Outline of Chapters

This thesis investigates the role of actin-binding proteins in the emergence of stable bundles and dendritic actin networks using computational simulations. MEDYAN, described in section 1.3, is the primary tool used to study the mechanochemical dynamics of actin networks. Additional modifications made to the model will be introduced in each chapter. Each chapter contains an Introduction, Methods, Results, and Discussion section.

What are the conditions under which stable actin bundles can be formed? To answer this, in Chapter 2, we study the role that crosslinker, myosin, and treadmilling play in the stability of bundles that are initially arranged in unipolar and apolar configurations. We find that myosin concentration is the primary determinant of the steady-state morphology of the bundles. Under excess myosin activity, bundles deform into radially-symmetric, aster-like configurations. We also see that excessive treadmilling can prevent effective crosslinking of filaments causing network fragmentation. Finally, we show that a delicate balance between filament treadmilling and myosin activity is required to stabilize sarcomere-like network architectures.

How does Arp2/3, the key branching nucleator, affect the sub-micron actin organization? We address this question by studying networks with varying levels of Arp2/3 in Chapter 3. We find that mechanosensitive Arp2/3 activity affects the filament length distribution of the dendritic network. Arp2/3 activity undermines the myosin-

driven contractility of the network by preventing force percolation through the network. This leads to stochastic network fragmentation at high Arp2/3 concentrations. We describe a novel mechanism of fragmentation where myosin activity dominates the network organization of actin initially, but Arp2/3 activity determines the steady-state network properties.

How does biochemical signaling affect the structure and dynamics of growth cones? Biochemical analyses on *Drosophila* growth cones reveal that the architecture of actin networks in growth cones involves an optimal balance between linear and dendritic actin networks by a critical signaling protein, Abl. Abl alters network architecture by simultaneously promoting Arp2/3 while inhibiting Enabled. As experimental limitations prevent imaging of individual actin filaments in Drosophila growth cones, we use MEDYAN to study the effect of Abl on actin architecture. We find that among the two downstream effectors of Abl, Arp2/3 and Ena, Arp2/3 is a stronger modulator of filament length and actin organization in growth cone mimics. Consistent with experimental observation, excess Abl activity causes network fragmentation. We try to understand the mechanochemical consequence of such a fragmented state by studying the mechanical and mechanochemical responses of the networks to perturbations. We conclude that spatial network fragmentation at Abl overexpression also hampers the mechanochemical properties of the network. We propose that the mechanochemical fragmentation observed *in silico* could explain the abnormal growth patterns observed *in vivo*.

Chapter 2 Remarkable structural transformations of actin bundles are driven by their initial polarity, motor activity, crosslinking, and filament treadmilling

This chapter is adapted from Aravind Chandrasekaran, Arpita Upadhyaya, and Garegin A. Papoian. "Remarkable structural transformations of actin bundles are driven by their initial polarity, motor activity, crosslinking, and filament treadmilling" ***PLOS Computational Biology*** *15(7): e1007156 (2019).*[82]

2.1. Introduction

Understanding emergent behaviors in the actin cytoskeleton is essential, since key biological functions such as cellular growth, division, and motility depend on cytoskeletal dynamics. Actin networks are transient and malleable within a single cell, constantly forming and remodeling various micro-architectures at different cellular locations. One salient class of such actin structures are actin bundles [68,103], which appear both in the cell body as stress fibers [69,104,105], or in specialized cellular processes such as filopodia [106–108], stereocilia [109–111], and microvilli [111–113]. The formation and functionality of bundles are spatially and temporally regulated by various proteins that interact with actin, including nucleation factors [69,114], crosslinkers [115,116], and molecular motors [117]. Depending on the cellular context and specific influence of actin regulatory proteins, different bundle structures emerge [118–120], with distinct functional roles as elaborated next.

First, due to individual actin filaments' polarity, an actin bundle may be unipolar, apolar, sarcomeric, or graded polarity (Appendix A, Figure A-1) [103], being tethered at either one or both ends via a cross-linker or a molecular motor. Cellular structures of unipolar bundles are ubiquitous across living cells: they aid in cytoplasmic streaming in pollen tubes [121–123] as well as in fungal hypha formation [124]. Unipolar bundles are found in animal cells in filopodia [125] and proximal dorsal stress fibers [69,71]. These structures are usually crosslinked but do not contain myosin as active crosslinkers *in vivo* [126]. However, there is evidence for myosin minifilaments, which are polymers of 10-30 myosin units [127], walking through tracks of unipolar bundles [128] under *in vitro* conditions. Non-muscle myosin II-A isoform minifilaments (NMII-A) [129] incorporate into dorsal stress fibers when these stress fibers are connected to transverse arcs [126]. Recently, NMI has also been implicated in filopodial force generation in neural growth cones [130]. Other actin bundle organizations, such as apolar bundles, underlie the portions of stress fibers near the cell center in fibroblasts [131], in sections of contractile rings [132,133], and sections of ventral and transverse stress fibers. Composite apolar bundles are mostly found as two unipolar precursor bundles interacting with one another due to filament sliding in response to NMII-A activity [128]. Finally, more finely organized polarity arrangements are found in sarcomeric ordering, which has great significance in generating the contractility of stress fibers [68,103].

The large variety of actin fibers and their distinct functional roles have instigated a growing interest in how various factors, such as crosslinking activity and minifilament

concentrations, affect the dynamics and stability of bundles having unipolar and apolar organization. Another salient property of many actin bundles, namely, non-sarcomeric contractility [134–136], has also been a focal topic of experimental and computational studies. An agent-based model was employed by Zemel et al. to study one-dimensional unipolar and apolar bundles of 10μm length under different concentrations of motors moving according to prescribed force-velocity relations [137]. They found that apolar bundles readily undergo sliding motions resulting in internal sorting. However, the lack of spatial details in their model did not allow predictions of the stability of bundle morphology under the influence of myosin. Dasanayake et al. [138] simulated actin bundles of 10μm length, modeled in 2D, considering explicit filament stretching and bending in addition to minifilament stretching forces in a confined volume. They found that apolar bundles exert higher wall stresses than parallel filaments.

Nevertheless, it is still unclear how actin bundles behave at long time scales under a wide range of crosslinker and myosin concentrations, especially if they were to be modeled in three spatial dimensions. The latter point should be emphasized because studying actin bundles in 3D is crucial for reconciling with the phenomenology of bundles observed under *in vivo* cellular conditions. Recent studies in three dimensions by Kim and coworkers indicated that filament polarity plays an important role in bundle formation from disordered actin networks [139] and tension generation [94,139]. To shed further light on the mechanochemistry of actin bundles, in this work, we set out to establish the fundamental principles that govern the stability of two fundamental bundle organizations, namely, purely unipolar and apolar bundles.

Understanding conditions that either stabilize or destabilize various bundle geometries will shed light on the basic principles that govern the cytoskeletal organization, bringing insights into complex *in vivo* processes, such as cytoplasmic disassembly [140] and actin network turnover [141–143]. For example, the stability of untethered bundles is likely to depend on their internal polarity structure and crosslinker and myosin motor conditions. Furthermore, cells modulate actin filament turnover through a host of mechanisms such as filament severing [144–146], branching [52,103], and capping [23,147]. As a result, *in vivo* turnover rates are orders of magnitude faster than those commonly observed in *in vitro* experiments [145,148–150]. In general, actin turnover plays a critical role in the stress relaxation of entangled actin networks at longer timescales. For example, skeletal myosin is known to fluidize actin networks at very low mole ratios (myosin head to total actin mole ratio, M: A 0.0039) [151].

On the other hand, myosin‘s catch bond behavior can lead to long residence times, resulting in actin networks maintaining significant internal stresses at high myosin concentrations. Also, transient passive crosslinkers arrest network configurations and prevent relaxation. However, crosslinker unbinding events allow for slow reconfiguration dynamics [152,153]. The crosstalk between filament turnover and crosslinker mechanokinetics has not been comprehensively studied under a wide range of conditions. Hence, it is also necessary to explore the stability of bundles under a broad set of treadmilling rates.

To address the above-outlined problems, we have used MEDYAN (MEchanochemical Dynamics of Active Networks) mechanochemical force field [89] to study the stability and dynamics of untethered actin bundles under a diverse set of polarity arrangements and levels of α-actinin crosslinker, myosin minifilament, and treadmilling conditions. MEDYAN is further elaborated in the Methods section below. Our main finding is that unipolar bundles preserve bundle morphology at a broader range of crosslinker and myosin concentrations than apolar bundles—the latter experience morphological instability due to being more susceptible to myosin-induced intra-bundle filament sliding and shearing. We also show that three salient microarchitectures eventually emerge when simulating various untethered bundles under different conditions --- bundles, asters, and bundle-aster hybrids. Asters are filamentous networks exhibiting radial polarity sorting, with barbed ends clustered towards the aster center. We also investigated how the resulting phase diagrams depend on the speed of treadmilling. We found that network catastrophes, characterized by poorly crosslinked low-density networks with obscure morphologies, occur when crosslinking cannot keep up with filament extension. Overall, our studies demonstrate that while a stand-alone apolar bundle is stable under a significantly narrower set of conditions than unipolar bundles, this geometric arrangement can serve as an essential precursor to rich network remodeling phenomena such as global polarity sorting and sarcomeric organization.

2.2. Methods

Stochastic trajectories of actomyosin bundles were generated using MEDYAN, a mechanochemical forcefield developed in the lab. In MEDYAN, reactive species that are in/bound to the filamentous phase are modeled differently from the freely diffusing species. To achieve this multi-resolution description of actin networks, the reaction volume is divided into compartments of size 500nm, where the size of the cube was determined based on the rate of the fastest reaction (barbed end polymerization) in the system. The diffusing species such as unpolymerized actin (G-actin), unbound crosslinkers, and unbound myosins are defined at a spatial resolution of a single compartment. We assume uniform mixing of such species within any compartment, and so, such molecules lack spatial coordinates. Actin filaments, on the other hand, are explicitly modeled as beads connected by non-deformable cylinders. Filament polymerization and depolymerization reactions are defined at each end of the filament, and binding reactions for crosslinkers and myosins at different points along with the cylinders that form an actin filament.

Once the chemical species are defined on their respective spatial scales, stochastic trajectories are evolved using a variation of the Gillespie algorithm called the *next reaction method*.[88] As MEDYAN uses a spatially resolved Gillespie algorithm, mechanical costs are defined for each network configuration using forcefields defined in the Introduction of this dissertation. The mechanical stress accumulated due to chemical perturbations is periodically equilibrated, and new reaction rates are defined

based on the network configuration at mechanical equilibrium. These cycles of steps are iteratively solved to generate 2000s long trajectories of actin bundles.

Initial structures for all our simulations were based on 2 μm long actin bundles, comprising 30 actin filaments that correspond to *in vivo* stress fibers [131], where the internal arrangements of filament polarities were in either unipolar or apolar geometries. Filaments were initially placed on a hexagonal lattice with a spacing of 35 nm as found in experiments [154,155]. Bundles were modeled with α-actinin and NMIIA minifilaments that can bind and unbind from actin filaments. Bundles were simulated at 7 different concentrations of α-actinin (α-actinin to total actin mole ratio referred to henceforth as α:A 0.01, 0.05, 0.1, 0.25, 0.4, 0.6, 0.8) and 6 different concentrations of myosin (myosin head to total actin mole ratio referred to henceforth as M:A 0.0225, 0.045, 0.09, 0.18, 0.225, 0.675). Each 2000 seconds long, eight trajectories were generated for each of the 6x7=42 mole ratio pairs (α:A, M: A) studied. Besides, we also studied how the speed of filament treadmilling influences bundle stability. Myosin mole ratios of 0.0225 0.045, 0.225, and 0.675 were considered at α:A 0.01, 0.1, and 0.4 to investigate how all observed non-treadmilling morphologies behave under different treadmilling conditions. Treadmilling speed was varied by simultaneously altering polymerization and depolymerization rates at both filament-ends by the same factor χ. As a reference, χ=1.0 corresponds to the *in-vitro* treadmilling rate. We chose the following χ values (0.1, 0.3, 0.6, 1.0, 3.0, 6.0, and 10.0), hence mimicking treadmilling speeds that are slower and faster than the *in vitro* rate. As a technical detail, in this work, we have developed a flexible volume protocol that

permits expanding and contracting the reaction volume along the X-axis, which allows avoiding artificial boundary effects on the bundle's major axis in a computationally efficient manner. This technique is further elaborated in Supporting Information (Appendix A, Section A.9). 7 trajectories were generated for each combination of the myosin mole ratio, α-actinin mole ratio, and χ factor.

In order to understand the underlying morphologies sampled, we devised a hierarchical clustering scheme. To carry out structural clustering of obtained bundle configurations, we first computed the distributions of plus-end -- plus end (Dis^{++}), minus-end -- minus end (Dis^{--}), and plus-end -- minus end (Dis^{+-}) Euclidean distances. Jensen Shannon divergences [156] between each of the 42-mole ratios taken pair-wise were used to construct initial -condition-specific dissimilarity matrices (Appendix A, Figure A-12). The complete linkage method [157] results in a hierarchical cluster, which we visualized as dendrograms (shown below). Appendix A, Section A.5 provides further details on the clustering algorithm.

2.3. Results

2.3.1. Long timescale morphologies of actomyosin bundles are primarily determined by their initial polarity and the myosin concentration

A wide array of steady-state network morphologies emerge when non-treadmilling bundles with the initial unipolar organization (non-treadmilling-BUInit) and initial apolar organization (non-treadmilling-BAInit) were simulated under a broad set of α-

actinin and myosin concentrations (Figures 2-1 and 2-2). A trajectory is considered to have reached a steady-state when the network's radius of gyration reaches a stationary value (Appendix, Figure A-10). We found that for any combination of α-actinin and myosin ratios, marked differences are observed between steady-state network morphologies of apolar and unipolar bundles. More specifically, antiparallel filaments show a strong tendency to mutually slide in response to myosin activity due to the latter being unidirectional walkers. To quantitatively characterize the resulting network morphologies, we applied a novel structure-based clustering analysis that we have developed in this work (Appendix A, Section A.5), which revealed dominant network morphologies preferred under various conditions, as elaborated below.

The resulting dendrograms reveal three broad clusters closest to the root, colored in green, red and blue, pointing to three major network morphologies (Figures 2-3): bundle-like (BL), aster-like (AL), and aster-bundle intermediate (ABI) states. We also considered an alternative morphology classification technique based on network radial distribution devised by Freedman et al. [158] (see Appendix A, Figure A-3) and a combination of nematic order and shape parameters (see Appendix A, Figure A-2, and Supplementary Methods Section A.6 and A.7). Both order parameters delineated well the bundled morphologies from the aster-like morphologies. However, the hierarchical classification strategy introduced in this work was also able to identify the intermediate bundle-aster morphologies.

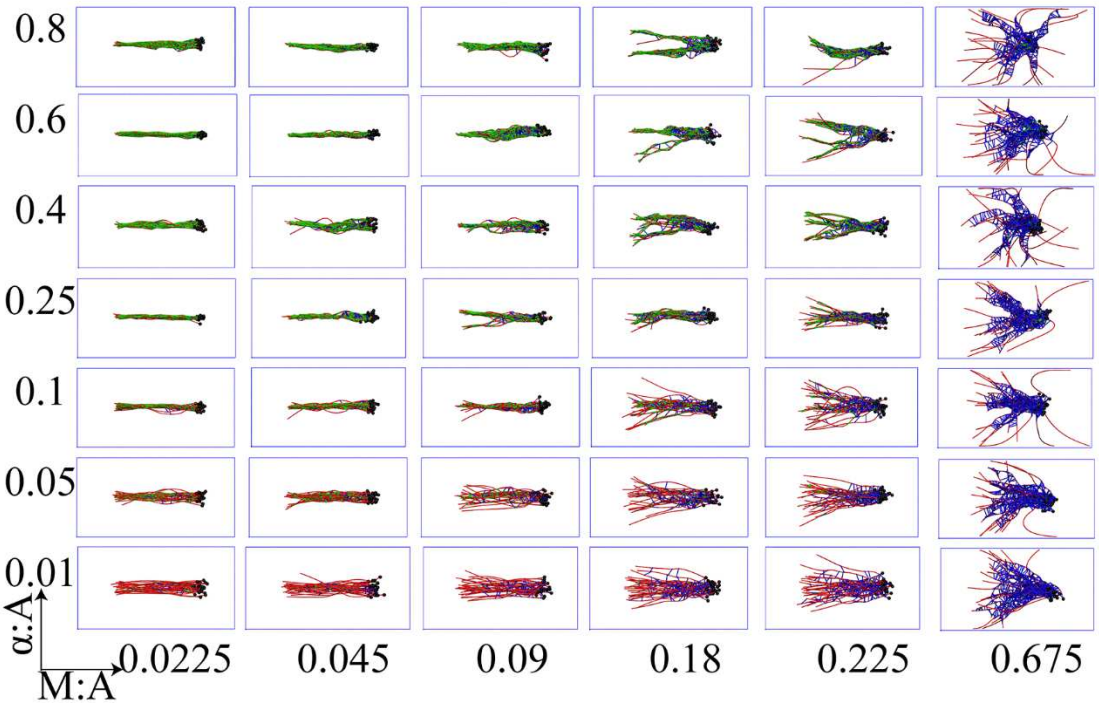

Figure 2-1 Representative snapshots show network morphologies from simulations of unipolar bundles under different crosslinker and myosin mole ratios with respect to the actin concentration. Each panel shows a steady-state network configuration of actin (colored in red) along with bound myosin minifilaments (blue) and α–actinin (green). Mole ratios of myosin and α-actinin with respect to actin are held at values mentioned along abscissa and ordinate of the grid, respectively.

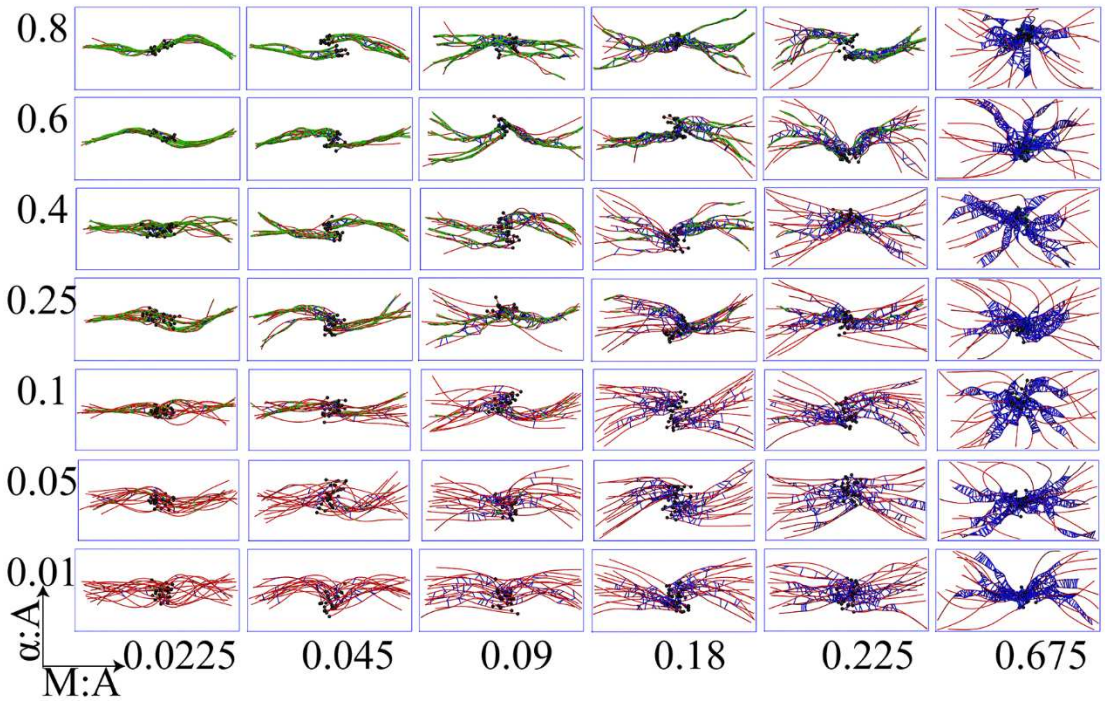

Figure 2-2 Representative snapshots show network morphologies from simulations of apolar bundles under different crosslinker and myosin mole ratios with respect to the actin concentration. Each panel shows a steady-state network configuration of actin (colored in red) along with bound myosin minifilaments (blue) and α–actinin (green). Mole ratios of myosin and α-actinin with respect to actin are held at values mentioned along abscissa and ordinate of the grid, respectively.

Some reflection on the internal structure of these dendrograms shows that within each initial polarity arrangement, NMIIA concentration is the primary driver of the resulting network morphology (see Figure 2-3). Specifically, the same highest level clusters are formed from configurations with similar M: A ratios, while finer-grained additional clustering is determined by other factors, such as the crosslinker (α-actinin) concentration. The effect of myosin is primary because, at high motor concentrations, inter-filament distances become significantly widened outside of the α-actinin binding compatibility zone of 30-40 nm. This, in turn, crucially depletes the network of

crosslinker binding sites (Appendix A, Figure A-4), hence, greatly diminishing parallel alignment among actin filaments and, subsequently, destabilizing the bundled phase.

It is interesting to compare our finding of the depletion of crosslinkers with increasing myosin concentration with the recent simulations that studied the sorting of two different crosslinkers along with an actin bundle. Freedman et al. have established that a significant length difference between two actin-binding proteins, when combined with a specific range of the filament bending moduli, can result in spatial sorting of crosslinkers along a bundle [159]. Here, we found that active myosin walking may significantly increase overall inter-filament separation, reducing the number of sites available for crosslinker binding in the bundles studied here, which presumably should have important implications for the sorting phenomenon in the presence of molecular motors.

When simulations were started with initial unipolar conditions, bundle-like states were stable when M: A $\leq$ 0.09 (21/42 cases = 50% of all M: A/α:A mole ratios studied). On the other hand, initial apolar arrangements result in stable bundle-like states only in ~20% (7/42) of the cases (i.e., when M: A = 0.0225). Thus, unipolar bundles are stable under a significantly more comprehensive range of conditions than their apolar counterparts. We tracked this difference primarily to myosin activity in apolar bundles giving rise to two thin polarities sorted sub-bundles that are together much longer than the initial bundle length and mutually interact via their barbed ends (see Figures 2-1, and 2-2). The resulting thinner bundles are more susceptible to bending deformations than the corresponding unipolar bundle.

Consequently, at the time scale of about 30 minutes probed in this work, unipolar and apolar bundles arrive at different metastable morphologies despite being under the same crosslinker and myosin conditions. Presumably, if these systems were to be ergodic, bundles are expected to eventually evolve to identical steady-state configurations regardless of the initial polarity arrangement. However, as shown in our previous works [160,161], cytoskeletal dynamics may be sufficiently glassy such that only metastable states are reachable over a laboratory timescale.

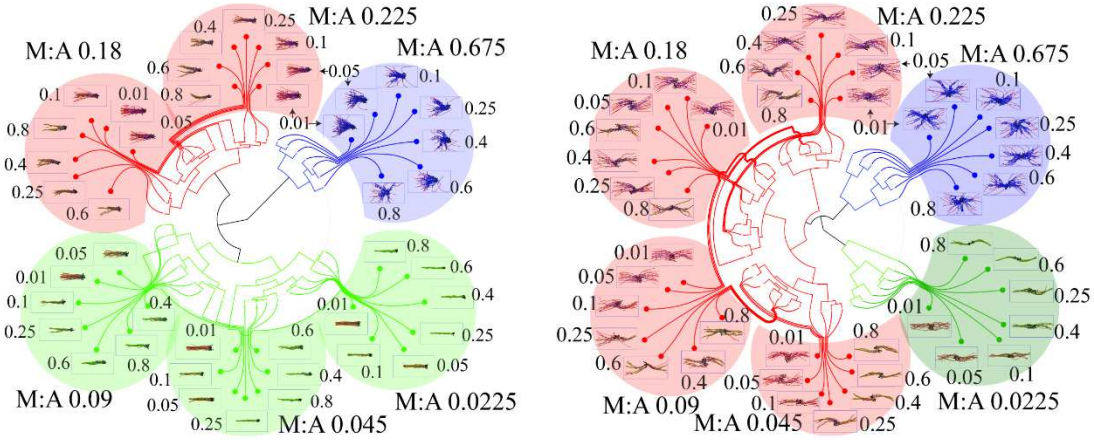

Figure 2-3 Dendrograms illustrating clustering of different resultant actin network morphologies from either unipolar (left) or apolar (right) bundle initial configurations. Distributions of distances between minus-minus, minus-plus, and plus-minus ends were used to construct dissimilarity matrices for both unipolar and apolar cases. Agglomerative cluster trees were encoded from the above-mentioned dissimilarity matrices and then drawn as dendrograms. The three largest clusters are shown in red, blue, and green, along with final representative snapshots. α:A values are indicated close to the snapshots, while M: A values are indicated for each sub-cluster. Clades corresponding to bundle-like configurations are colored in green, while aster-like configurations are colored in blue. Intermediate states that do not resemble either network morphologies are colored in red.

Under very high myosin activity (M: A = 0.675), both unipolar and apolar bundles undergo a morphological collapse, preferring radially symmetric aster-like structures (the last column in Figures 2-1, and 2-2). We note in passing that in cells, asters are

primarily found in microtubule networks as radially symmetric structures with filament plus ends spatially clustered together [162,163]. Actin networks are also expected to form radially polarity sorted asters [164]. Such structures have been found *in vitro* treadmilling actin networks subject to skeletal muscle myosin (M: A 0.1), fascin, and myosin [165] or just skeletal muscle myosin (M: A 0.02) alone [166,167], with the filament plus ends oriented towards the center of the aster.

The increased processivity of muscle myosin partly explains the difference in threshold myosin ratios between skeletal muscle myosin and NMIIA for the onset of aster-like structures. Actin asters were observed *in-vitro* when cytoskeletal structures were destabilized using Cytochalasin D [140]. Recently, they were shown to be essential in fission yeast cells during fusion [168,169]. Fission cell actin asters are considered to be formed due to Fus1 nucleators and multimerization of Myo51 and Myo52 [169]. Overall, we found that experimentally observed salient network morphologies of treadmilling networks can also be sampled in our simulations under non-treadmilling conditions.

2.3.2. Initial polarity arrangement plays a vital role in the evolution of the treadmilling bundle morphology

Next, we investigated the combined effect of network turnover and mechanokinetics (crosslinker and NMIIA) by including actin filament polymerization and depolymerization processes in bundle simulations analogous to the systems discussed above. In the treadmilling study, steady-state was defined when the average

filament length fluctuations reach their stationary values (Appendix A, Figure A-11). To systematically modulate filament treadmilling, we varied polymerization and depolymerization rates at both barbed and pointed ends by a factor χ between 0.1 and 10.0, where lower χ values correspond to slower treadmilling rates. We modeled a reaction volume having dimensions of 4 μm x 1.5 μm x 1.5 μm, with an initial total actin concentration of 5 μM, where the simulation box can expand and contract along the major axis based on the instantaneous bundle length (more details are provided in Appendix A, Supplementary Methods, Section A.9).

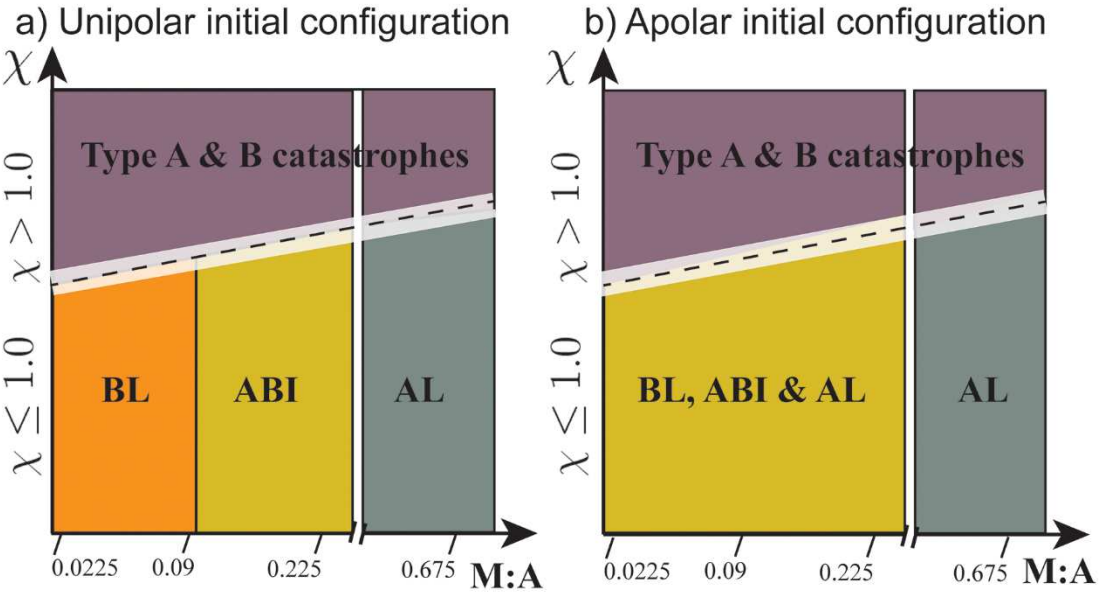

Figure 2-4 Schematic of preferred network morphologies under different values of the triad. Cartoon illustration of primary network morphologies of bundles expected in a) unipolar and b) initial apolar configuration at different ranges of the triad, namely χ=0, 0>χ≤1.0, and χ>1.0. Morphologies observed at discrete values of the triad and results from clustering (Appendix A, Figure A-4) were used to propose the map above. Colored voxels are used to represent distinct zones of preferred network morphologies expected. The dotted line represents uncertainty in the boundary. Dotted lines within white bands represent the crosslinker- and myosin-dependent boundaries between stable and unstable networks.

We investigated both unipolar and apolar bundles at M: A mole ratios of 0.0225, 0.09, 0.225, and 0.675, whereas α:A was sampled at 0.01, 0.1, and 0.4. These values were carefully chosen to capture the different salient network morphologies manifested under non-treadmilling conditions (non-treadmilling-BUInit and non-treadmilling-BAInit), namely, BL, AL, and ABI states. 7 trajectories, each 2000 seconds long, were generated for each of the 84 triad conditions (α:A, M: A, χ), starting from either unipolar (χ-BUInit) or apolar (χ-BAInit) initial conditions. Like non-treadmilling bundles, the classes of network morphologies mentioned above were determined by clustering trajectories from 84 triads using the same clustering protocol (Appendix A, Figure A-12). We classify connected networks with morphologies that do not belong to BL, AL, or ABI as either Type A catastrophes if the networks are fragmented into smaller clusters or Type B catastrophes, where filaments in the network are poorly connected (Appendix A, Figures A5-A9).

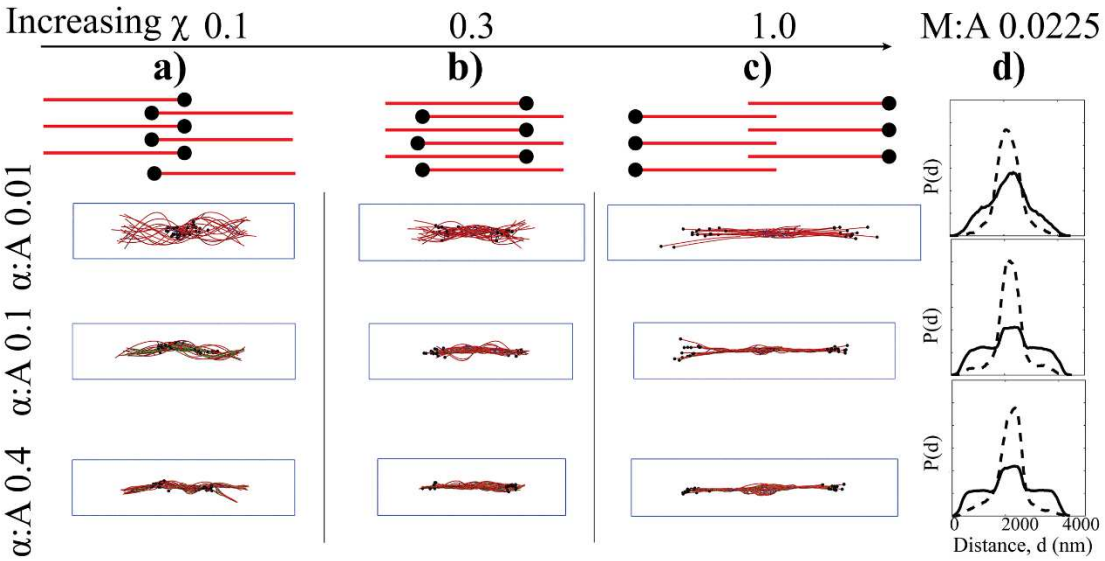

Figure 2-5 The effects of treadmilling factor (χ) and myosin sliding on the morphologies of BAInit networks are illustrated. The upper panel shows a cartoon of filaments (red) with barbed ends (black tips) representing various orientational arrangements realized in our simulations, determined by the interplay between the treadmilling rate and myosin activity. Representative final snapshots from simulations at M: A 0.0225 at various crosslinker mole ratio (α:A) and χ values are shown. For networks with χ=1.0 (c), the probability of finding NMIIA (dotted line) and α-actinin (solid line) along the bundle axis are plotted in panel d.

We found that these catastrophes emerge from the interplay between inter-filament connectivity and treadmilling. Net depolymerization characterizes treadmilling at minus ends, and filament growth at the plus ends. In particular, increasing χ leads to faster filament growth at plus ends (and faster depolymerization at minus ends). In these systems, network stability is assured as long as the newly formed filament segments are effectively crosslinked. Under conditions where the latter does not occur, filament treadmilling dominates the system's structural evolution, leading to poorly connected networks. When well-structured initial bundle configurations result in a highly fragmented network, we denote such transitions as catastrophes (Appendix A,

Figure A-5). On the other hand, at higher mole ratios of α-actinin or myosin, the rate of inter filament connections is enhanced, which prevents network catastrophes.

Having established how inter-filament connections influence network stability, we next investigated the effect of treadmilling speed. Our clustering analysis indicates that treadmilling networks starting from initial unipolar configurations attain BL and ABI morphologies (i.e., non-aster, non-fragmented morphologies) in 33/84 (~40%) cases, compared to 19/84 (~21%) cases for the initial apolar configurations. On the other hand, the initial apolar arrangements lead to aster-like structures in 39/84 (46%) cases contrasting against 20/84 (24%) cases for the unipolar cases. Taken together, these results demonstrate that treadmilling bundles that were evolved from initial unipolar configurations are less likely to undergo morphological collapse than those evolved from initial apolar configurations.

Based on the network morphologies observed at the sampled triad combinations, we suggest the following two phase diagrams, shown in Figure 2-4, indicating dominant network morphologies as functions of M: A and χ. To justify the choice of these two order parameters, we point out that α-actinin dynamics determine bundle stability in conjunction with myosin, however, affecting only very weakly the final network morphology of stable networks. Figure 2-4a suggests that treadmilling unipolar networks sample similar network morphologies to the non-treadmilling cases for $\chi \leq 1.0$. At larger χ values, network treadmilling dominates as crosslinkers and minifilaments cannot effectively connect filament segments that are formed, leading to network catastrophes (Appendix A, Figures A6-A9, see snapshots from simulations

with χ >1.0) On the other hand, treadmilling apolar bundles lead to aster-like states (under non-catastrophic triads). The BL, ABI morphologies sampled by treadmilling apolar bundles have rich diversity due to the interplay between myosin activity and treadmilling, as explained later.

We finally discuss the weak influence of crosslinkers on the morphology of a treadmilling network. We found that unipolar bundles treadmilling at α:A=0.01 and under low myosin mole ratios (0.0225, and 0.09 shown in Appendix A, Figures A6 and A7) χ=1.0 result in network catastrophes. However, significantly increasing crosslinker concentration (e.g., between 10 and 40 folds) can rescue such networks to prefer bundle-like/intermediate morphologies. These findings are in qualitative agreement with the observations by Bidone et al. [139] that at high crosslinker concentrations, bundles form robustly from networks obtained from a wide range of initial orientational biases (at M: A=0.08).

2.3.3. Treadmilling apolar bundles attain a diverse set of network morphologies at long time scales

Under low myosin activity conditions, treadmilling bundles starting from an apolar arrangement generate a remarkably diverse set of final network morphologies, primarily based on how filament barbed ends are spatially localized (see Figure 2-5). These emergent network geometries arise from the tug-of-war between myosin activity and filament treadmilling. On the one hand, treadmilling apolar bundles are subject to the continuous process of plus-end extension and minus-end retraction. On the other

hand, myosin activity drives the mutual sliding of neighboring filaments. If the rate of plus-end extension is slower than myosin sliding, myosin activity dominates, leading to two unipolar bundles connected at their plus ends (Figure 2-5a) or to networks with overlapping plus end segments (Figure 2-5b). Conversely, under vigorous plus end extension conditions compared with myosin sliding, the network transitions to polarity sorted bundles interacting at their minus ends via myosin (Figure 2-5c).

Modulation of χ also controls the overall distribution of myosin minifilaments in such bundles. The computed spatial distributions of myosin minifilaments and α-actinin under low myosin concentrations (Fd) indicate that myosin spatially segregates close to pointed ends, characteristic of sarcomeric ordering [70,118,135]. The latter arises when myosin minifilaments interact with minus ends flanked on either side by plus ends.

2.4. Discussion

Actin bundles are essential for cellular stability, growth, and mechanosensing. While prior experimental and modeling research has primarily focused on bundle formation processes [98,139,170,171], we have addressed the stability and temporal evolution of various bundle configurations in this work. We used MEDYAN, a mechano-chemical forcefield based on molecular principles, to simulate bundle dynamics in 3D. The dimensionality of the model is crucial as filament deformations, and mutual interactions are markedly dimension-dependent. This study comprehensively analyzed how α-actinin and myosin influence the stability and

morphological transformations of unipolar and apolar actin bundles. We discovered that at time scales of about 2000 seconds, non-treadmilling unipolar bundles are stable under a broader range of crosslinker and myosin mole ratios than apolar bundles. At high myosin mole ratios, we observed aster-like states characterized by interacting barbed ends grouped in the center of the cluster with radially emanating pointed ends. We also investigated how actin turnover affects bundle morphology fates by developing and applying a simulation protocol that allows moving system boundaries. Our results indicate that both unipolar and apolar treadmilling bundles undergo network catastrophes when the network's ability to form inter-filament connections is insufficient compared to the treadmilling speeds. *In vivo* cytoskeletal networks undergoing fast treadmilling may avoid such undesired fragmentation using additional mechanisms such as filament capping and actin filament nucleators.

Interestingly, at high myosin concentrations, even quick treadmilling does not rescue the network from transitioning to aster-like configurations. On the other hand, at low myosin activity, initially apolar bundles explore a diverse spectrum of network organizations attributed to the tug-of-war between minifilament activity and filament treadmilling. Under certain conditions, interesting, biologically relevant architectures emerge, such as sarcomeric-like organization. We are not aware of prior models that resulted in the spontaneous assembly of sarcomeric arrangements without imposing spatial restrictions on crosslinkers. In particular, previous attempts to reproduce the sarcomeric distribution of treadmilling apolar networks relied on various assumptions,

such as preferential binding of passive crosslinkers near plus ends [118] or considered systems with both plus and minus end-directed motors [172].

Finally, we reflect on the biological consequences that follow from this work. We found that treadmilling bundles with initial apolar configuration are poised to undergo a remarkable morphological response to the perturbations of the environment, such as alterations of myosin activity or treadmilling rates. However, this level of sensitivity to parameters might be potentially detrimental to the overall stability of the cellular actin network. On the other hand, if only a tiny fraction of the cytoskeleton is organized as apolar bundles, the latter can sensitively respond to various signaling cues that affect the local concentrations of actin-binding proteins. Thus, we propose that apolar bundles might be crucial to cytoskeletal robustness and adaptation in scenarios that demand drastic structural reorganization. The ability to rapidly change network morphology might be necessary for specific cellular functions where force production or rapid cellular reorganization are necessary. Overall, the optimal choice of bundle architecture should be determined by the specific cellular processes that it affects: for example, in the case of cargo transport [173] or protrusive growth [174], a structurally stable unipolar bundle would be the optimal choice, while contractile elements that require frequent reorganization would be more robust when apolar bundles are incorporated into their architectures [69,175].

In summary, we simulated actin bundles in 3D while explicitly accounting for excluded volume interactions, diffusion of actin, crosslinker and NMIIA proteins, and numerous chemical and mechanical processes that enhance the model's realism. We

systematically studied the influences of initial bundle polarity, concentrations of myosin and α-actinin, and the network turnover rate, finding a vibrant palette of bundle evolution trajectories, from stable bundle states to asters and sarcomeric organizations. Additional effects may be considered in future works, such as actin filaments transiently tethering to the substrate and nucleation of filaments via formins or Arp2/3, which will bring us closer to achieving a complete understanding of bundle dynamics under *in vivo* conditions.

Chapter 3 Branching activity modulates network organization between connected and fragmented states in a myosin-dependent manner

This chapter is adapted from a manuscript in preparation. Aravind Chandrasekaran, Edward Giniger, and Garegin A. Papoian. "Branching activity modulates network organization between connected and fragmented states in a myosin-dependent manner."

3.1. Introduction

Biological systems rely on the self-organization of their constituents to perform specific functions. To perform a wide range of physiological functions, cells respond to signals through drastic changes in their shape and organization. These changes are partly due to the cellular cytoskeleton. Cytoskeleton reorganizes through a host of actin-binding proteins to self-organize into various self-assembled structures through a delicate balance between myosin-driven forces and viscoelastic dissipation[100,176]. This cytoskeletal distribution, moreover, is not random. The cell cortex forms a sub-membranous actin shell that surrounds the cell and gives it a characteristic shape. Additionally, actin forms a nuclear cage and comet-tails behind transporting organelles. Local actin masses develop at sites of nascent plasma membrane protrusions, providing the force needed to generate elaborate cellular projections and reproducibly under the instruction of signaling molecules from the surrounding environment.

While such biologically relevant processes involve actin, motor proteins (myosin), and passive crosslinkers, rapid reorganization of cytoskeleton requires additional mechanisms such as actin nucleation, branching, and severing. Our current understanding of actin organization is informed by minimal models of linear actin networks.[59,166,177–180] While they offer critical mechanistic insights, they have limited scope in informing us of cytoplasmic actin networks, which include additional processes that modify actin organization. As a result, little is known about the self-assembly of actin networks with such actin modifying proteins. It is essential to understand the role that NPFs play in network architecture and mechanical properties. Here, we study how the dynamics of actin branching affect the structural properties of the actin network.

The organizational principles by which actin, myosin, and ancillary cofactors collaborate to create dynamic cytoskeletal structures are active research areas [176,178,181–184]. F-actin filaments in solution undergo entropically driven nematic ordering transitions[185,186] at threshold actin concentrations determined by filament lengths[187,188]. Subsequent studies on actin network organization focused on kinetic mechanisms by which passive crosslinkers such as α-actinin[189], fascin[190], and filamin[177] modify dilute suspensions of long, linear actin filaments and also studied the mechanical properties of resulting networks. As passive crosslinkers can kinetically trap the actin filaments in the overlapped state and induce local contractility[160], crosslinked networks exhibit viscoelastic properties. Additionally, varying crosslinker concentration results in an actin network with a wide array of properties[191–194]. Of

particular interest is the study by Weirich et al. in which networks of sub-micron actin filament lengths above a threshold crosslinker concentration readily undergo density transitions to form disconnected high-density aggregates. The aggregates are anisotropic, resulting in a tactoid shape that increases in time till a steady state is reached.[177] Adding low concentrations of skeletal myosin to the system results in myosin alignment along the tactoid mid-plane, while higher concentrations of myosin lead to shape change resulting in two tactoids coupled together by myosin.[178] At larger filament lengths, myosin-driven forces reorganize isotropic networks into either multiple locally contracted clusters or a single globally contracted cluster based on crosslinker concentration.[184,195]

Branched nucleation is a key mode of actin reorganization in living cells. Branched nucleation is primarily controlled by the actin-related-protein-2/3 (Arp2/3) complex, which accelerates nucleation by mimicking the presence of two actin monomers.[17] Arp2/3 nucleates filaments on the side of existing filaments at a 70^{o} angle.[16,196] Branching and debranching activities have profound effects on cell shape and dynamics [197,198] and indeed are commonly found to be central targets of the external signals that regulate cytoskeletal events[14,15,199,200]. Computational studies on disordered dendritic actin networks have helped identify the kinetic[201] and mechanical[202] differences between linear and dendritic actin networks. Both studies inform us of dendritic network dynamics in the absence of force-sensitive Arp2/3 kinetics. Growing evidence on the force-sensitive unbinding of Arp2/3 suggests a key role for mechano-sensitivity in cytoplasmic dendritic networks.[203,204]

Here, we subject micron long actin filaments crosslinked by α-actinin and myosin to varying concentrations of Arp2/3 branchers in a cylindrical volume of 23.56μm^3. We show that branching molecules modulate the length distribution of the actin network through their nucleation activity. While networks under low branching activity organize into globally contractile structures, highly dendritic networks organize into locally contractile, fragmented networks characterized by actin droplets of heterogeneous volumes. We show that networks with low branching activity are dominated by myosin-driven contractility. On the other hand, networks with high branching activity are initially dominated by myosin-driven contractility, but branching-driven network fragmentation determines the steady-state network organization.

3.2. Methods

All simulations performed in this work were carried out in MEDYAN [89]. We chose a cylindrical reaction volume of 2μm diameter and 7.5μm height to avoid artificial edge dependent biases found in cuboidal systems. Simulations were performed with 400 randomly oriented, 40 monomers long, seed filaments, and 20μM diffusing actin. Filaments are represented as rigid cylinders that are joined at hinge points. While the cylinders resist stretching, bending deformations are allowed at the hinge points. Each cylinder is 40 monomers long, with four binding sites available to bind linker/motor/brancher molecules. In order to recreate a contractile network, the network was subjected to non-muscle myosin IIA (NMIIA) minifilament (M: A=0.1)

and α-actinin (α:A=0.01). Linear networks described above were evolved for 1s before activating Arp2/3 molecules. Stochastic chemical evolution in MEDYAN is achieved through the *next reaction method* [88]. Diffusion and reaction events are modeled at the level of an actin monomer. Spatial description of filaments along with necessary mechanical forcefields accurately captures stress build-up during chemical evolution. The accumulated stress is released using a gradient descent algorithm every 25ms of chemical evolution to account for mechano-chemical effects. In MEDYAN, unbinding of α-actinin and myosin minifilaments are rendered mechanosensitive as slip, catch bonds, respectively. Unbinding rates are calculated at the end of every minimization cycle. This cycle of events is repeated to generate 2000s long trajectories.

In our model, Arp2/3 binding produces an offspring along the side of the mother filament at a 70^{o} angle forming a dendrite[74,196]. The offspring filament's minus-end is protected from (de)polymerization fluctuations in the Arp2/3 bound state. In our model, Arp2/3 unbinding results in a free offspring filament, diffusing Arp2/3 molecule, and a binding site on the parent filament. We model Arp2/3 unbinding as a force-sensitive slip bond with a characteristic unbinding force of 6pN[203]. All simulation parameters used and the number of replicates generated in this study are mentioned in Appendix C, Table C-1.

3.3. Results

3.3.1. Increased Arp2/3 activity reduces diversity in filament lengths and increases network treadmilling rate

To understand the impact Arp2/3 branching has at the filament level, we simulated networks with 20μM G-actin and 400 short seed filaments, each 40 monomers long. Networks were evolved under α-actinin (α:A=0.01) and myosin (M:A=0.1) for 1s, after which Arp2/3 molecules were activated. We studied the effect of various Arp2/3 concentrations on the linear network. We found that in linear networks ([Arp2/3] = 0nM), the seed filaments extended into long filaments thanks to diffusing pool of G-actin. With the addition of Arp2/3, filament distribution bifurcates into a population of short filaments nucleated by Arp2/3 and a population of seed filaments (Figures 2-1 and B-1).

Further, an increase in Arp2/3 concentration results in networks dominated by dendritic nucleation and are characterized by extremely short filaments (<0.5μm). These results can be explained by the combination of finite bound lifetimes for Arp2/3-parent-offspring filament complex (τ=50s) [205] and the experimentally observed, mechanosensitive nature of unbinding rates that are incorporated in our model[203]. Upon binding, Arp2/3 nucleates a new offspring filament with a stabilized minus-end along the parent filament. In our model, Arp2/3 kinetics is mediated by a force-sensitive slip bond, with an unbinding event generating free Arp2/3 and a daughter filament with a free minus end. Branches experience tension when subject to myosin walking and

crosslinker kinetics, and unbind at rates that are modeled as a slip bond behavior. Thus, increasing Arp2/3 activity increases the filament nucleation rate resulting in a steady-state characterized by short filaments. We also looked at the treadmilling rate of the network to understand remodeling rate of the network. We define treadmilling rate as the average of the total number of monomers that depolymerize from minus ends and the number of monomers that polymerize from plus ends of filaments in 1s. We find that the treadmilling rate at steady-state increases with Arp2/3 concentration due to the increase in the number of filament ends from Arp2/3 based nucleation. Additionally, Arp2/3 unbinding exposes the minus end to fluctuations from filament polymerization and depolymerization reactions. Taken together, the results shown in Figure 3-1 suggest that under the influence of Arp2/3, branching activity produced a population of short filaments and the networks experienced enhanced treadmilling rate.

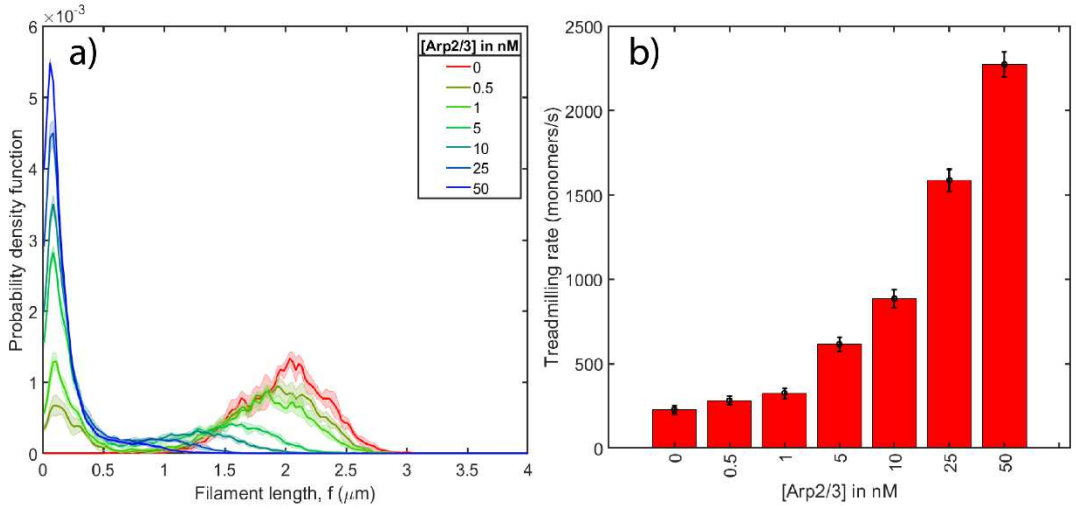

Figure 3-1 Dendritic activity in networks causes a reduction in filament length and increases monomer replacement by treadmilling. The plot of a) filament length and b) network treadmilling rate of networks at various Arp2/3 concentrations. a) Solid lines and shaded areas represent the mean and standard deviation of filament lengths from multiple replicates. b) Mean treadmilling rate of the network is plotted as a bar graph with error bars

representing standard deviation. Networks' approach to steady-state was quantified based on time invariance of mean treadmilling rate. As the treadmilling rate stabilized around 1500s, data from the last 500s of trajectories was employed in panel B.

3.3.2. Arp2/3 alters the hierarchical organization of actin networks

Having understood how Arp2/3 affects properties of actin filaments, we then investigated the influence of Arp2/3 on the network level organization of actin. To achieve this, we mapped the high-resolution actin filament coordinates onto a coarse-grained density field. Dividing the reaction volume into voxels of size 100nm, we counted the number of F-actin monomers enclosed in each voxel to define local actin density. Additionally, density was averaged over neighboring pixels. Together, this protocol helps us understand the spatial distribution of actin in the reaction volume by avoiding eccentricities arising due to extremely small clusters and also prevents discontinuities in the density field [206,207].

To understand how actin is organized in the reaction volume, we visualize the density field at various voxel concentration thresholds (Figure 3-2). This visualization is similar to observing fluorescently labeled experimental actin networks at varying intensity thresholds. When the density field considers all voxels with F-actin (threshold of 0μM), we see minor differences in actin organization from changing Arp2/3 concentration. Density fields at higher thresholds reveal drastic differences in actin organization. When the threshold is set to bulk actin concentration (20μM) of our simulations (Figure 3-2), we see that actin is not distributed uniformly throughout the volume but is rather concentrated among a subset of voxels under all Arp2/3 concentrations studied.

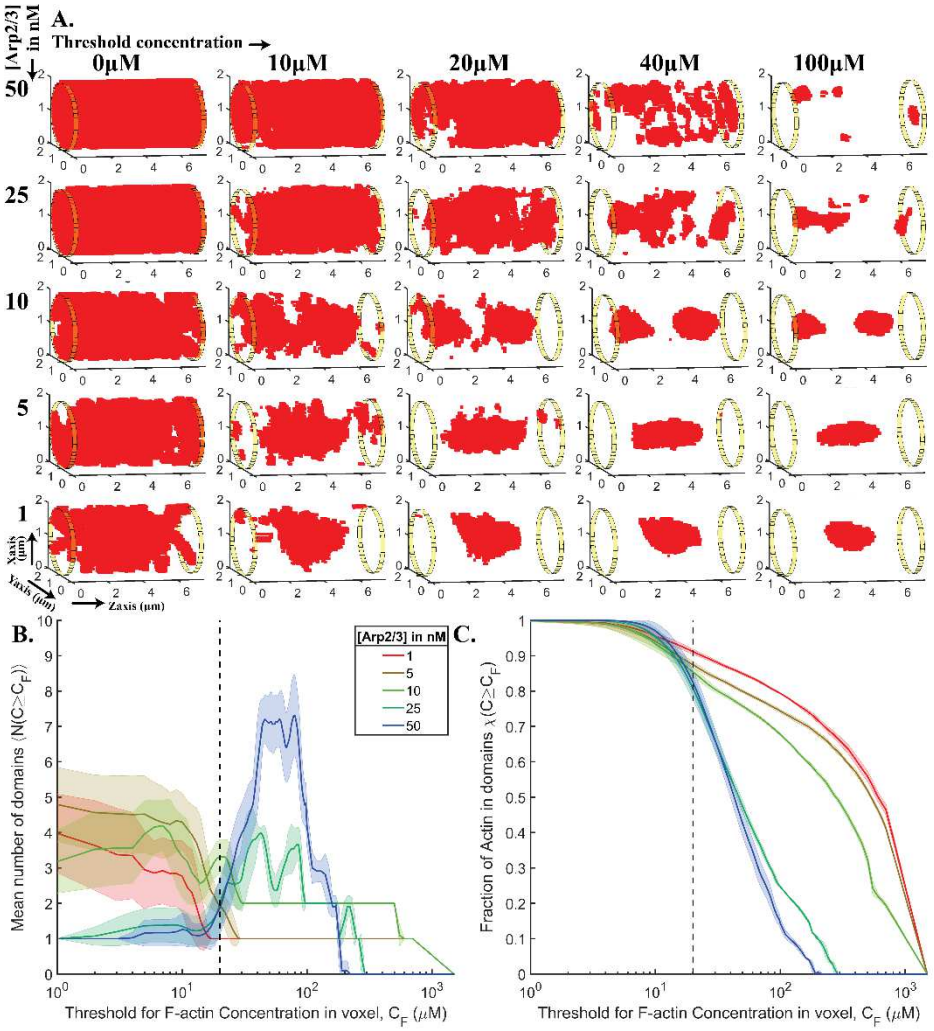

Figure 3-2 Visualization of actin density field reveals Arp2/3 driven changes to actin organization. A. We visualize representative final snapshots from our simulations at various Arp2/3 concentrations as a density field. Cylindrical reaction volume is discretized into voxels of size 100nm to define local F-actin density. The ends of cylindrical volume are shown as 50nm thick yellow cylinders. Please refer Materials and Methods section for more information on the actin density field computation. Red squares represent the Center of mass of voxels that contain actin above the threshold concentrations (listed above). B. Plot of the number of disconnected domains identified when viewing the actin density field at various threshold concentrations. The X-axis is shown in logarithmic scale, and the bulk actin concentration is shown as a dotted line. C. The fraction of total actin monomers found by integrating over the density field is plotted at various threshold actin concentrations. The dotted line represents bulk actin concentration.

Additionally, at the 20μM threshold, we see stark differences in actin organization depending on branching activity. At low Arp2/3 concentrations, F-actin contracts globally into a single domain. Increasing Arp2/3 concentration to 10nM results in a network that is composed of two high actin density domains. At higher Arp2/3 concentrations ([Arp2/3] =25nM and [Arp2/3] =50nM), the number of domains increases suggesting that the density distribution is spatially heterogeneous. Increasing thresholds to 2x and 5x bulk actin concentration does not reveal significant changes in trends observed. Figures 3-2 b and c show the nature of actin organization over a wide range of threshold concentrations. We see that the trends in the number of domains from changing Arp2/3 levels do not change when the actin density field is visualized at 1-10x bulk actin concentration. We also find that under all Arp2/3 concentrations studied, most of the actin (>80%) is found in regions where the local voxel density is 20μM and above (Figure 2-2C). Thus, actin's overall hierarchical organization is dictated by a combination of filament length and, as we will show below, myosin activity.

To quantify differences in network organization due to Arp2/3 in these contractile networks, we investigated the density fields at a concentration higher than the bulk actin concentration. Visualizing density fields at thresholds lower than bulk does not offer insights into the contractility-driven organization of actin. Using a breadth-first search algorithm, we identified the disconnected domains in the reaction volume and calculated domain volume for each. Distribution of domain volume from the last 100s (sampling frequency = 5s) of trajectories (Figure 3-3) under a threshold concentration

of 40μM revealed remarkable differences in domain organization (Figure 3-3). As Arp2/3 concentration is increased, two trends are observed. First, median domain size decreases. Second, heterogeneity of domain size increases, particularly at intermediate concentrations of Arp2/3, before beginning to reduce again at the highest concentrations. We postulated that heterogeneity arises from a stochastic fluctuation of a balanced set of competing factors that drive domain expansion and contraction, respectively, but which begin to resolve in favor of domain condensation and fragmentation at the highest level Arp2/3. The results discussed above suggest that Arp2/3 alters the hierarchical organization of F-actin into domains causing fragmentation into domains with heterogeneous size distributions. This conjecture will be examined in more detail in the Discussion.

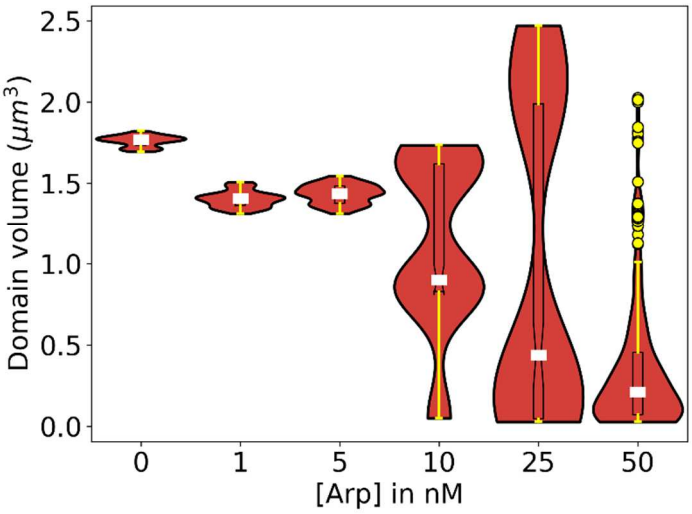

Figure 3-3 Distribution of actin domain volume reveals differences in actin organization resulting from Arp2/3 activity. Domain volume distributions at various Arp2/3 concentrations from the last 100s of the trajectories are represented as violin plots. The box plot shows the 25-75 percentile represented as a box with the median shown as white lines. Whiskers are shown as solid yellow lines with outlier data points represented as yellow circles.

3.3.3. Increased Arp2/3 activity results in fragmented actin network

To understand the mechanism by which networks at higher Arp2/3 concentration fragment into multiple domains, we investigated the time profile of the actin density field at a concentration cut-off of 40μM. Figure 2-4 shows time profiles of the density field from representative snapshots at various Arp2/3 concentrations. We see that initially, networks at all Arp2/3 concentrations are composed of spatially fragmented domains. As the simulation proceeds, we find that spatial segregation of the network into actin-rich and actin-depleted regions occurs in an Arp2/3 concentration-dependent manner. In networks with <10nM Arp2/3 concentrations, the domains merge with time, resulting in a single, connected domain. At Arp2/3 concentrations of 10nM and above, actin networks initially contract and merge through agglomeration of preexisting domains. However, at later stages in the simulation, these domains of high actin density decouple from one another, resulting in a network where high actin concentration regions are again spatially fragmented. Together, these results demonstrate that the mechanism of actin organization changes depending on Arp2/3 concentration.

To gain more insights into the Arp2/3 driven fragmentation, we calculated the number of disconnected domains found in the density field at snapshots taken every 5 seconds

(Figure 3-5a) using a breadth-first search algorithm over the voxels that satisfy

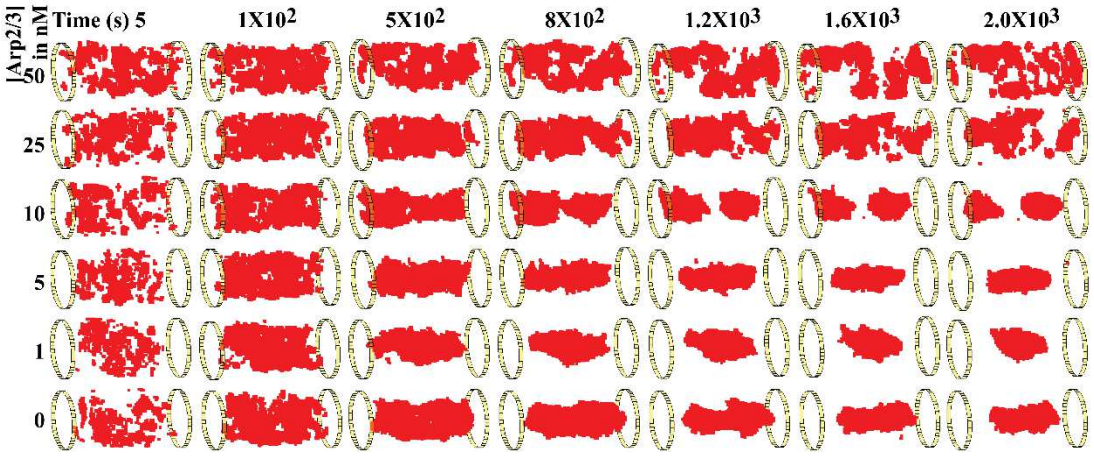

Figure 3-4 Time profiles of actin density field reveal altered network organization leading to actin fragmentation at elevated Arp2/3 concentrations. At various time points in our simulations with different Arp2/3 concentrations, representative snapshots are converted into actin density fields to understand actin organization. The actin density field is visualized at 40μM threshold concentration in each case. The voxels that have a local actin concentration higher than the threshold concentration are shown in red. Timestamp in seconds is shown to the top while Arp2/3 concentrations are mentioned in the left.

the concentration threshold. We find that the number of domains decreases steadily with time at low Arp2/3 concentrations (≤5nM) till the entire network is composed of a single, connected domain. Looking at the actin concentration in the domains (Figure 3-5b), we see a steady increase in actin concentration with time. In contrast, at higher Arp2/3 concentrations, networks evolve with a biphasic domain count profile where during the initial phase, we see a reduction in the number of high-density actin domains, followed by a maturation phase where the number of domains increases. Additionally, increasing Arp2/3 concentration progressively limits actin concentration in domains (Figure 3-5B), suggesting that Arp2/3 reduces the effective packing of filamentous actin.

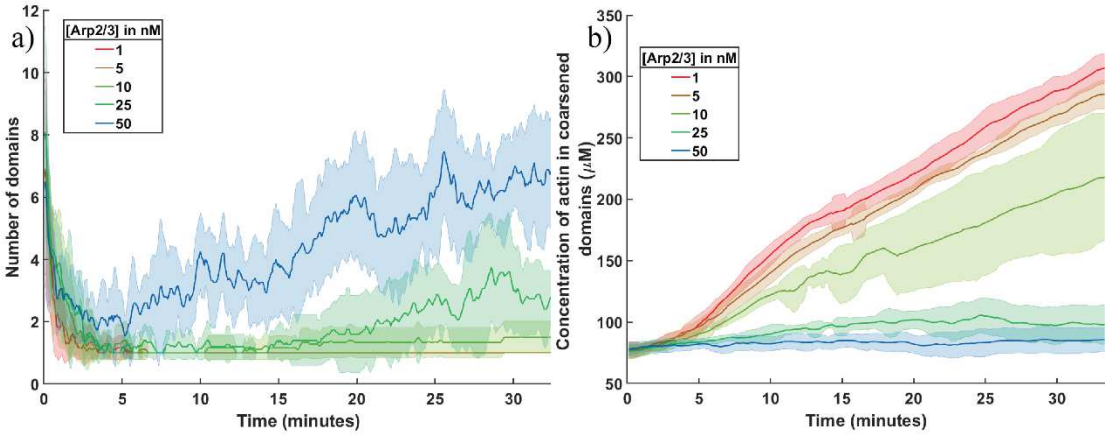

Figure 3-5 Analysis of F-actin domains reveals Arp2/3 dependent differences in network organization. a) Number of actin domains found from actin density field analyses is plotted as a time profile at various Arp2/3 concentrations. b) Time profiles of actin concentration in the domains are plotted at various Arp2/3 concentrations. a) and b) Solid lines and shaded areas represent mean and standard deviation, respectively.

3.3.4. Competition between myosin and Arp2/3 dynamics modulate actin organization

The Arp-dependent changes to actin concentration in high actin density domains suggest a crosstalk between nucleation-driven treadmilling and myosin-driven contractility. To understand the role of myosin in the mechanism of Arp2/3-driven fragmentation, we studied actin networks by reducing myosin concentrations to 50% or 10% of myosin concentrations employed in simulations discussed so far. The number of domains from the last 100s of the 2000s trajectories is plotted in Figure 3-5, a-c. At all myosin concentrations studied, increasing Arp2/3 results in a fragmented network characterized by an elevated number of high-density actin domains. We also looked at actin concentration in the high actin density domains to understand myosin's impact in organizing filamentous actin (Figure 3-5d-f). Consistent with Figure 3-5b,

increasing Arp2/3 reduces F-actin concentration in domains. Additionally, we find that at any given Arp2/3 concentration, reducing myosin decreases actin concentration in domains consistent with the reduced contractility of the networks. The actin concentration in these domains (Figure 3-5, d-f) reduces with increasing Arp2/3, particularly at high concentrations of myosin, but has reduced effect as myosin level decreases, suggesting that Arp2/3 reduces actin density primarily by hindering myosin-driven contractility.

We then ask if reducing myosin levels increases fragmentation of the actin network. Wilcoxon test at 1% significance reveals that reducing myosin to 50% and 10% causes increased fragmentation of actin networks up to [Arp2/3]=10nM. At higher Arp2/3 concentrations, we find that reducing myosin to 50% does significantly increase fragmentation, but a further reduction to 10% does not affect the network fragmentation from the ones observed at 50% reduction. It is interesting to note, however, that under all conditions studied, reducing myosin did increase fragmentation in the initial phase (<10min) of the trajectories (Appendix, Figure B-2), suggestive of time scale differences in the dominant mechanism that drives actin organization in dendritic networks, perhaps accounting for the biphasic temporal evolution of domain number under conditions of high Arp2/3 (Figure 3-5).

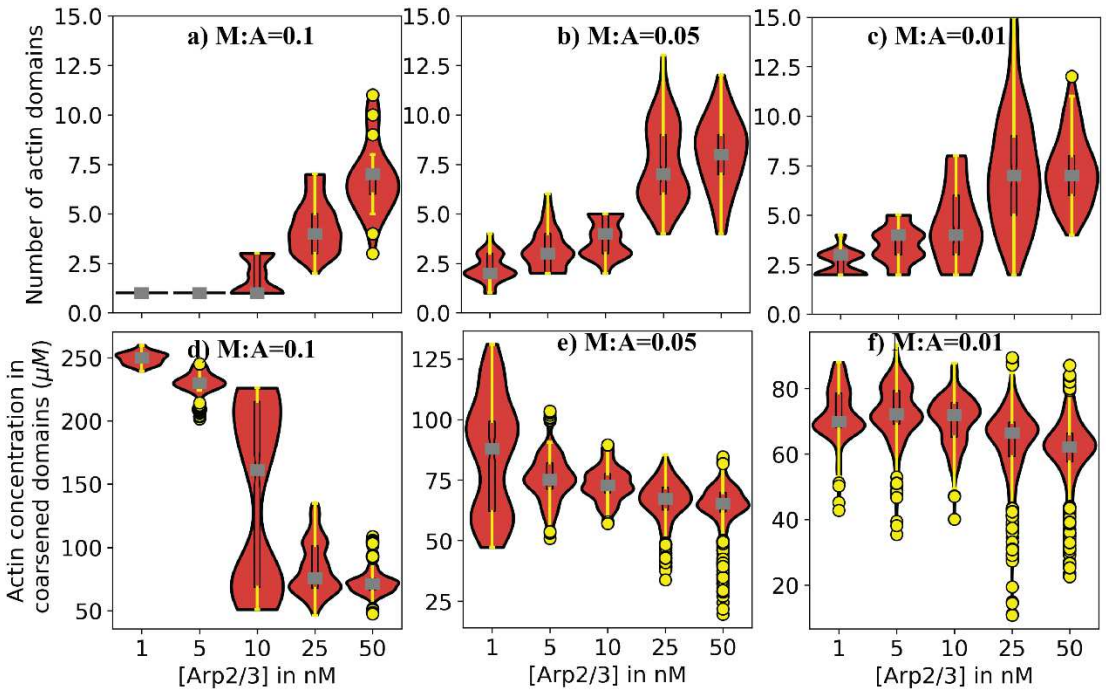

Figure 3-6 Myosin competes with actin to prevent network fragmentation. a-c) Violin plots showing the number of domains in the actin density field obtained at a threshold concentration of 40μM at different Arp2/3 concentrations (X-axis). Myosin mole ratios are mentioned above each panel. d-f) Violin plots showing actin concentration in high-density actin domains. Note that the domains are determined based on the mean concentration threshold, while the concentration plotted here is calculated based on actin concentration determined from filament data. Hence, the actin concentration in domains can be below the mean concentration threshold. a-f) Plots also show median values (gray) and 25% and 75% quantiles as box plots (black). Whiskers represent data ranges (yellow lines), and outlier data are plotted as yellow circles.

3.3.5. The activity of branching protein alters dynamics of actin domains towards fragmented states

The results above show how overall network properties evolve over time, with Arp2/3 causing global spreading and myosin producing local condensation, but how does this combination give rise to the final, fragmented states that we observe? To understand the mechanism by which high actin density domains evolve, we studied the trajectories of the density field. We classified each domain's birth as either coming from

a domain splitting or domain nucleation event and the loss of a domain as resulting from either domain-domain merge or domain destruction event (Figure 3-7a). While domain nucleation happens when actin in a region within the reaction volume condenses, destruction happens as actin in a high-density domain relaxes from events such as myosin/crosslinker unbinding, thereby lowering actin concentration to below our chosen threshold. Figure 3-7B shows that increasing Arp2/3 concentration increases the frequency of occurrence for all four elementary events that alter domain number. It is interesting to note that the mechanisms that lead to an increase in domain number are roughly as prevalent as mechanisms that cause a decrease in domain number. Also, we see that actin domains form primarily from the splitting of existing domains, while domain-domain merges are the dominant mechanism to explain the loss of an F-actin domain.

To understand the differences in domain dynamics between networks from low Arp2/3 and high Arp2/3 concentrations, we plotted distributions of domain number altering events accumulated over 500s intervals (Appendix, Figure B-3). We see that at low Arp2/3 concentrations, actin domains are highly dynamic in the first 500s of trajectories. Although all four domain birth and death mechanisms occur, domain-domain merge events happen at a higher frequency. As a result, within the first 500s of trajectories, networks with [Arp2/3]<10nM result in a steady decrease in the number of domains resulting in a single, connected domain. The space-spanning domain is significantly less dynamic, suggesting that domain merges are irreversible in networks with low [Arp2/3]. This observation is consistent with experiments where actin

condensates merge irreversibly with time, causing a steady increase in actin mass within condensates[208,209].

On the other hand, networks with high Arp2/3 concentration are less stable than their low Arp2/3 counterparts. As the domain birth and death events roughly balance each other throughout the trajectories, we postulate that elevated Arp2/3 levels stochastically favor a fragmented network state with multiple high actin density domains. To understand this, we employed a stochastic modeling framework assuming that the change in the number of domains in a given time interval depends on deterministic factors characterized by a combination of effective drift and random fluctuations. Further, we consider that the effective drift and diffusion terms depend on the number of domains at a given time point. Analyzing time series of the number of domains from trajectories, we see that the drift is lowest for states with an intermediate level of fragmentation, with minimum drift when the snapshot has 3, 4, and 5 fragmented domains for networks at 25nM [Arp2/3] and 3 to 6 domains for 50nM [Arp2/3] (Figure 2-7D). Besides, for networks with more than six domains, the drift parameter is negative, indicating that the system favors domain death events while at values lower than the minima, drift is positive, suggesting that the system favors the birth of events. Thus, the fragmented state is the result of a delicate balance of domain dynamics. We also see that the diffusion coefficient term is significant at all n values studied, highlighting the role that random noise plays in the process. Please refer Appendix for a discussion on the stochastic model and parameter estimation.

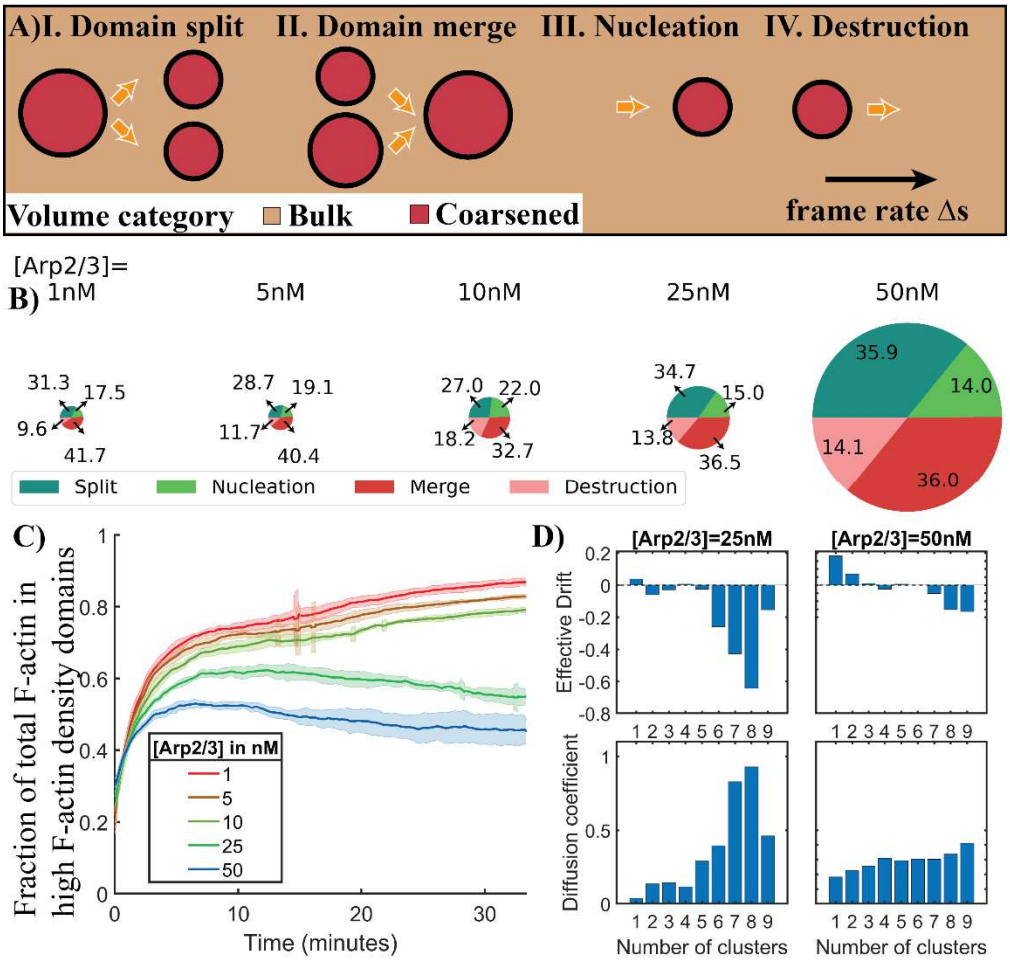

Figure 3-7 Analysis of domain dynamics reveals the underlying mechanism of F-actin organization into high-density actin domains. A. The cartoon rendering describes elementary transition mechanisms showing F-actin domains in red, with brown regions representing low-density actin background. AI-AIV shows four different transition mechanisms in a reference snapshot that affect the number of clusters in the following snapshot. B. Pie charts showing the percentage of transitions observed throughout the trajectory at different Arp2/3 concentrations. The size of the pie chart is proportional to the total number of transitory events. C. Time profiles of the fraction of total actin in the domains at various Arp2/3 concentrations. The solid line and shaded area respectively represent mean and standard deviation. D. Estimation of drift (top row) and diffusion coefficients (bottom row) at various cluster sizes from trajectories of high Arp2/3 concentrations, 25nM (left column) and 50nM (right column).

3.3.6. Relative roles of geometric branching vs. kinetic nucleation in the effect of Arp2/3

The fragmentation of networks in our simulations can be explained as a combination of two distinct phenomena: myosin-driven contractility and Arp2/3 driven nucleation. We find that increasing dendritic activity in a network results in short filaments (<1μm) (Figure 2-1a). Such short filaments organize into a non-percolated network through which myosin-driven contractile forces cannot effectively propagate. Such non-percolated networks contract locally due to myosin-driven contractility resulting in a fragmented network with multiple high-density actin domains. To understand the role of branching molecule in fragmentation, we simulated actin networks with varying concentrations of synthetic minus-end nucleators with the same kinetics as Arp2/3 but lacking the capacity to bind a mother filament and generate a branched structure. These nucleators nucleate filaments and stay attached to the minus end till unbinding. We find that high nucleator concentrations reproduced the network fragmentation (Appendix, Figure B-4) suggesting that the nucleation activity alone, independent of a branching geometry, is sufficient to generate network fragmentation.

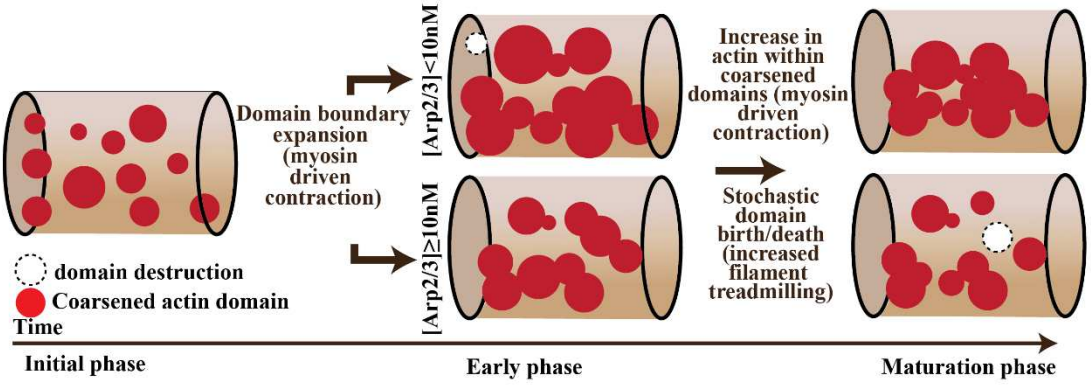

Figure 3-8 Cartoon outlines the proposed mechanism to explain Arp2/3 dependent network organization. Cylindrical reaction volumes are shown with red blobs representing actin domains. The dominant mechanism for transitions along a trajectory is mentioned, along with the filament level interaction mentioned within parenthesis. Domain destruction events are mentioned as empty circles with dotted lines.

3.4. Discussion

This study investigated filamentous actin's network organization and its dependence on the branching molecule Arp2/3 and myosin. We propose the following mechanism to explain the differences in actin organization in networks of low and high dendriticity (Figure 2-8). During the initial stages of trajectory evolution, multiple small domains are formed under all Arp2/3 conditions studied. The domain boundaries expand due to G-actin's conversion to F-actin and due to myosin contractility, which increases the network's connectivity, as evidenced by a significant reduction in the number of actin domains. Figure 3-7C shows the steep increase of F-actin in domains within the first 5 minutes of trajectory evolution. As the network evolves, the hallmarks of Arp2/3 dependency become more evident. At low Arp2/3 concentrations, networks form a single, connected domain due to dominant myosin activity and a percolated network architecture. Subsequently, the number of domain birth and death events significantly

decreases (Figure B-3). At higher Arp2/3 concentrations, network fragmentation occurs due to a high degree of fluctuations between domain birth and domain death events with a drift towards a fragmented steady state, with the degree of fragmentation depending on the balance point between domain increase and decrease.

3.5. Conclusion

Our work demonstrates how network organization can be drastically altered in the presence of branching molecules. Changing the concentration of Arp2/3 alters overall network connectivity by increasing the population of sub-micron long filaments. We show that irrespective of Arp2/3 concentration, networks initially evolve with decoupled local contraction events leading to multiple domains composed of condensed actin. As the network evolves, we observe contractile domain merge events resulting in fewer actin domains. As network evolution progresses, we see that networks with low Arp2/3 activity are trapped in the connected, globally contractile state. In contrast, high Arp2/3 activity causes the networks to evolve stochastically towards fragmented network states. We also show the elementary domain level processes that underlie such transitions and argue that network fragmentation is stochastically favored in high Arp2/3 networks. This study suggests that signaling pathways that affect Arp2/3 levels tune the overall network architecture through subtle changes to network connectivity.

Chapter 4 Computational simulations recapitulate the Abl-dependent dynamics of axonal actin *in-vivo*

This chapter is adapted from a manuscript in preparation. Aravind Chandrasekaran, Akanni Clarke, Philip McQueen, Hsiao Yu Fang, Garegin Papoian, and Edward Giniger. "Computational simulations recapitulate the Abl-dependent dynamics of axonal actin in-vivo."

Author contributions: A.C. performed computer simulations and analysis. A.C. and G.A.P. designed the computational tool. H.Y.F., Ak.C., P.M., and E.G. performed experiments and analysis on experimental data. A.C., E.G., and G.A.P. wrote the manuscript.

4.1. Introduction

During embryonic development in both vertebrates and invertebrates, axons send out projections autonomously, in an orchestrated fashion to facilitate the formation of complex neuronal patterning.[210] The ability of axons to extend through the extracellular space *in vivo* is coordinated by specialized structures called growth cones found at the tips of motile axons.[211] As the axon extends, growth cones sense and respond to extracellular biochemical guidance cues such as Netrins, Semaphorins, Slit, and Ephrin [212–215]. The growth cones are made of actin and microtubule filaments along with a host of actin modifying proteins and signaling molecules such as Rho-family GTPases.[212,216,217] Actin and microtubules play specific roles in the

extension of axons.[79,143,218,219] Many studies have tried to understand the mechanism of such autonomous growth by focusing on the morphological changes of growth cones or the cytoskeletal signaling process that aids in growth.[220] Nevertheless, critical knowledge gaps exist in the synergy between biochemical signaling and the cytoskeletal growth response.

Studies focusing on growth cone morphology have helped uncover the relationship between structural dynamics of cytoskeleton and the mechanism of axon extension. While knowledge of growth cones dates back to seminal work by Cajal, fluorescent and electron, microscopic imaging of neuronal cell cultures has helped us understand the ultrastructure of growth cones. [221,222] Such plated growth cones are flat and fan-shaped with cytoskeletal structures such as filopodia and lamellipodia. The growth cone is composed of the periphery and the central regions rich in actin and microtubules. Growth cone motility is initiated by filopodial protrusions that explore the local environment. Soon lamellipodial growth displaces growth cones. Subsequently, microtubules stabilize the extended tips by extending into the central region of the growth cone. Finally, the axon shaft extends and reorganizes to consolidate the growth cone architecture. Axons extend by iterative repetition of these steps.[216,223] Growing evidence from in vivo studies of axons reveals an alternate organization of growth cone. These growth cones are bulbous and protrude primarily by leveraging filopodial protrusions.[224–227] These axons are expected to protrude by a stochastic inch-worming mechanism of actin and microtubule within the growth

cone. In this study, we explore the relationship between signaling and actin organization in such growth cones.

The changes to growth cone architecture are controlled by specific signal transduction molecules that act as the intermediaries between the membrane-bound signal receptors and the cytoskeleton binding proteins. These intracellular molecules dynamically alter kinetic fluxes of essential actin-binding proteins and modify cytoskeletal structure. Despite knowledge of the downstream effectors of signaling molecules, we do not understand the emergent axonal architectures resulting at different signaling levels.

The relationship between architecture and biochemical signaling has been elaborated in Abelson (Abl) nonreceptor tyrosine kinase. Abl is a key signaling molecule that is known to act downstream of all commonly known signaling receptors.[228] Recent imaging studies on imaginal wing discs in Abelson (Abl) nonreceptor tyrosine kinase have been studied by Giniger lab on the *Drosophila* Twin sensilla of the margins (TSM1) axons reveals that Abl mutations lead to developmental errors.[225,229] TSM1 neuron wires one of the two key mechanoreceptors (TSM1 and TSM2) on the wing of Drosophila. TSM1 neuron is a pioneer neuron that develops early in the embryonic stage and travels autonomously for 120 microns from TSM1, thereby pioneering the L1 nerve patterning. Genetic and biochemical analysis has revealed that Abl alters filament organization by simultaneously promoting Arp2/3 driven nucleation and inhibiting Enabled (Ena) driven processive-polymerase activity. [230,231] While the roles of the two downstream proteins have been studied

independently,[16,23,120,232] the relative importance of the two is still poorly understood.[30] Imaging studies of TSM1 axons reveal that Abl ensures spatial correlation and dynamic coherence of actin networks within the growth cones. Under both gain-of-function and loss-of-function conditions, growth cones are characterized by increased spatial fragmentation of actin and dynamic incoherence. Additionally, while Abl over-expressed growth cones have wider growth cones, growth cones with Abl knockdown have narrower growth cones.

Despite knowledge of the filament level interactions of Abl and the consequences at the growth cone level, we do not understand the emergent mechanism by which Abl controls growth cone architecture. Also, it is not possible to resolve single actin filaments *in vivo* imaging experiments. Hence, we choose a sophisticated mechanochemical model called MEDYAN to simulate key processes that account for cytoskeletal changes that result from Abl signaling. This is the first computational study to our knowledge to study the effect of axonal signaling on growth cone actin architecture. As the relative effect of Abl on Arp2/3 promotion and Ena inhibition is not known, we simulate networks with 20μM actin and a wide range of Arp2/3 and Ena concentrations. We find that Arp2/3 plays a crucial role in determining filament length distributions and actin packing in growth cones. We also see that the growth cone mimics capture essential features of actin distributions measured in experiments and also find evidence to explain the mechanism of actin fragmentation observed in overexpressed Abl axons in vivo. Finally, we study the functional consequence of the actin architecture at various expression levels and prove that Abl overexpression causes

mechano-chemical fragmentation of the actin network. We also discuss the consequence of fragmentation in altering the motility and growth of TSM1 axons.

4.2. Methods

In order to faithfully simulate axonal actin networks, we simulated contractile actin networks under cylindrical boundary conditions. As simulations over the entire length of growing axon are computationally expensive, we restricted the reaction volume to cylinders of height 7.5μm and radius 1μm. This volume represents approximately 50% of the growth cone volume observed *in-vivo* for TSM1, a growth cone with uniquely well-characterized actin distribution and dynamics that we take as our point of comparison throughout this analysis.[225] Axonal growth cone mimics were generated through stochastic evolution of actin networks initialized with 400, 40 monomer long filaments that were randomly oriented in the reaction volume with 20μM actin. Mole ratios of non-muscle myosin minifilaments (NM-IIA) and α-actinin were chosen to be 0.1 and 0.01 to observe contractile behaviors similar to previous studies. [100,233] A deterministic ODE model of Arp2/3 and Ena dynamics was used to determine bounds on Arp2/3 and Ena concentrations (Figure 4-1, Appendix C.3). Hence, we simulated networks at concentrations of 1, 5, 10, 25, and 50nM Arp2/3 and Ena.

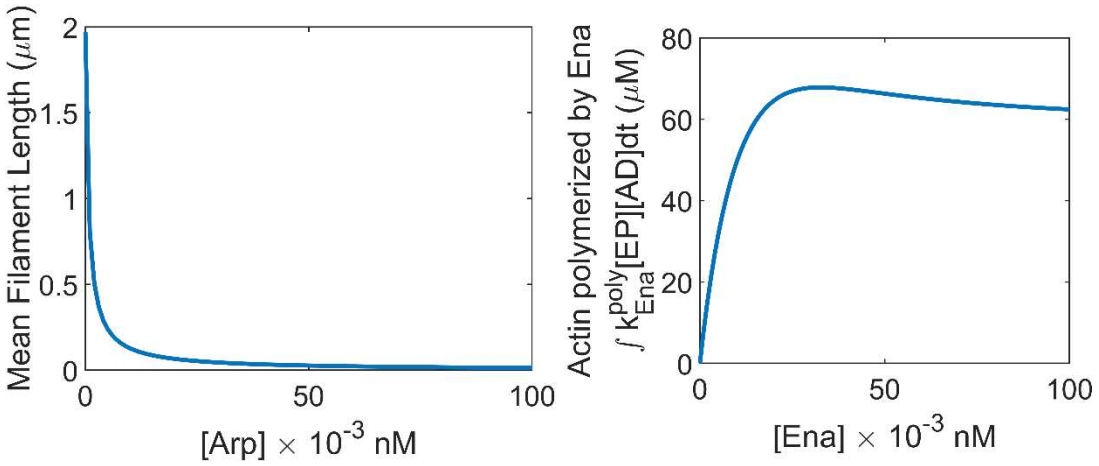

Figure 4-1 Deterministic model for branching and Ena kinetics predicts bounds for Arp2/3 and Ena concentrations. A. Plot of mean filament length predicted by a deterministic model of filament dynamics at various Arp2/3 concentrations ([Ena]=0nM]). B. Plot of total diffusing actin that is converted to filamentous actin through Ena-driven filament extension at various Ena concentrations ([Arp2/3] = 0nM).

A stochastic simulation platform, MEDYAN[89], was used to generate six replicates for each Arp2/3 and Ena concentration studied. MEDYAN simulates chemically active reaction networks and additionally enables force-sensitive, stochastic simulations of filamentous active networks, such as actin and microtubules. In this study, we restrict our discussions to actin networks in the growth cone. Actin filaments are represented as a series of non-deformable cylinders coupled at hinge points. Bending deformations around hinge points are allowed corresponding to a persistence length of 16.7μm. [101] Myosin and α-actinin molecules are represented as Hookean springs with equilibrium lengths based on experimental measurements (refs). Please refer to Appendix B, Table B-1, for details on all parameters used in this study. The simulation space is composed of reaction-diffusion compartments overlayed with the filamentous actin phase. Diffusing reactive molecules (G-actin, unbound crosslinkers, myosins, Arp2/3, and

Ena) are considered homogeneously distributed throughout the reaction-diffusion compartments. Thus, a diffusion reaction is modeled as a hopping reaction between two neighboring compartments. Reaction propensities are defined over the compartment phase and stochastic trajectories are generated by evolving the chemical reaction network using the *next reaction method*.[88] Chemical events in MEDYAN can lead to mechanical stress accumulation. MEDYAN alternates between short bursts of chemical evolution (25ms) and conjugate gradient mechanical equilibration to generate physically realistic trajectories. Additionally, mechanochemical sensitivity of α-actinin unbinding, myosin walking, and unbinding are incorporated in the model. Six replicates of 2000s long trajectories were generated for each (Arp2/3, Ena) concentration pair.

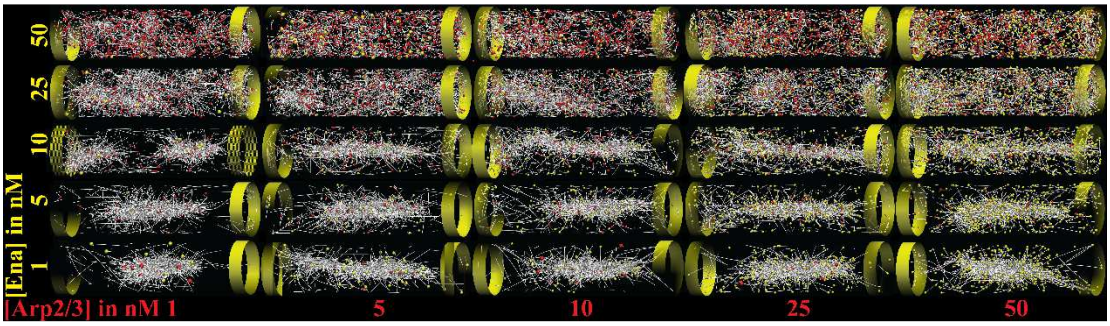

Figure 4-2 Gallery of representative, final snapshots from 2000s long simulations of 20μM actin in cylindrical volumes of height 7.5μm and radius 1μm at various Arp2/3 and Ena concentrations. Arp2/3 concentrations are mentioned at the bottom, while Ena concentrations are noted to the left. F-actin, bound Arp2/3, and bound Ena molecules are colored in white, red, and yellow. Myosin minifilaments and α-actinin are also present in the simulations but are not visualized.

4.3. Results

4.3.1. Filament branching versus extension – Arp2/3 driven changes dominate filament length and network organization

Representative snapshots shown in Figure 4-2 show clear differences in actin network organization that result from changing Arp2/3 and Ena concentrations. We quantified filament length distributions to define the specific changes resulting from varying Arp2/3 and Ena (Figure 4-3A). Parent and offspring filaments were considered as two different filaments when calculating filament length distributions. As Arp2/3 concentration is increased, Arp2/3 turnover causes increased offspring filament nucleation (Figure 4-3B). As the total actin in the reaction volume is held constant, this results in an increased abundance of short filaments. Changing Ena concentration, in contrast, has a limited impact on filament length distribution. At [Arp2/3]<10nM, Ena's addition caused Ena-driven filament extension leading to increased abundance of longer filaments and decreased abundance of shorter filaments. As Ena concentration increases, we see a steady increase in the fraction of filament plus ends stabilized by Ena (Figure 4-3C). At Ena concentrations of 25nM and 50nM, we see that Ena-driven extension is limited by actin availability, causing minimal changes to filament length distributions. At [Arp2/3]≥10nM, changing Ena concentration has a limited impact on filament lengths.

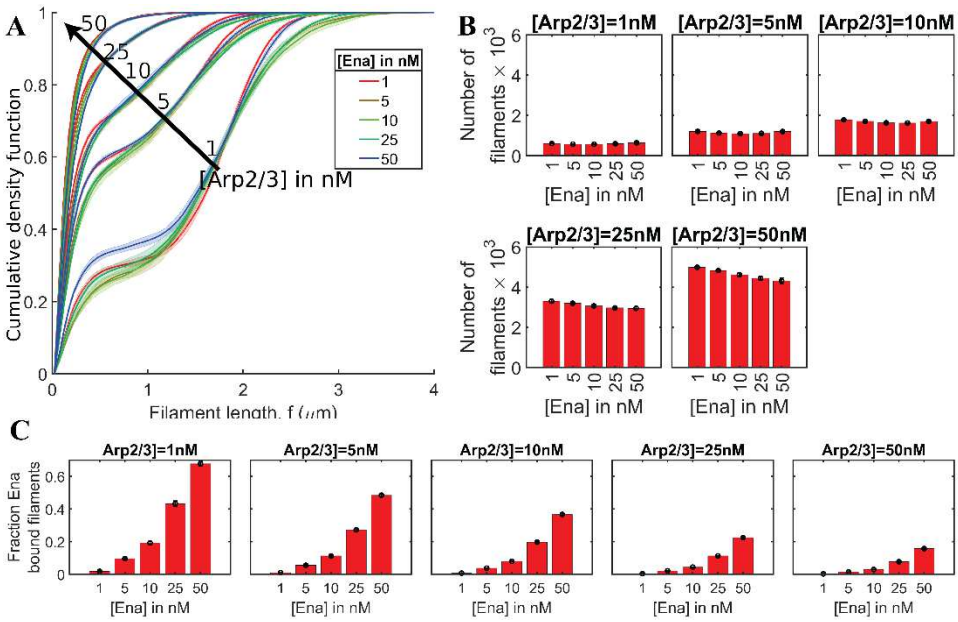

Figure 4-3 Arp2/3 dynamics determines filament organization of growth cone mimics. A. Filament length distributions are shown as cumulative density functions at various Arp2/3 and Ena concentrations. Distributions are colored based on Ena concentration, while the Arp2/3 concentration is overlayed on the graph. Solid lines and shaded areas represent mean and standard deviation, respectively, from multiple replicates. B. Bar graph shows the number of filaments when Ena concentrations are changed at each Arp2/3 concentration. Error bars show standard deviation.

To understand how differences in filament lengths alter network organization, we looked at actin concentration in 100nm thick discs along the cylindrical reaction volume axis (Figure 4-4). The profiles were obtained by peak-aligning the actin profiles from the last 50s of the trajectories. Increasing Arp2/3 at any given Ena concentration leads to drastic changes in actin profiles characterized by multiple peaks spread across an increasing fraction of the reaction volume. At low Arp2/3 concentrations, in contrast, increasing Ena modestly broadens the width of a central peak in the actin

distribution. To understand the relative effects of Arp2/3 and Ena on the actin distribution profiles, we measured the spread of actin around the peak. Figure 4-5

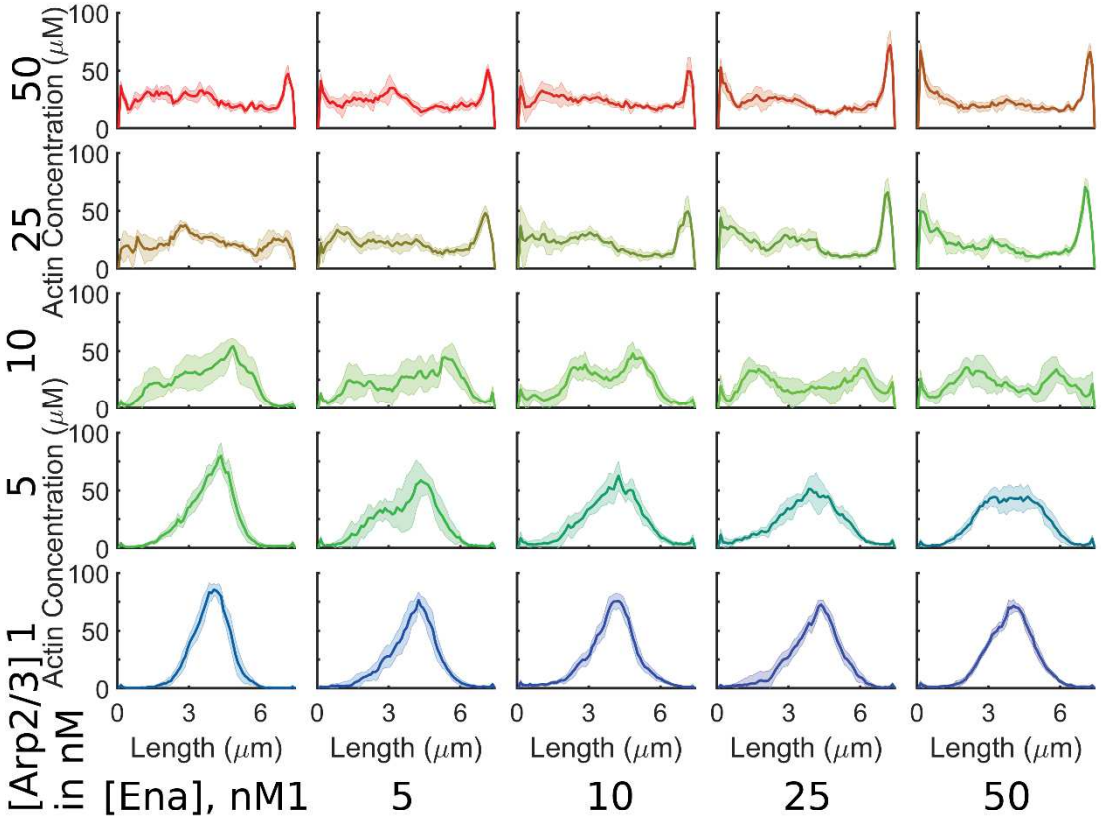

Figure 4-4 Axial actin concentration profile reveals Arp- and Ena-driven differences in actin organization. Actin concentration along the length of the reaction volume of the final snapshots (2000s) from all replicates at Arp2/3 and Ena concentrations are plotted.

shows box plots of actin spread around the peak. Actin spread was defined as the sum of standard deviations on either side of the actin peak. We studied the effect of Arp2/3 and Ena on actin spread using the Wilcoxon rank-sum test. We find that in 94% (47/50) pair-wise comparisons, increasing Arp2/3 concentration at any particular Ena concentration increases the median spread of actin profile at 5% significance. Similarly, at a given Arp2/3 concentration, increasing Ena increases actin spread in 86% (43/50)

of comparisons. We note that at the two highest Arp2/3 concentrations, actin is already distributed roughly homogeneously across the entire volume, limiting the possibility of further spread. We also note that increasing Arp2/3 increases actin spread over a multi-micron length scale at any given Ena concentration, whereas the range of actin spread from varying Ena is smaller than 1um in all cases. Thus, these results suggest that actin organization and distribution are dominated by Arp2/3, with the effects of Ena being far more modest.

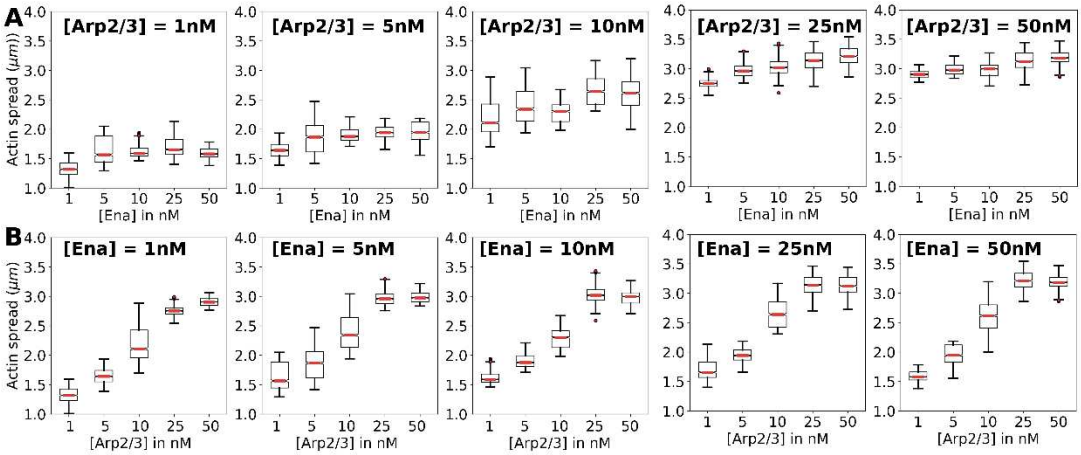

Figure 4-5 Actin spread from the last 200s of trajectories reveals Arp2/3 dependent actin organization in axon mimics. Actin spread was measured as the sum of left and right standard deviations from the actin distribution peak. Each panel shows actin spread at various Arp2/3 concentrations at a given Ena concentration (mentioned above each panel).

We then proceeded to understand if the actin organization observed in our simulations is due to boundary effects. As simulations in 15µm length scales are computationally expensive, we chose to simulate a subset of Arp2/3 and Ena concentrations we have explored so far. As Abl signaling simultaneously promotes Arp2/3 activity and inhibits Ena activity [230], we chose to simulate actin networks at the conditions specified

along the falling diagonal of Figure 4-2 inside reaction volumes that were 15μm long and 1μm in radius. Thus, we explore network organization by simultaneously decreasing Arp2/3 and increasing Ena concentrations. We see that under conditions that mimic elevated Abl expression, i.e., under ([Arp2/3],[Ena]) pair values of (25,5) and (50,1), actin spreads homogeneously throughout both the short and long reaction volumes (Figure 4.6 i-iv). In the other conditions with Arp2/3 and Ena concentration pair values of (10,10), (5,25), and (1,50), we see that actin is highly condensed at certain parts, evidenced by peaks in the axial actin distributions. Additionally, we also see that the width of actin peaks is similar in actin distributions from both 7.5 μm and 15 μm reaction volumes. Finally, the overall distribution of actin within 15 μm long reaction volumes under all conditions studied appears to be combinations of actin profiles obtained at 7.5 μm length scales. These similarities support the argument that the actin distributions obtained at 7.5 μm length scales contain scale-free features that are also observed at longer length scales.

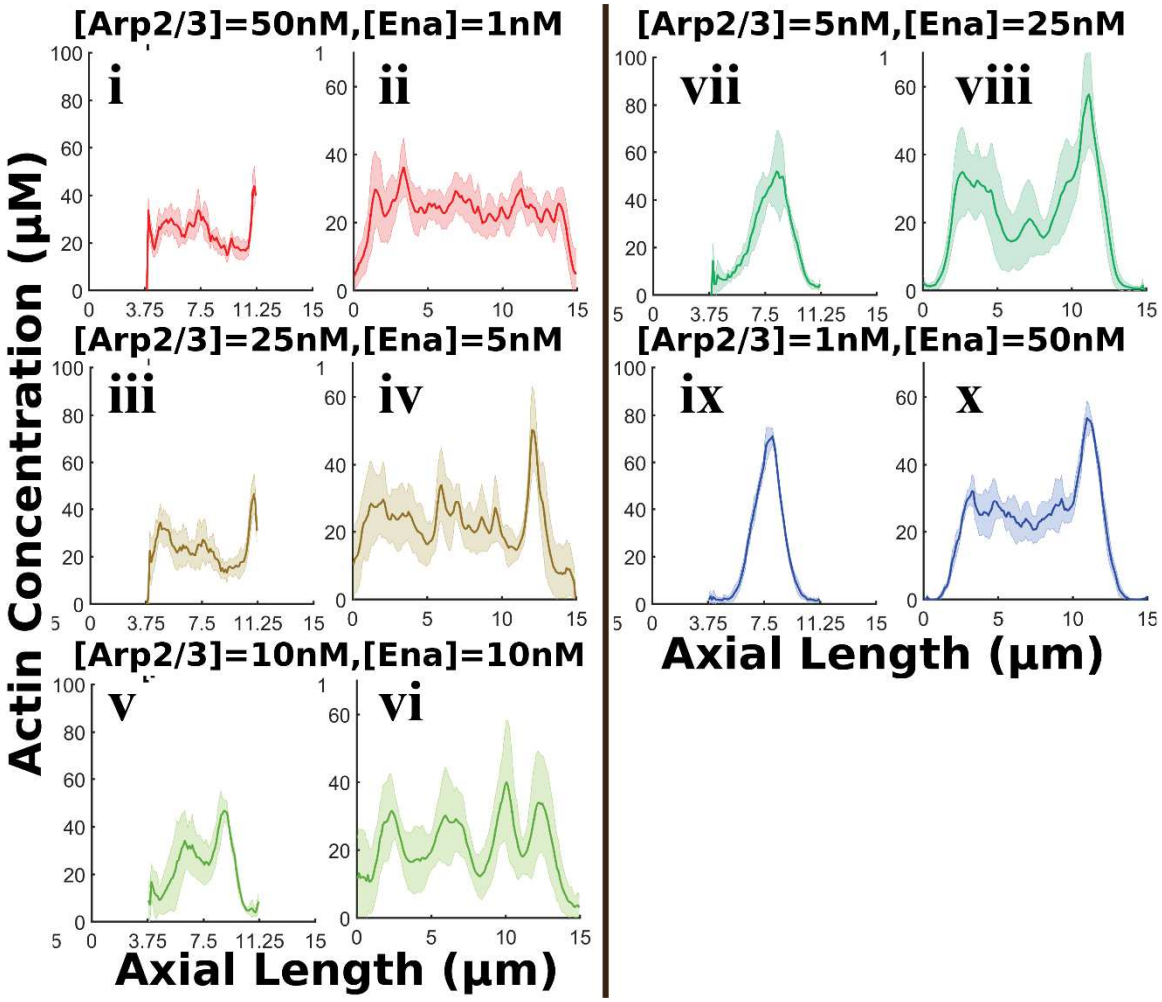

Figure 4-6 Simulations at longer length scales preserve salient features found at lower length scales. In each row, the left panel (i,iii,v,vii,x) shows peak-aligned actin profiles from simulations in 7.5µm long reaction volumes, while the right panel (ii, iv, vi, viii, x) shows peak-aligned actin profiles from simulations in 15µm long reaction volumes. The peak-aligned profiles from 7.5 µm long reaction volumes were translated appropriately to enable easy comparison to profiles obtained from simulations in 15µm reaction volume.

4.3.2. Networks corresponding to elevated Abl activity are composed of weakly interacting actin filament communities

Having found that Arp2/3 modifies local parameters of actin network architecture more robustly than Ena, we asked how Arp2/3 activity alters the global network organization of actin. To answer this, we investigated the modularity changes to actin architecture resulting from changes to Arp2/3. Modularity is a graph theoretical measure of networks to quantify how well the network components are divided into modules. Graph theory techniques have been proven helpful in understanding network architecture.[234,235] We constructed graph representations of inter-filament contacts by representing actin filaments as the node and weighting the edge by the total number of the linker, motor, and brancher contacts between two filaments. We then compartmentalize the filaments into domains by optimizing the Louvain-Modularity metric.[236] More details about the modularity metric can be found in Appendix C, Section C-3. This algorithm was used to identify communities within the actin network. Communities are sets of actin filaments that interact more closely with other filaments within the set than with the rest of the filaments in the network. We find that increasing Arp2/3 concentration increases the number of communities and decreases community size, suggesting that actin is organized into weakly interacting communities. (Figure 4-7A and B). This altered organization of actin filaments also affects the amount of actin in each cluster, as shown in Figure 4-7B.

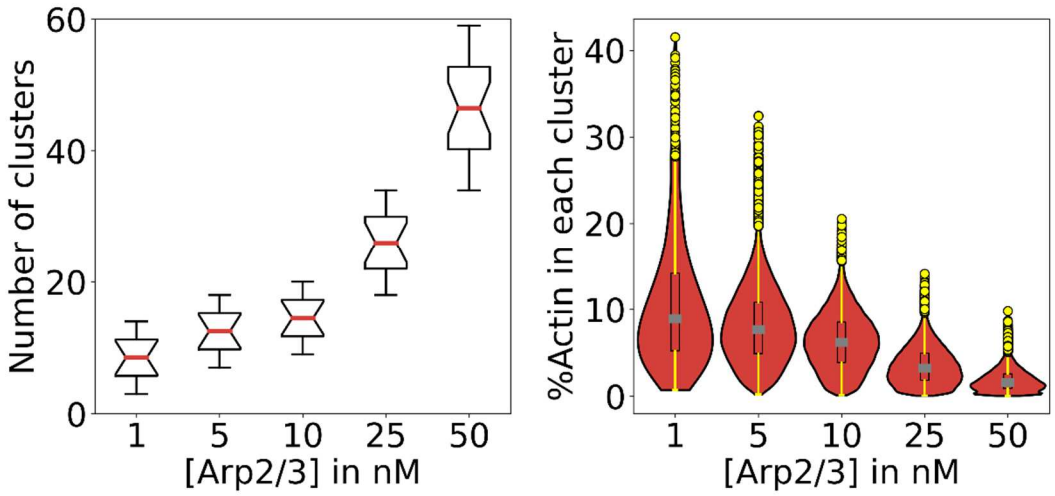

Figure 4-7 Arp2/3 activity alters network organization in favor of weakly coupled communities of filaments. A. The number of actin filament communities detected by the Louvain-Modularity optimization algorithm is plotted as a function of Arp2/3 concentration at [Ena] =25nM. Box and whisker plots show median (red), quartiles as blue boxes, interquartile range (black whiskers), and outliers (red crosses). B. The fraction of F-actin in each cluster has been plotted as a violin plot. The box plot shows the 25-75 percentile represented as a box with the median shown as gray lines. Whiskers are shown as solid yellow lines with outlier data points represented as yellow circles

4.3.3. In-silico networks capture essential features of experimental actin profiles

The simulations above were designed to model the properties of actomyosin networks. A key question, however, is how similar these are to actin distributions observed experimentally. To obtain experimental representations comparable with the simulation results shown in Figure 4-4, we normalized the intensity profiles obtained from fluorescent imaging of actin in single WT axons for 30 minutes (sampling frequency = 3min), aligned the profiles by the position of maximum actin intensity in each time point and averaged the intensity for a 15μm span around that peak position.

This value was motivated by the experimental observation that the actin peak width in the growth cone is ~15μm in WT axons (defined as the square root of the second moment of the distribution).[225] This procedure was repeated for 14 WT axons (presented as a gallery in Figure 4-8A, showing the median and median absolute deviation for each axon). Figure 4-8B shows actin profiles from MEDYAN simulations at all Ena concentrations for [Arp]≤10nM (Subset of profiles shown in Figure 4-4). Comparing against the experimentally observed actin, we see striking similarities. Experimentally observed profiles are composed of a high actin concentration resulting in a dominant peak with a steady decrease in actin intensity around the peak. In contrast, it is clear from inspection of Figure 4-4 that simulations with higher levels of Arp2/3 do no bear any substantial resemblance to the experimentally observed axial actin distributions. Even though our simulations approximate Abl signaling by just the downstream effector concentrations and do not include any neuronal polarization mechanisms, the actin profiles obtained from our simulations at [Arp] < 10nM bear a striking similarity to the experimentally observed features of actin organization discussed above. This similarity is also evident in overlays of the individual profiles from the constituent experimental profiles and simulation profiles (Appendix C, Figure C-6).

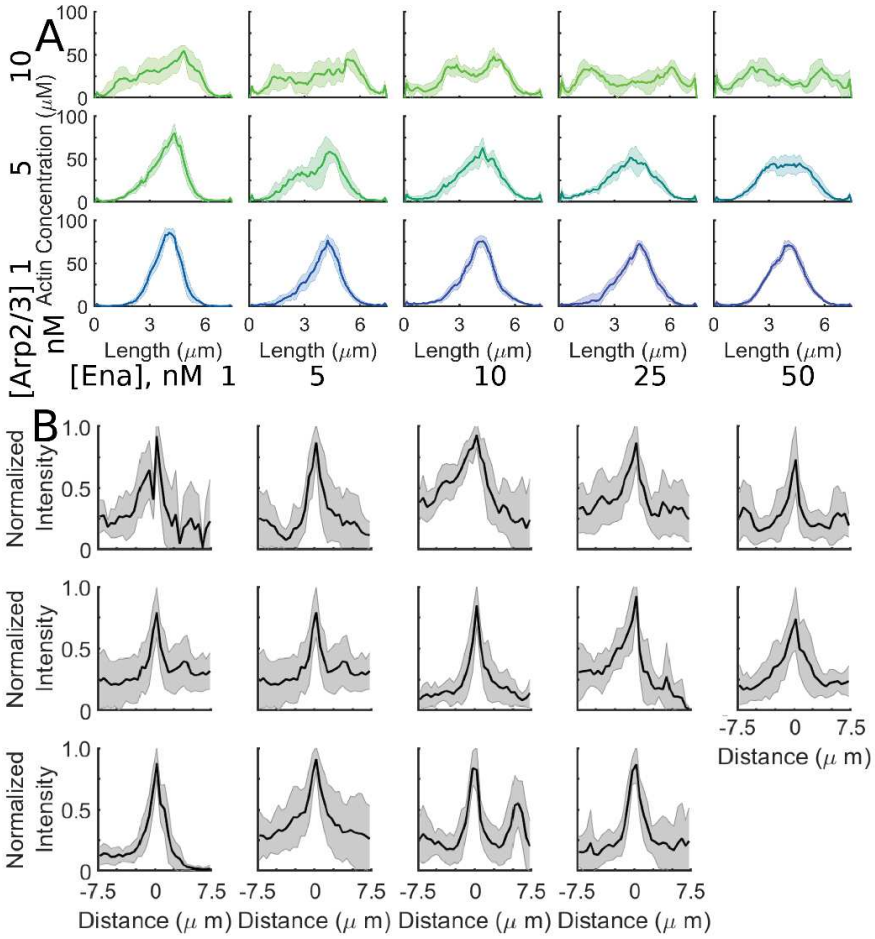

Figure 4-8 Simulations capture features of axonal growth cones observed in experiments. A. Peak-aligned actin concentrations are plotted as a function of distance along the cylinder axis. Arp2/3 concentrations are mentioned to the left, while Ena concentrations are labeled at the bottom of the panel. The solid line and shaded area represent mean and standard deviation, respectively. B. Actin intensity distribution in 14 WT Abl axons. Each sub-panel shows the median and median absolute deviation of peak-aligned actin profiles from the first 30 minutes of imaging a WT axon. Experimental actin intensity distributions were truncated 7.5 μm on either side of the peak according to experimental determination of growth cone width.

We next sought to obtain a quantitative measure of these distributions to test the apparent similarity in their profiles. Previously, wavelet analysis was applied to the experimental actin distributions in wild-type axons and in axons with gain- or loss-of-function of Abl to quantify the spatial structure of the experimental 1-D actin

distributions. We, therefore, compared how the differences in the spatial structure were observed experimentally with increasing and decreasing Abl activity compared to the trends in spatial structure obtained in our simulations with increase and decrease of the primary Abl target, Arp2/3. We wished to understand the basis for the apparent separation of the longitudinal actin distribution into discrete peaks with increasing Arp activity. We, therefore, analyzed pair correlation profiles (also known as radial distribution functions) of actin profiles from different Arp2/3 and Ena concentrations (Figure 4-9). These profiles were calculated by projecting monomer coordinates along the cylinder axis. Therefore, as two monomers can have the same coordinate along the cylinder axis, the radial pair correlation functions (Figure 4-9) are non-zero at 0μm. The pair correlation function informs us of how the linear density (μM/μm) scales as a function of distance away from a reference point compared with bulk linear density. We see that at Arp2/3 concentrations of 1nM and 5nM, F-actin abundance decreases monotonically with increasing distance. Additionally, as Ena concentration is increased at these levels of Arp2/3, pair correlation decays to 1.0 (when bulk density and local density match) at slightly larger length scales. This result is consistent with the findings from the actin spread that actin spread increases with increasing Ena at low Arp, as we discussed earlier (Figure 4-5A). At higher Arp2/3 concentrations, pair-correlation shows reduced dependence on distance, consistent with the relatively flat axial actin distribution profiles across the reaction volume (Figure 4-9). Changing Ena has very little effect on the pair correlation function profiles, again consistent with actin spread data.

Conversely, when Arp2/3 concentration is increased at any given Ena concentration (Figure 4-9B), we see that linear actin densities are above bulk value (g(r)>1) over longer spans consistent with increased actin spread observed earlier (Figure 4-5B). Specifically, the effect of Arp2/3 spans the entire reaction volume, also consistent with the finding that Ena increases actin spread only locally, at short range, whereas Arp2/3 increases spread globally, across the entire volume. Finally, we see that at [Arp2/3]=10nM, the pair correlation function shows one auxiliary peak suggesting multiple domains of actin organization. At higher Arp2/3 concentrations, actin profiles decay monotonically with no significant features. We would like to point out that the patterns in order parameters measured along the cylinder axis, such as actin spread and pair correlation function, are a consequence of the actin fragmentation explored in Chapter 3. Thus, at Arp2/3 concentration, actin is distributed differently along the reaction volume axis, consistent with experimental observations. We would elaborate on the similarities between simulations and experiments in the Discussion section.

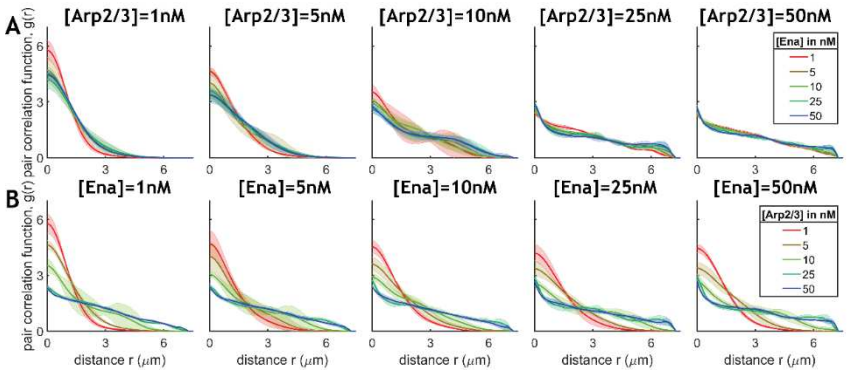

Figure 4-9 Pair correlation function of actin intensity reveals Arp dependant fragmentation. Mean (solid line) and standard deviation (shaded area) are plotted at various

Arp2/3 (top row) and Ena (bottom row) concentrations at a given Ena and Arp2/3 concentration, respectively.

4.3.4. Actin communities at elevated Arp2/3 networks are mechano-chemically disconnected

To understand the functional relevance of actin communities found through modularity analysis, we studied mechanical and mechano-chemical responses to perturbation through two different in-silico experiments. First, we asked if the weakly coupled communities that we find are mechanically disconnected. To answer this question, we simulated actin networks generated from studies discussed above under the following constraints. We chose the final configurations of the 2000s long simulations presented above as the initial conditions for the current study. To study just the mechanical response of the system, we prevented chemical dynamics in filaments (polymerization, depolymerization, branching, and unbranching). Such networks were then subjected to mechano-chemical perturbations from myosin and crosslinker activity only in a 500nm "active zone." The active zone was chosen to be the region of the highest actin density. Myosin and crosslinker kinetics are quenched outside the active zone, thereby freezing the myosin and crosslinker molecules in the bound state. Parameters of the simulation can be found in Appendix C, Table C-2. This simulation was inspired by previous experimental studies to study correlation in linear actin networks.[237] Looking at the velocity of filaments from the last 100s of trajectories, we see that filaments move within the active zone and in a region adjacent to it (Figure 4-10). Specifically, in low Arp2/3 networks, actin filament movement extended in regions flanking the active zone

over longer distances than filaments in high Arp2/3 networks. The difference in velocity decay rates between low Arp2/3 and high Arp2/3 networks demonstrates that increasing the number and decreasing size of filament-filament contact-based communities is associated with a decreased mechanical connection within the actin network.

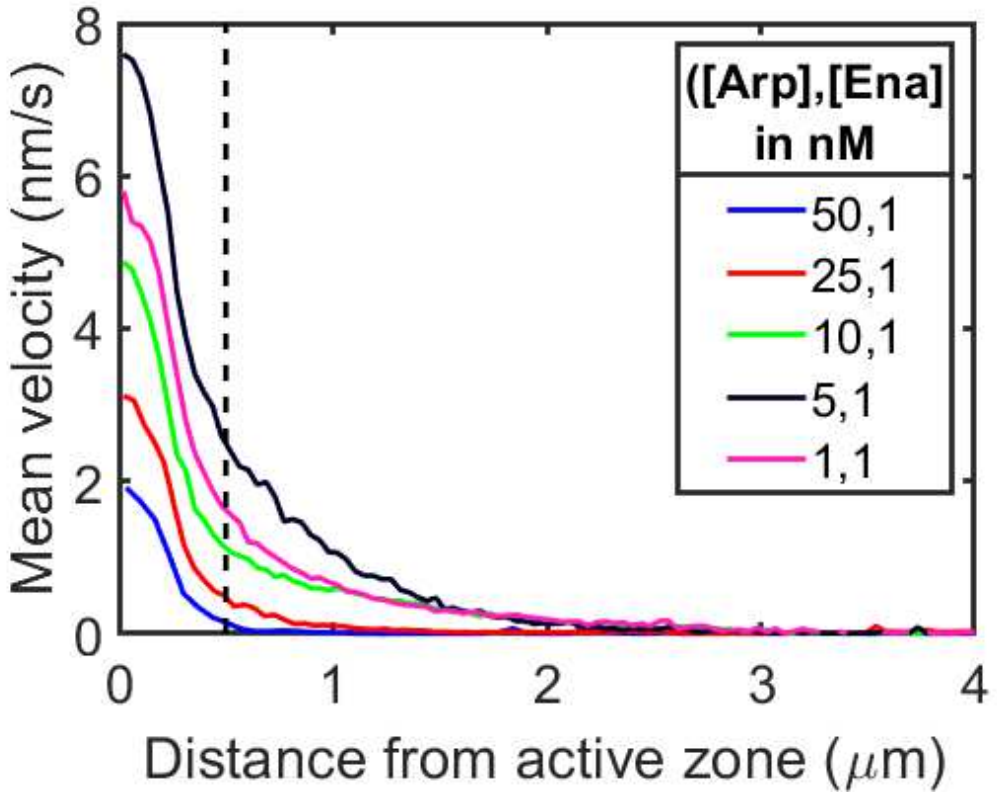

Figure 4-10 Mean filament velocity from spatially-localized myosin-driven perturbations reveal signs of mechanical fragmentation. Mean actin velocity calculated from displacements in the last 100s of trajectory at various Arp2/3 concentrations is shown. The dotted line represents the active zone boundary.

As actin networks are chemically active, we also studied the effect of fragmentation within the actin network by studying the mechano-chemical response of the actin network to mechanical perturbation. Using the final configuration of filaments, linkers,

motors, and branchers from our earlier simulations as the initial conditions, we exert an external force on the actin network using a functionalized "AFM tip" mimic. The AFM tip mimic is functionalized with 50 stabilized actin filaments of 540nm length, it is introduced into the actin network, and it is allowed to incorporate into that network. With its associated stabilized actin filaments, the AFM tip mimic was then moved by a distance of 1μm over a 5.0s time scale. As a result, tensile forces are transmitted across the actin network through contacts between stabilized filaments in the probe and the actin filaments in the network. Chemical interactions such as filament treadmilling and inter-filament chemical interactions from branching, myosin, and crosslinker kinetics were activated throughout the reaction volume. We then study the response of the network to the force transmitted through the motions of the AFM probe. Figure 4-11 shows snapshots at various time points showing changes to the actin network during the probe displacement. We see that network with [Arp2/3]=1nM moves coherently as a single connected unit in response to the external force. On the other hand, in networks generated with [Arp2/3]=10nM, AFM pulling exacerbates the disconnect between the two actin domains preventing effective transmission of tension across the entire network. Taken together, the results from the perturbative simulations suggest that elevated Arp2/3 levels result in network architecture into domains that are mechano-chemically disconnected.

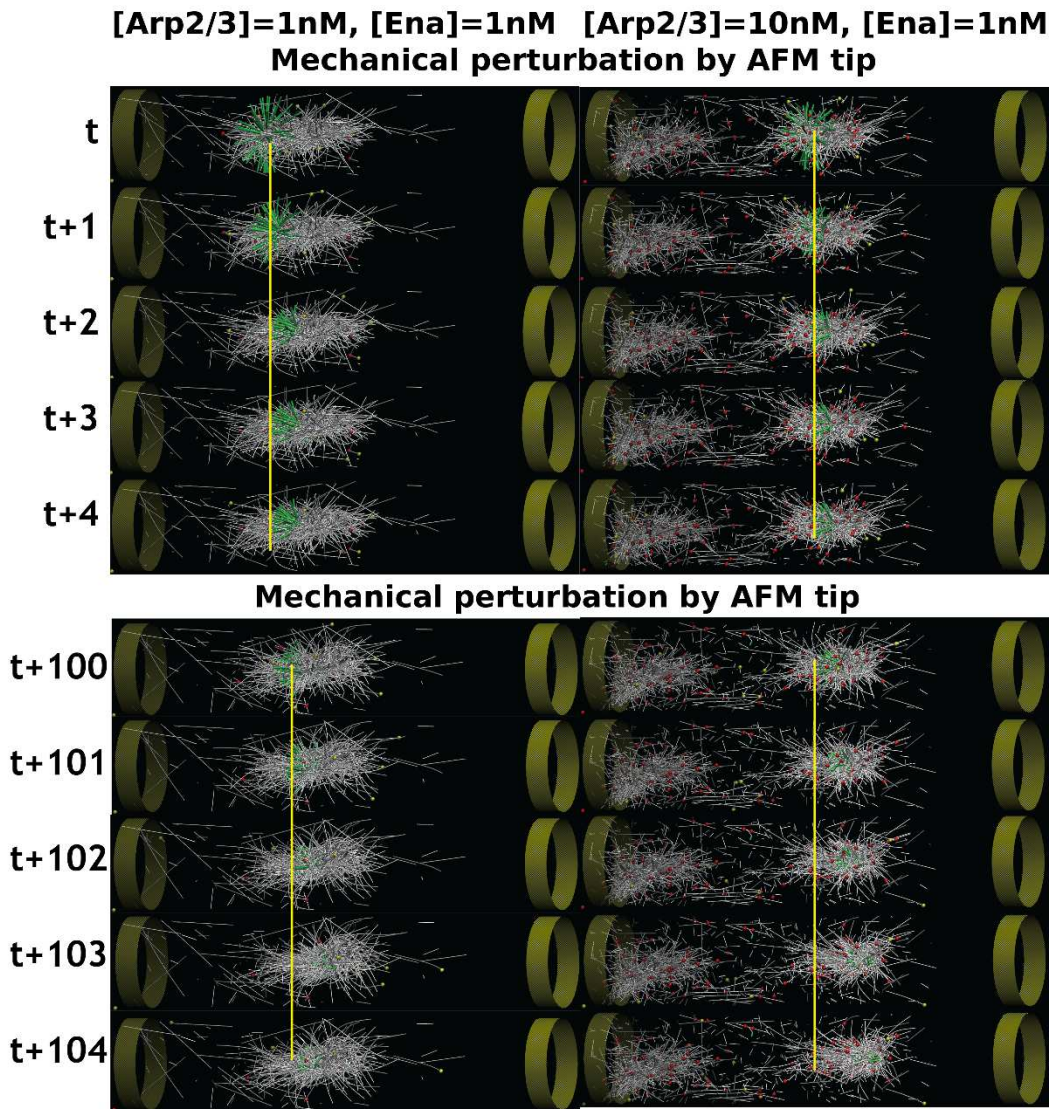

Figure 4-11 Mechanochemical response of actin networks to AFM mimic driven mechanical perturbations reveal fragmentation in intra-network signal transduction. Time series of snapshots showing actin filaments in white, Arp2/3 molecules (red), and Ena molecules (yellow) is shown. AFM tip is represented through the functionalized tip with 50 actin filaments (green). The solid yellow line represents the position of the tip before AFM-driven displacements are exerted.

4.4. Discussion

The axonal growth process is mediated by cytoskeletal modifications resulting from signaling cascades. Abl is a crucial signaling molecule controlling the axonal growth process in the TSM1 neuron by promoting Arp2/3 activation and inhibiting Ena activity. As it is challenging to resolve actin's filament level organization experimentally, we decided to employ MEDYAN, a computational model that can model actin filaments under monomeric resolution subject to relevant mechano-chemical complexities.

We determined relevant concentration ranges and employed experimentally determined kinetic rates to generate in-silico growth cone mimics. We find that Arp2/3 is a stronger modulator of both filament length and network organization than Ena. Thus, cytoskeletal reorganization resulting from dynamic Abl levels could be primarily determined by changes to Arp2/3 levels in axons. We see that both Arp2/3 and Ena increase the actin network's spread, albeit across different length scales. Additionally, we see that actin profiles generated at Arp2/3 concentrations 1nM and 5nM capture key actin organization features found in experimental images of WT Abl axons. Interestingly, we capture essential features of WT axons despite simulating networks without any constraints to enable polarization of networks.

Given that Arp2/3 plays a dominant role in actin organization, we then understand how filament-filament contacts are altered. We represent the actin network as a graph structure with actin filaments as the nodes and filament-filament contacts as edge weight. We then uncovered the community architecture of the actin network by

optimizing the Louvain modularity metric. We see that under high Arp2/3 activity, the network is composed of a higher number of communities than at low Arp2/3 conditions. The change to community structure suggests that underlying actin filaments are organized into sets that interact strongly amongst each other and are weakly coupled to the rest of the network.

While such novel graph theoretical approaches have been employed in earlier studies[202,235], the physical and potential biological consequences of such findings have been elusive. We, therefore, establish a framework to understand the functional consequences of structural changes in the actin network. To this end, we designed two perturbative computational studies to understand mechanical and mechano-chemical consequences of the decoupled actin organization at high Arp2/3 concentration (by extension, mimicking high Abl activity). MEDYAN simulations were initialized at the final configurations generated in our earlier simulations, and networks were evolved by studying filament velocity in response to myosin walking within a defined active zone. We find that as Abl activity increases, filaments transmit force, and therefore information, over shorter distances as at lower levels of Abl activity.

Additionally, we also studied the differences in the network's mechano-chemical responses to an external tensile force applied over short time scales. We see that networks corresponding to Arp/Ena combinations that resemble wild-type actin distributions are displaced en-masse as a single, connected unit in response to the force exerted by AFM probe, while networks generated at high Arp, as expected from hyper-activation of Abl activity, behave as disconnected networks. This addresses the

longstanding problem in axonal guidance on how the actin cytoskeleton in the growth cone organizes to move as a single entity under wildtype conditions and how Abl overexpression causes guidance errors. In our simulations, the networks generated under low Arp2/3 concentrations are organized similarly to wild-type axons imaged in the experiments and behave coherently to perturbations suggesting a coordinated information transfer through the network. On the other hand, the filaments from high Arp2/3 concentration are weakly coupled, and the network organization is expected to limit coherent information transfer within the actin network. We hypothesize that these differences in properties might explain the increased developmental errors and fragmentation observed in axons under over-expressed Abl conditions.

Experimental evidence suggests that changes to Abl levels alter growth cone width and also peak wavelet length scales. This study has helped us understand the sub-micron architecture of actin that can explain the experimental observations. Simulations reveal that actin is organized into communities that are weakly coupled. Considering evidence from the previous chapter on actin domain organization, we see that actin networks are organized into high-density actin domains that are weakly coupled to one another. Thus the network architecture is a combination of domain size and domain-domain spacing. The two experimental metrics listed above measure a combination of the two actin domain properties.

Another critical question is the source of Abl loss of function phenotypes. At the lowest levels of Arp2/3, simulated actin networks showed maximal condensation of actin, consistent with the contraction of the actin second moment in Abl loss of function

conditions. So, we hypothesized in our earlier experimental study[225,229] that increased activity of Ena resulting under Abl loss of function conditions might lead to the local collection of F-actin into the individual actin peaks, potentially stimulating actin fragmentation. However, in our simulations, we do not observe obvious evidence for the degree of short-length scale fragmentation as reported in experiments characterized by the generation of small foci of intense actin intensity. The reason for this is not apparent. Such differences can be accounted for, in part, by a more detailed model of Enabled. As Ena tetramer's bundling activity has been found crucial in filopodial bundles [23,120], we suggest that the differences in actin organization might be more evident using a detailed model of Ena as a tetramer capable of binding to multiple actin filaments.

4.5. Conclusion

We studied the downstream effects of the Abl signaling pathway using computer simulations in MEDYAN. We find that Abl alters network architecture primarily through changes to Arp2/3 abundance. We identify specific changes to actin architecture resulting from changes to Arp2/3 and identify differences in mechano-chemical signal transduction by studying actin networks' responses to perturbations. Taken together, these and other findings from this work provide a molecular-level picture of how axon morphogenesis arises from the biophysics of actin networks. In as much as all axonal signaling molecules have to converge on the same, restricted set of elementary dynamic processes of growth cone actomyosin dynamics interrogated here,

we believe that this picture applies not just to Abl-dependent axon patterning mechanisms but also to other signaling modules that guide neuronal morphogenesis.

Chapter 5 Discussion and Outlook

In this thesis, we explore the self-assembly processes driven by both linear and dendritic actin filaments and highlight the cooperation between them within axonal growth cones. Using MEDYAN, an advanced mechanochemical forcefield, we simulate actin networks along with the necessary actin-binding proteins. This has given us biophysical insights into several biological phenomena. As the structure of cytoskeletal structures plays a key role in mechanotransduction, this thesis helps understand the structure-function relationship of the actin cytoskeleton.

Cells spontaneously alter chemical fluxes of actin and a cohort of actin-binding proteins to remodel the actin cytoskeleton. In Chapter 2, we looked into the role that crosslinkers, myosins, and treadmilling rate play in the stability and active remodeling of bundles. The resultant network morphologies give us a dictionary of states that are favored at steady-state. By devising a novel unsupervised learning algorithm, we identify the underlying patterns among the structures that suggest that the bundles broadly sample three unique network morphologies. With our knowledge of specific parameter ranges in the state space that lead to bundle stability, we can now explore the role that focal adhesions play in facilitating stress fibers as mechanotransducers. Focal adhesions are complexes of transmembrane proteins such as integrins and proteins such as vinculin, talin, and paxillin adjacent to the plasma membrane.[238–241] Simulation of such complex mechanochemical events requires explicit membrane and transmembrane proteins modeling. Recently, a member of our lab (Haoran Ni) has

been constructing reaction-diffusion models on semi-flexible membranes to understand the biophysical origins of cytoskeletal-membrane coupling.

In Chapter 3, we investigated the spatial organization of the actin network at various Arp2/3 concentrations. Analyzing spatial density fields of actin, we found key differences in actin organization at high Arp2/3 concentrations that result in a spatially fragmented actin network. Similar behaviors of network organization have been observed in linear networks where additionally, the size of fragmented domains grows with a characteristic power-law behavior.[177,181] Such behaviors are reminiscent of phase transitions observed in polymers in unfavorable solvents.[206] Such transitions have been observed in filamentous actin systems as sol-gel transitions, and the role of crosslinkers and myosins in regulating this transition has been established. Here, we find that changing Arp2/3 and Ena can help tune the spatial scale of the gels. Our results suggest a novel mechanism by which biochemical signaling can trigger cytoskeletal remodeling in cells by modulating the nature of sol-gel transitions. Further analysis of such active coarsening behaviors will help us understand the fundamental physical principles behind actin organization in cells. Our simulations suggest that networks under low Arp2/3 concentrations are sensitive to changes in myosin activity while high Arp2/3 networks respond weakly to changes in myosin activity. This hypothesis can be tested experimentally using reconstituted purified networks of dendritic actin networks at various myosin concentrations.

In Chapter 4, we looked at the cooperation between Arp2/3 and Ena in determining axonal architecture. While we identified unique features that explain the

actin architecture observed in wild-type and overexpressed signaling states, we did not find mechanisms of fragmentation observed under Abl loss of function. The effects could be explained, in part, by a more detailed model of Ena tetramer. In our study, Ena is modeled as a barbed end binding protein that accelerates actin polymerization. Nevertheless, experimental evidence suggests that each subunit in the tetramer can interact with the actin barbed end or bind along the sides of an actin filament. We could employ a more detailed model where Ena acts as a tetrameric actin-binding protein to account for this mechanism. Thus, we can study if the role of Ena as a multifilament binding protein can help explain network fragmentation observed under Abl loss of function *in vivo*.

Additionally, our studies do not include mechanisms of polarization which is crucial for directional growth. Recent evidence suggests that microtubules play a crucial role in establishing neuronal polarization. More specifically, microtubule-actin crosslinks act as ratchets that prevent retrograde flow of actin into the cell body. This mechanism can be explored in MEDYAN. Finally, we can also explore the role of spatial gradation in Abl signaling within growth cones. As Abl activation happens in response to extracellular cues detected by transmembrane protein, Abl activity could decay monotonically from the axonal tip to the cell body. We can model a spatially heterogeneous model for Abl activation and explicitly couple local Arp2/3 and Ena activity to Abl abundance. This will help us gain more critical insight into the sub-micron architecture of actin filaments within growth cones.

To push the envelope on our current understanding of actin networks, we need to continue improving the performance of MEDYAN to simulate cell-scale networks. Stochastic simulations of such complicated chemical networks are computationally prohibitive. To overcome this, we can use a constant time-step Gillespie algorithm where all compartments in the system can be evolved in parallel under a predetermined time step. Such a scheme can also enable us to decouple reaction and diffusion operators of the master equation under carefully chosen time-steps. Such efforts are currently underway in a joint project led by Haoran Ni and me from the lab.

Appendices

Appendix A. Supporting Information for Chapter 2

Supporting Figures

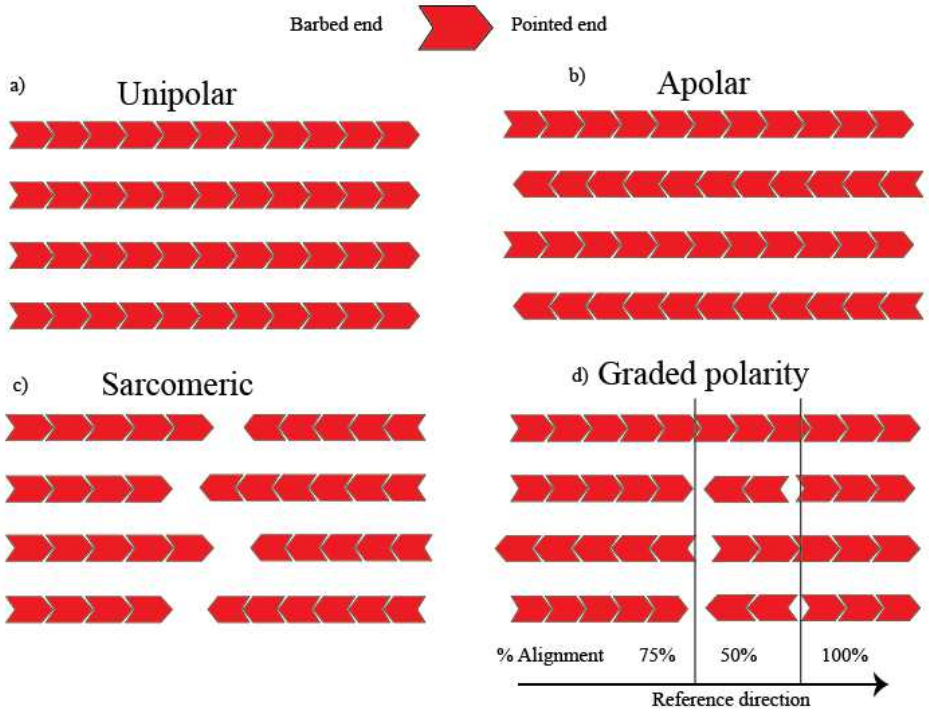

Figure A-1 Schematic is depicting different modes of actin bundle organization. Actin monomers with barbed and pointed end polymerize to form long filaments. a) Unipolar bundles have polarity sorted barbed and pointed ends while c) Sarcomeric bundles have polarity sorted pointed ends. b) Apolar bundles have zero net polarity while d) graded polarity bundles have varying degrees of polarity along the length of the bundle.

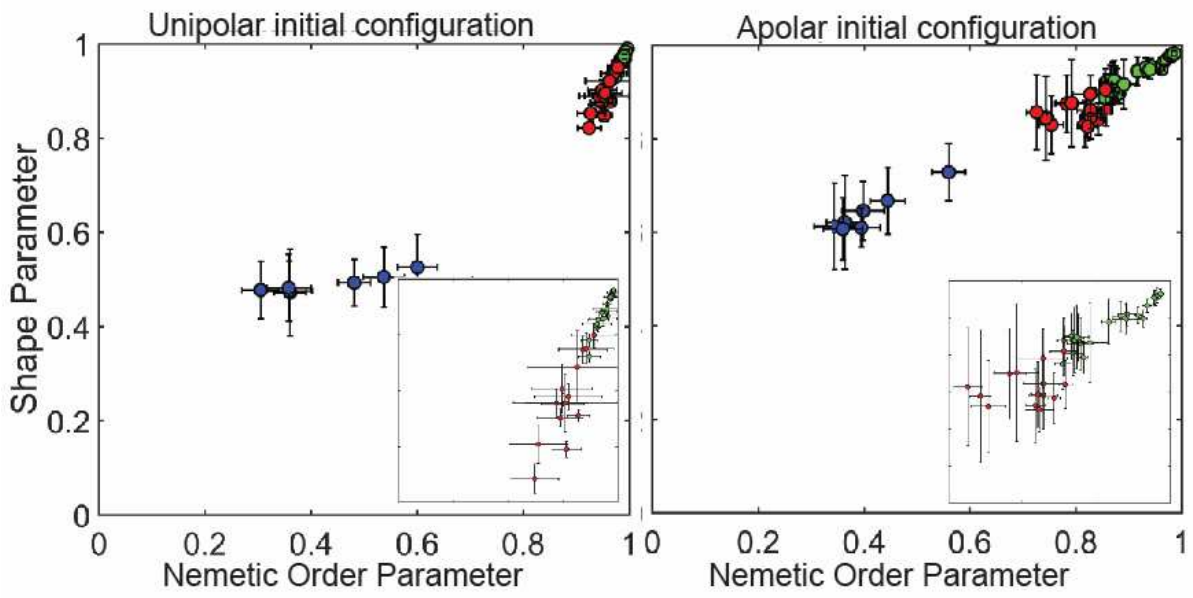

Figure A- 2 Nematic order and shape parameters highlight the differences between BL, ABI, and AL morphologies. Mean and standard deviation of nematic order parameter and shape parameter from the last 500s from networks simulated at 42 different mole ratio pairs under (a) unipolar and (b) apolar initial conditions are shown. BL, ABI, and AL morphologies are colored respectively in green, red, and blue. Inset shows zoomed-in plots of shape and order parameters to highlight differences between BL and ABI morphologies. Please refer to Supporting Methods (sections A.3 and A.4) for the definitions of order and shape parameters.

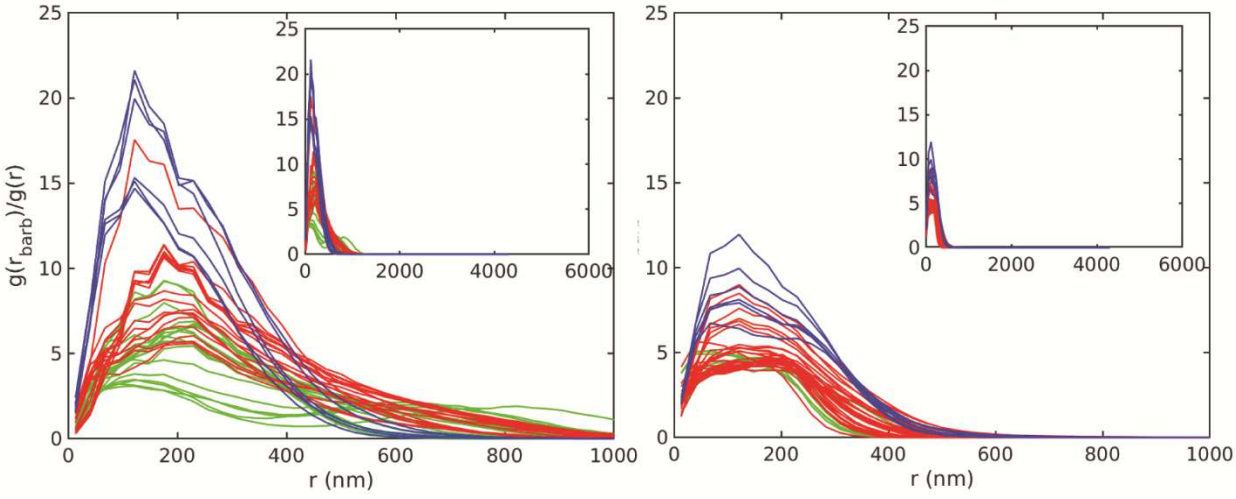

Figure A-3 Radial distribution function-based order parameter for different network morphologies observed in non-treadmilling networks. Profiles of $\boldsymbol{g(r_{barb})/g(r)}$ for 42

different mole ratio (M: A,α:A) pairs are plotted for unipolar (left) and apolar (right). In studies by Freedman et al. [158], this order parameter delineates polarity sorted networks. BL, ABI, and AL morphologies are colored respectively in green, red, and blue. Inset shows the complete profile of the distribution function. Using the last 500s of trajectories, each actin segment was interpolated to get a fine grain network structure.

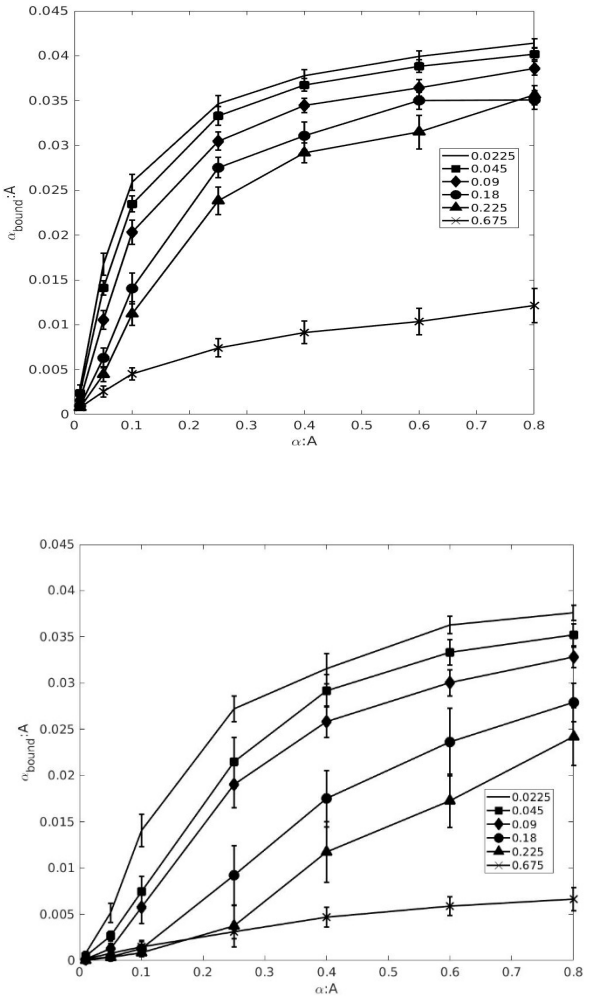

Figure A-4 Mole ratio of crosslinkers bound to actin network at different total crosslinker mole ratios. Mean and standard deviation bound crosslinker mole ratios (αbound: A) for networks evolved from both unipolar (left) and apolar (right) bundle configurations at different myosin mole ratios (M: A, legend) are shown. The last 500s of the trajectories were used to calculate bound crosslinker mole ratios. As M: A is increased, the average number of linkers bound to the network reduces.

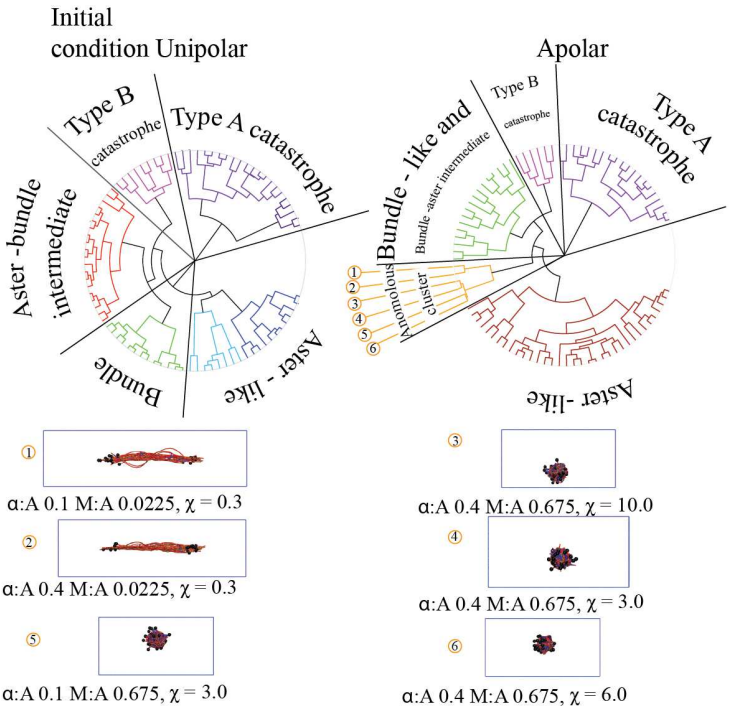

Figure A- 5 Dendrograms from clustering actin networks from unipolar (left) and apolar (right) initial conditions. Dendrogram clades are colored based on network morphology. Type A catastrophe is characterized by a poorly connected network with very low packing density, while B catastrophe is characterized by a connected network with moderate packing density. Six of the resulting clusters from apolar conditions were incorrectly clustered to an anomalous cluster. They contained spherical asters and apolar bundles in the same clade. Representative snapshots of members within the cluster are also shown. The two kinds of catastrophes seen are characterized either by network split (Type A) or poor inter-filament connectivity (Type B).

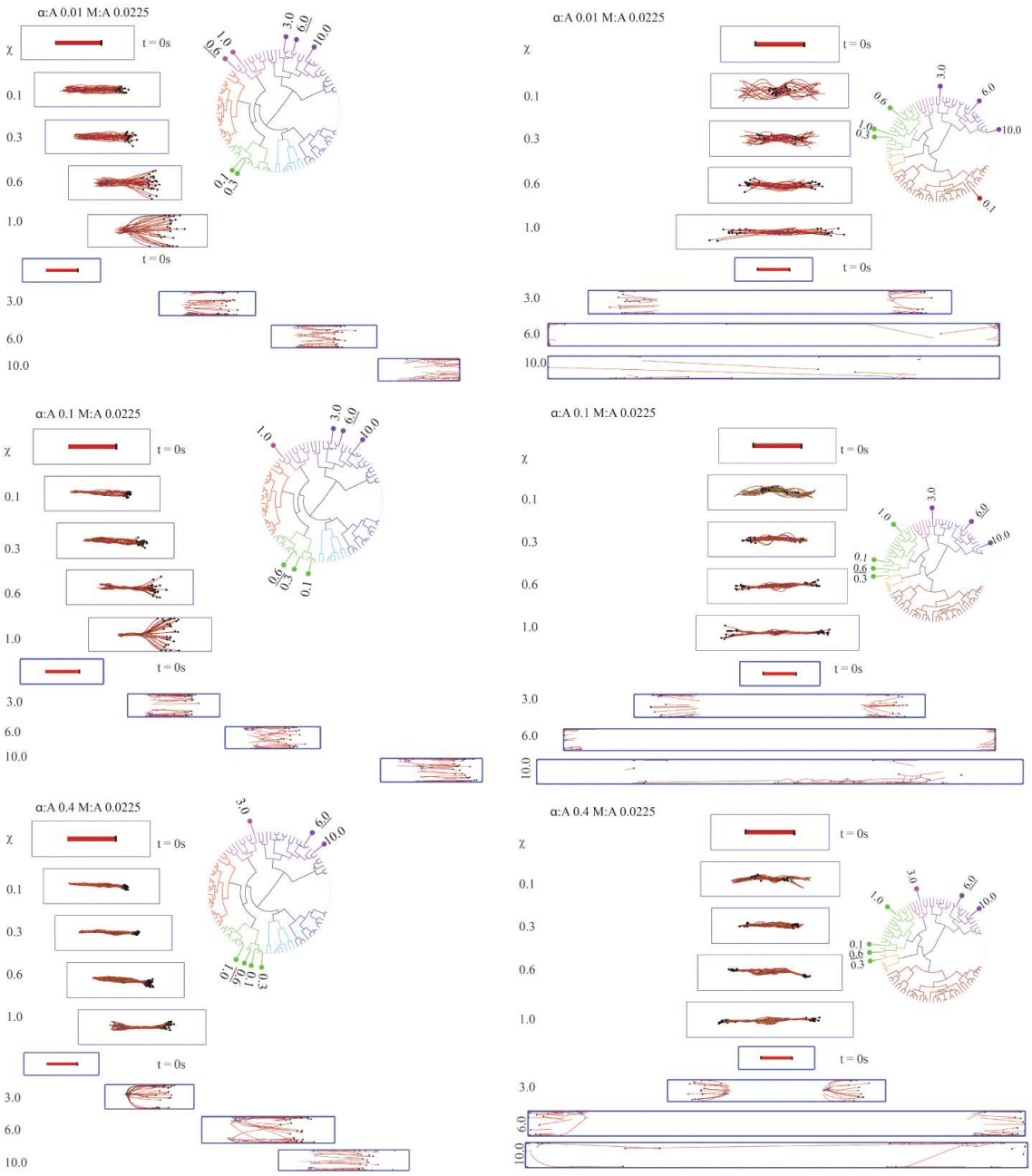

Figure A-6 Networks evolved from unipolar (left) and apolar (right) bundle configuration with M:A = 0.0225, at α:A 0.01 (top row), 0.1 (middle row), and 0.4 (bottom row) under different treadmilling rates modulated through χ. Side view of reaction volumes (blue rectangle) filled with actin filaments (red) along with bound myosin (blue) and α-actinin (green) are shown. Initial reaction volume side views along with initial actin network configuration are also shown for comparison. Inset in each panel shows a dendrogram obtained from the clustering protocol used. Refer to Appendix A, Figure A-4 for the color map of dendrograms presented.

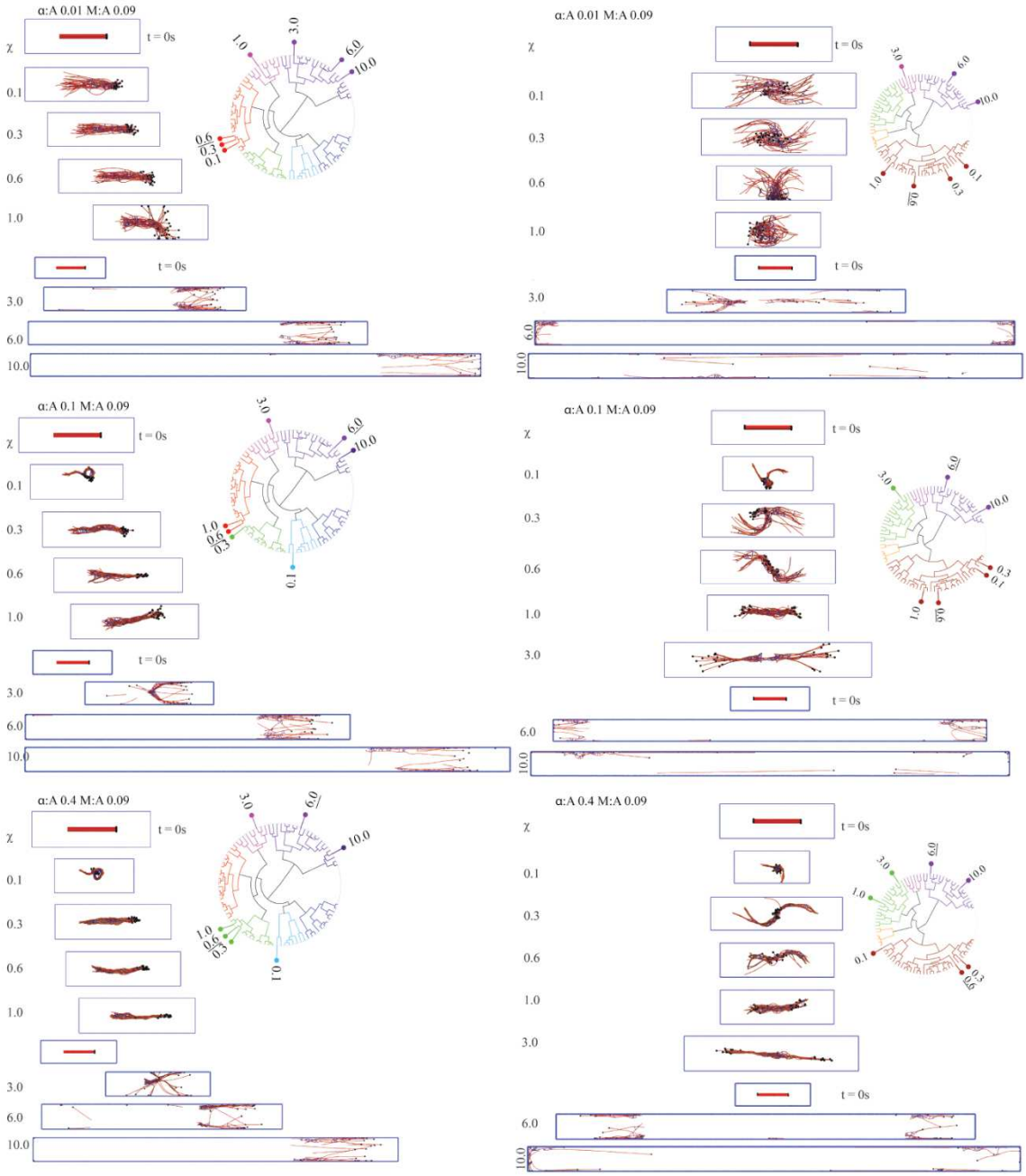

Figure A-7 Networks evolved from unipolar (left) and apolar (right) bundle configuration with M:A = 0.09, at α:A 0.01 (top row), 0.1 (middle row), and 0.4 (bottom row) under different treadmilling rates modulated through χ. Side view of reaction volumes (blue rectangle) filled with actin filaments (red) along with bound myosin (blue) and α-actinin (green) are shown. Initial reaction volume side views along with initial actin network configuration are also shown for comparison. Inset in each panel shows a dendrogram obtained from the clustering protocol used. Refer to Appendix A, Figure A-4 for the color map of dendrograms presented.

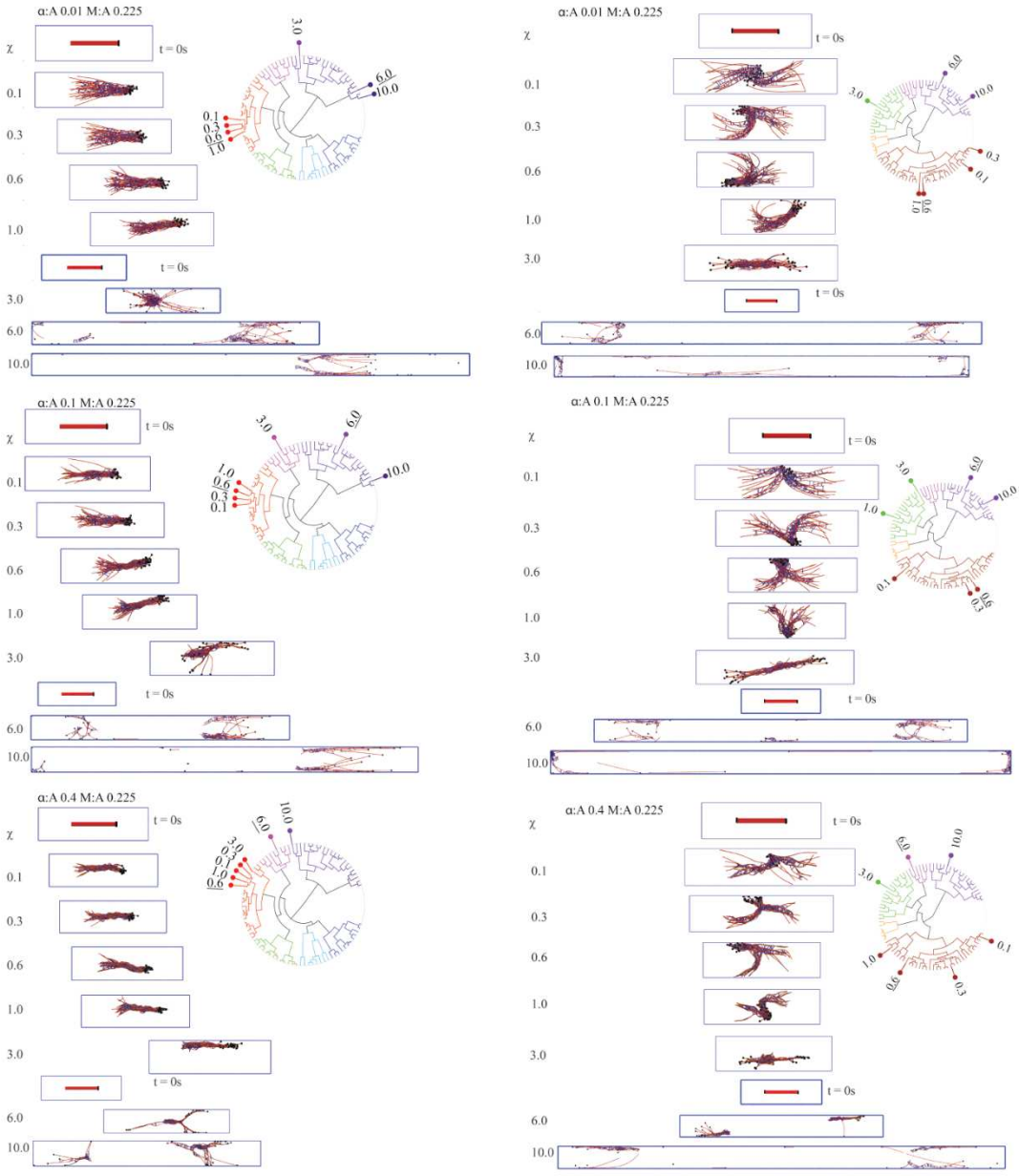

Figure A- 8 Networks evolved from unipolar (left) and apolar (right) bundle configuration with M:A = 0.0225, at α:A 0.01 (top row), 0.1 (middle row), and 0.4 (bottom row) under different treadmilling rates modulated through χ. Side view of reaction volumes (blue rectangle) filled with actin filaments (red) along with bound myosin (blue) and α-actinin (green) are shown. Initial reaction volume side views along with initial actin network configuration are also shown for comparison. Inset in each panel shows a dendrogram obtained from the clustering protocol used. Refer to Appendix A, Figure A-4 for the color map of dendrograms presented.

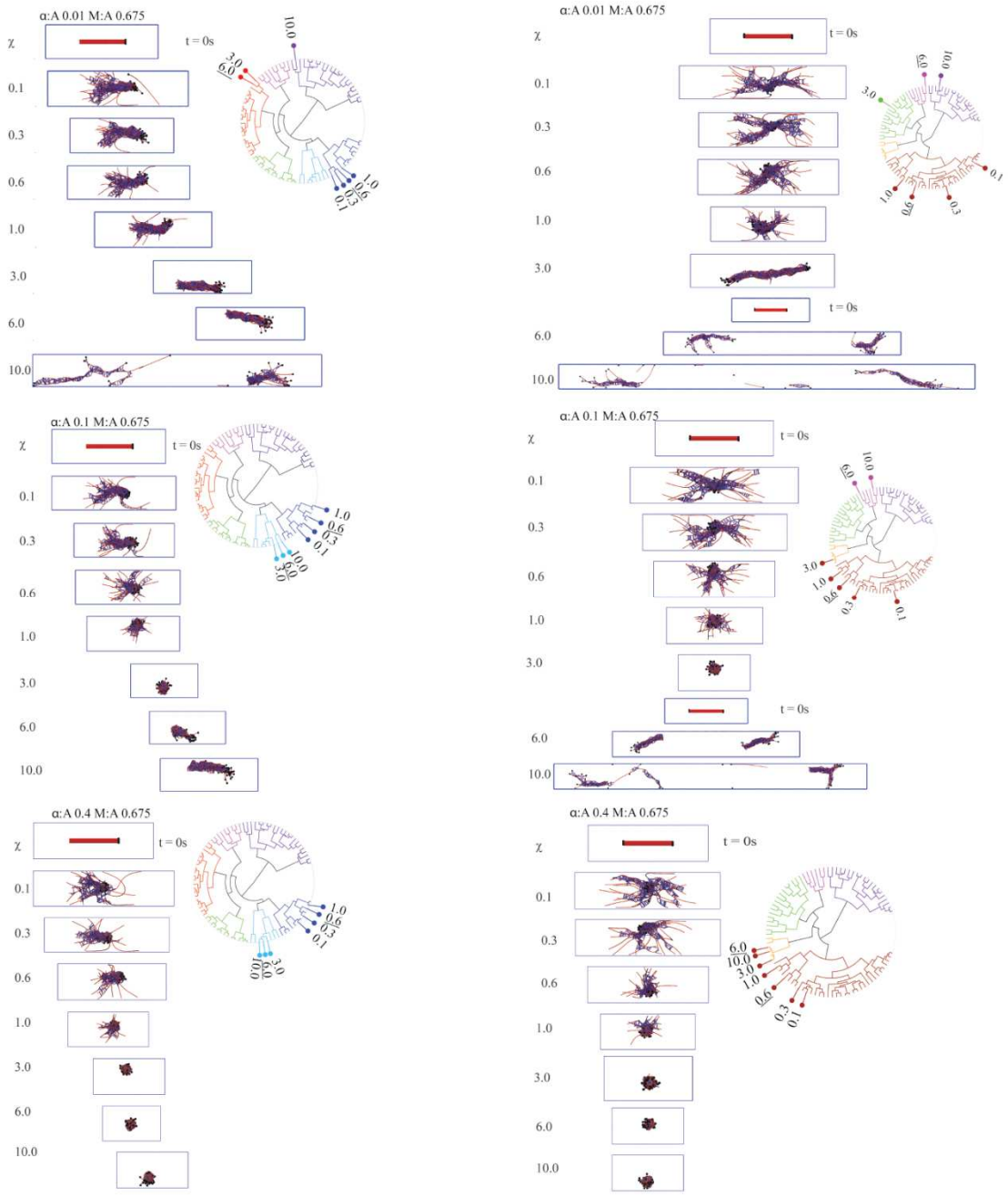

Figure A- 9 Networks evolved from unipolar (left) and apolar (right) bundle configuration with M:A = 0.675, at α:A 0.01 (top row), 0.1 (middle row), and 0.4 (bottom row) under different treadmilling rates modulated through χ. Side view of reaction volumes (blue rectangle) filled with actin filaments (red) along with bound myosin (blue) and α-actinin (green) are shown. Initial reaction volume side views along with initial actin network configuration are also shown for comparison. Inset in each panel shows a dendrogram obtained from the clustering protocol used. Refer to Appendix A, Figure A-4 for the color map of dendrograms presented.

Supplementary Results

A.1. Trajectory analysis

Trajectories were generated for each pair of crosslinker and myosin mole ratios considered (α: A, M: A) in the case of non-treadmilling study, and for each triad of treadmilling factor, crosslinker mole ratio and myosin mole ratio (χ, α: A, M: A) to study the effect of treadmilling under both unipolar and apolar initial conditions. Trajectories are analyzed once a steady-state is reached. Steady-state is defined based on network radius of gyration for non-treadmilling networks (Appendix A, Figure A-10) and based on filament length fluctuations for treadmilling networks (Appendix A, Figure A-11). Filament length fluctuations are characterized by filament treadmilling rate, defined as the rate of monomer addition at plus-end or removal at minus end of each filament in the network. To ensure equal sampling at steady-state across all conditions studied, the last 500s of the trajectories are considered for analyses.

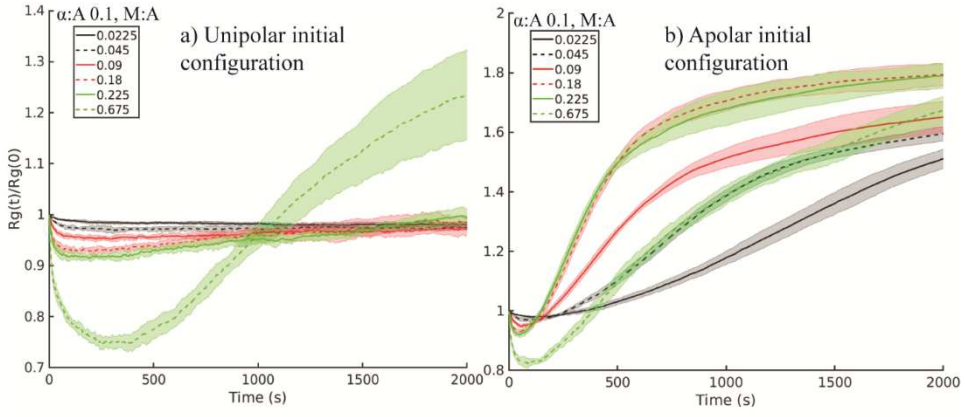

Figure A- 10 Ratio of network radius of gyration to initial radius of gyration at α:A 0.1 and various myosin mole ratios. The mean and standard deviation of Rg(t)/Rg(0) is plotted as a time series for trajectories from a) Unipolar b) initial Apolar configurations. Both unipolar

and apolar bundles at high myosin mole ratio (0.675) show higher fluctuation in Rg(t)/Rg(0) due to myosin activity.

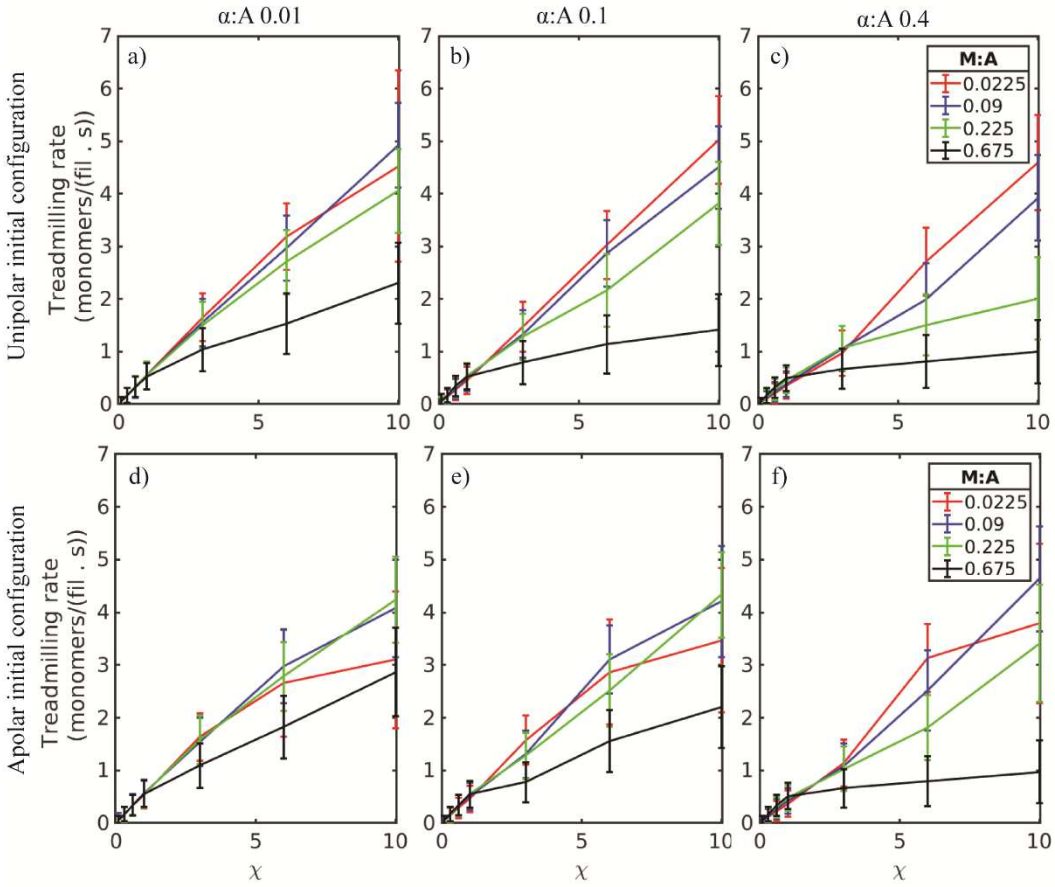

Figure A- 11 Treadmilling rates as a function of χ parameter. Mean and standard deviation of treadmilling rates of networks evolved from unipolar (a-c) and apolar (d-f) bundles as the initial configuration are shown. α-actinin mole ratios are mentioned on top of each panel at varying M: A. The last 500s of the trajectories were used to calculate treadmilling rates. Treadmilling rate is defined as the rate of monomer addition at the plus end (removal at the minus end) for each filament in the network.

Supplementary Methods

A.2. Chemical model

2.1. Diffusion

Rigorous consideration of the diffusion process would involve Brownian dynamics simulation of each of the freely diffusing molecules in the system. As this is computationally expensive, we divide the reaction volume into compartments of uniform mixing based on the Kuramoto length [242]. Kuramoto length is the length scale over which two regions of the reactive diffusion system are uncorrelated with respect to copy number fluctuations of diffusing molecules [243,244].

Kuramoto length measures the mean free path before reactive collisions. In other words, a chemical species diffusing in a volume undergo a reaction before it traverses Kuromoto length [245]. The species are mixed uniformly within spatial dimensions determined by Kuromoto length, while points separated by distances larger than Kuramoto length fluctuate independently [243,244]. Hence, the reaction volume is divided into compartments whose dimensions are smaller than Kuromoto's length. If the species of interest diffusing with a diffusion constant D is produced at the mesoscopic rate k+ and consumed at the rate k-, Kuramoto length is given by the ratio

$$K_l = \sqrt{\frac{k^+ k^-}{D}}$$

As actin polymerization is the fastest reaction in actomyosin networks, the cellular concentration of actin is used to determine Kuromoto length. We choose a compartment size of 500 nm, which is less than the Kuromoto length [89].

Diffusion reactions are defined as events of single-molecule transfer between two compartments. Hence, for two compartments (A and B) sharing a boundary, we define two different diffusion reactions (molecule from A diffuses into B and vice versa). Diffusion events are chemical reactions in the stochastic simulation protocol. Thus, diffusing molecules are represented as a homogenous continuum within compartments instead of individual particles. Diffusion coefficients of α-actinin and myosin were considered to be 1/4 and 1/8 that of actin, respectively.

2.2. α-actinin, myosin minifilament binding and unbinding

The rate constants for each of these reactions were obtained from experiments as explained in [89]. Any two unoccupied actin-binding sites within (4 per cylinder) α-actinin (30-40 nm)/minifilament (175-225 nm) binding distance can be occupied by a crosslinker/NMII-A minifilament, respectively. The binding sites are chosen at random from the set of all possible binding sites. NMIIA minifilaments are made of 15-30 myosin molecules [246], and the number of myosin heads is chosen at random within the specified range during each binding event. Refer to the section on Mechanical Model, Mechanichemical coupling for more details.

2.3. Minifilament walking

Minifilaments make use of energy from ATP hydrolysis and processively walk towards barbed ends of the actin network. We simulate minifilament walking based on zero load walking rates used in previous studies [62]. Mechanochemical coupling of walking rates is explained later.

A.3. Details of the mechanical model in MEDYAN

3.1. Actin filaments

In MEDYAN, actin filaments are modeled as cylinders with equilibrium spacing $l_0^m \ll l_p$ (l_0^m= 108 nm in this study, l_p-persistence length) connected in the ends. This aids considerable speed up during mechanical equilibration of the network compared to traditional bead and spring models. Axial stretching (U_i^{str}), bending at the hinges between consecutive cylinders (U_i^{bend}) excluded volume interactions between cylinders are the potentials included in the model.

The stretching and bending potentials are given by,

$$U_i^{str} = \frac{1}{2} K_{str} \left(\left| \vec{l_i} \right| - l_0 \right)^2 \tag{S3}$$

$$U_i^{bend} = \varepsilon_{bend} \left(1 - cos\left(\theta_{i,i+1} \right) \right) \tag{S4}$$

$K_{str}, \varepsilon_{bend}$ are stretching and bending constants, respectively. $\left| \vec{l_i} \right|$ is the length of cylinder *i* connecting beads at $\overrightarrow{x_i^1}$ and $\overrightarrow{x_i^2}$. $\theta_{i,i+1}$ measures the angle between cylinders *i* and *i+1*. Please refer to Figure 1-6 for an illustration of potentials used in the model.

In the case of excluded volume effects, we consider a potential equal to $\left|\vec{r_i} - \vec{r_j}\right|^4$ between any two fragments on cylinders *i* and *j* located at $\vec{r_i}$ and $\vec{r_j}$ respectively. Thus,

$$U_{ij}^{vol} = K_{vol} \int_{l_i} \int_{l_j} \frac{dl_i dl_j}{\left|\vec{r_i} - \vec{r_j}\right|^4} \tag{S5}$$

Where K_{vol} determines the strength of repulsion. This can be rewritten by considering $\vec{r_i} = \overrightarrow{x_i^1} + t\left(\overrightarrow{x_i^2} - \overrightarrow{x_i^1}\right)$, where $\underline{t}$ is a parameter.

$$U_{ij}^{vol} = K_{vol} \int_0^1 \int_0^1 \frac{dsdt}{\left|\vec{r_i} - \vec{r_j}\right|^4} \tag{S6}$$

This study considers four binding sites per cylinder available exclusively for the linker, motor binding.

3.2. α-actinin, minifilament model

As soon as a binding event is triggered, the actin-binding protein is represented physically as a spring connecting a pair of binding sites (on actin filament) subject to experimental constraints of bond length. During unbinding, the actin-bound protein is replaced in the reaction volume. Minifilaments consist of 15 to 30 heads, and a number is chosen at random during each binding step. Crosslinkers and minifilaments bound to points *i* and *j* on actin filament experience stretching potentials given by,

$$U_{ij}^{MF} = \frac{1}{2} K_{str}^{MF} \left(\left|\overrightarrow{l_{ij}}\right| - l_0\right)^2 \tag{S7}$$

$$U_{ij}^{linker} = \frac{1}{2} K_{str}^{linker} \left(\left|\overrightarrow{l_{ij}}\right| - l_0\right)^2 \tag{S8}$$

In the case of minifilaments (MF), $\overrightarrow{l_{ij}}$ changes with motor walking. It is rewritten in terms of the fractional position of the two MF heads on the actin cylinder.

3.3. Boundary

Boundaries in MEDYAN repel cylinders to confine the network within a certain volume. The repulsion energy $\varepsilon_{boundary}$ scales exponentially with characteristic length λ.

$$U_i^{boundary} = \varepsilon_{boundary} e^{-d/\lambda} \tag{S9}$$

A.4. Mechanochemical coupling

MEDYAN framework allows for explicit consideration of feedbacks from mechanics to the rates of chemical events. Anisotropy in the actin network leads to spatial differences in loads acting on actin, minifilaments, and α-actinin molecules. This highlights the necessity of mechanochemical coupling as experimental evidence suggests that the dynamics of minifilaments in regions of high stress I altered based on the catch-slip model. At the same time, the kinetics of α-actinin molecules are best represented by a slip model.

4.1. Minifilament walking, binding, and unbinding rates

The salient features of minifilaments of non-processive myosin II protein are well explained by the parallel cluster model (PCM) [62]. Ideas of mechanochemical feedback are borrowed primarily from this model. We consider a two-state system for minifilaments, namely bound and unbound. Bound state configuration is characterized by AM.ADP (Actin bound myosin with ADP ligand) while unbound state involves

M.ADP.Pi (freely diffusing minifilament liganded to ADP and Pi). Binding, unbinding, and walking rates are affected by mechanochemical feedback.

The filament binding rate k_b of minifilament can be written as,

$$k_{fil,bind} = k_{NMIIA,bind} \cdot N_{total} \tag{S10}$$

where $k_{NMIIA,bind}$is the binding rate for a single myosin head. N_{total} is picked at random at every binding event within the minimum and the maximum number of heads specified.

When subject to an external load (F_{ext}), the unbinding and walking rates are affected based on the number of heads in the bound state (N_{bound}). Under zero load conditions ($F_{ext} = 0$), N_{bound} is given by $N_0 = \rho N_{total}$. ρ=0.1 [251] is duty ratio defined as the fraction of time a myosin head stays in the strongly bound state. Under non -zero F_{ext}, we assume linear scaling of N_{bound} with parameter γ=0.05.

$$N_{bound} = N_0 + \gamma F_{ext} \tag{S11}$$

We use a catch bond behavior similar to that of [252] as the forces in our system are within the slip bond threshold [89].

$$k_{fil,unbind} = \frac{\epsilon \cdot k^0_{NMIIA,unbind}}{N_{bound}} \cdot exp\left(\frac{-F_{ext}}{N_{bound} \cdot F_{NMIIA,unbind}}\right) \tag{S12}$$

where $F_{NMIIA,unbind}$ is the characteristic unbinding force of each myosin head. ϵ is chosen to be 0.2 /pN. Under zero load conditions, walking rates are of each minifilament (not for individual heads) is related to single myosin head binding rate as,

$$k^0_{walk} = k_{NMII,bind}(N_{total} - N^0_{bound})/N^0_{bound} \tag{S13}$$

To model changes to myosin walking rate from mechanical forces, we employ a Hill [253] type force-velocity relation with a parameter ζ=0.1 [62].

$$k_{walk} = k_{walk}^{0} \cdot \frac{(F_{stall} - \mathrm{F_{ext}})}{(F_{stall} + F_{ext}/\zeta)} \quad \text{(S14)}$$

where $F_{stall} = 12.6pN$ is the minifilament stall force, and $\zeta = 0.1$.

4.2. α-actinin unbinding rate

Experimental evidence suggests that the α-actinin binding rate is unaffected by external load while the unbinding rate depends on slip bond behavior.

$$k_{\alpha,unbind} = k_{\alpha,unbind}^{0} \cdot exp\left(\frac{F_{ext}}{F_{\alpha,unbind}}\right) \quad \text{(S15)}$$

A.5. Clustering analysis

We devise a clustering algorithm to understand underlying network morphologies resulting from varying α-actinin and myosin minifilament mole ratios under unipolar and apolar initial conditions.

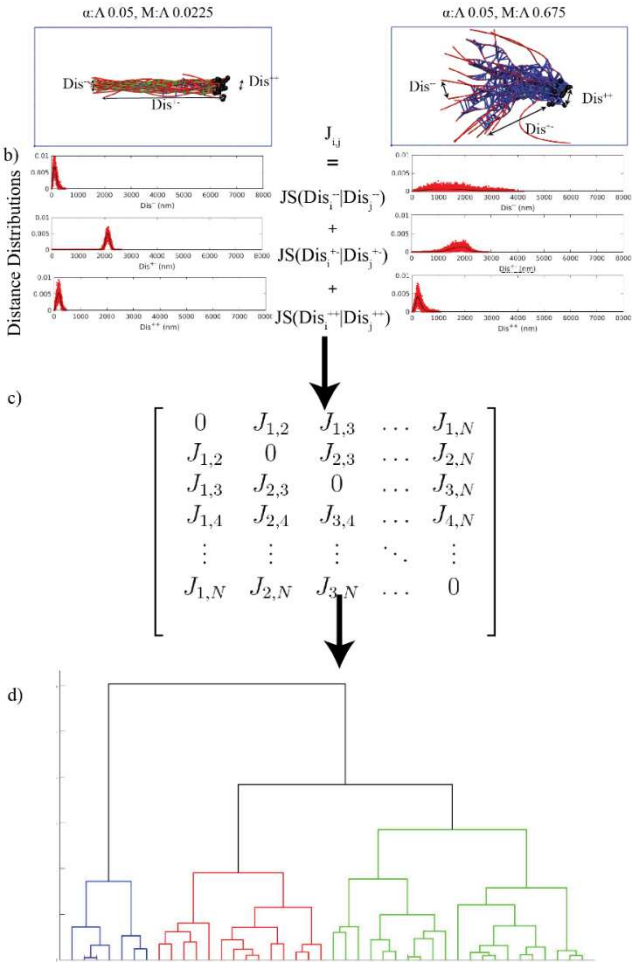

Figure A- 12 Schematic of clustering algorithm used to classify networks of unipolar networks under varying α:A and M: A values. Representative final snapshots from simulations under two different M: A values, namely 0.0225 (left) and 0.675 (right) at α:A 0.01, are shown. b) Three pair-wise distance distributions corresponding to Dis++, Dis—, and Dis+- are constructed. Jensen Shannon divergences of Dis++, Dis— and Dis+- are calculated for each unique simulation condition (determined by α:A and M: A) taken pairwise c) The sum of divergences is used to construct two dissimilarity matrices corresponding to unipolar and apolar initial conditions. d) Complete-linkage clustering algorithm is employed to construct an agglomerative, hierarchical linkage that can be visualized as dendrograms.

Distances between plus ends (Dis^{++}), minus ends (Dis^{--}), and minus-plus ends (Dis^{+-}) from the last 500s of each unique simulation condition are converted to distributions (Appendix A, Figure A-12b). To compute dissimilarity between each pair of conditions

(for example, α:A 0.05, M: A 0.0225 vs. α:A 0.05, M: A 0.675), the Jensen Shannon divergence [156] measure for each of the three distributions is added to produce a dissimilarity matrix (Appendix A, Figure A-12c). Jensen Shannon divergence between two continuous distributions P and Q is given by,

$$JSD(P||Q) = \frac{1}{2}D(P||M) + \frac{1}{2}D(Q||M) \quad \text{(A1)}$$

Where M=(P+Q)/2 and D() refers to Kullback-Leibler divergence defined as,

$$D_{KL}(P||Q) = \int_{-\infty}^{\infty} p(x) log\left(\frac{p(x)}{q(x)}\right) \quad \text{(A2)}$$

where p and q are probability densities of P and Q.

Hierarchical agglomerative clustering (complete-linkage clustering) is employed to convert this matrix to a dendrogram (Appendix A, Figure A-12d). The clades in the dendrograms correspond to different clusters present in our sample space. Conditions within each cluster result in similar network morphology compared to conditions outside. A similar procedure is repeated for results from varying χ-parameter to understand the relevant network morphologies.

A.6. Orientational order parameter (S)

S measures the directional order in liquid crystals to measure the structure of actin bundles obtained from MEDYAN simulations. The order parameter (S) is obtained from ordering tensor Q defined as,

$$Q_{\alpha\beta} = \frac{3}{2}\left(\frac{1}{N}\sum_{i=0}^{N} u_{i\alpha}u_{i\beta} - \frac{1}{3}\delta_{\alpha\beta}\right), \alpha, \beta = x, y, z \quad \text{(A3)}$$

The largest eigenvalue obtained from matrix Q represents the order parameter of the snapshot. Order parameter from snapshots after t=1000s was averaged over 15

trajectories to obtain $\langle S \rangle$. Order parameter 0 corresponds to random network while 1 represents absolute alignment.

A.7. Shape Parameter (Sh)

Sh measures the ratio of variance in the distribution of actin along the primary axis as a function of the sum of variances along all three principal axes. A matrix R matrix of bead coordinates is defined as,

$$\boldsymbol{R}^T = \begin{bmatrix} x_1 - \bar{x} & x_2 - \bar{x} & \dots x_N - \bar{x} \\ y_1 - \bar{y} & y_2 - \bar{y} & \dots y_N - \bar{y} \\ z_1 - \bar{z} & z_2 - \bar{z} & \dots z_N - \bar{z} \end{bmatrix} \quad \text{(A4)}$$

Eigen decomposition of R^TR gives eigenvalues $\lambda_1 \geq \lambda_2 \geq \lambda_3$ that correspond to variance along the three principal axes. Shape parameter is defined as, $Sh = \lambda_1/(\sum \lambda_i)$.

A.8. Probability distribution of linker, motor

For the cases where bundle configuration is preserved, the bundle axis can be approximated by the principal axis given by the eigenvector corresponding to the largest eigenvector of Eq. 11. Projections of position vectors of myosin minifilaments (α-actinin) from the center of mass of bundle give the position of minifilament (α-actinin) along the principal bundle axis. Coordinates of two binding sites and center of mass of minifilament (α-actinin) were considered. A probability density profile is obtained from binning results last 500s snapshots from all trajectories.

A.9. Protocol for flexible volume simulations

At the end of each mechanical equilibration phase, we find the compartments spanned by F-actin. An additional 1-micron skin distance is added to the extremities to define the bounds along the x-axis for the new reaction volume. If the new reaction volume is larger than the old reaction volume, 50% of the diffusing species in the compartments that form the bounds of the old reaction volume is shared with the newly included compartments, as shown in Appendix A, Figure A-13. This is continued recursively till the compartment extremities of the new reaction volume are reached. On the other hand, if the new reaction volume is smaller, starting from the outside, all diffusing species are transferred inward along X-axis recursively to the bounds of the new reaction volume.

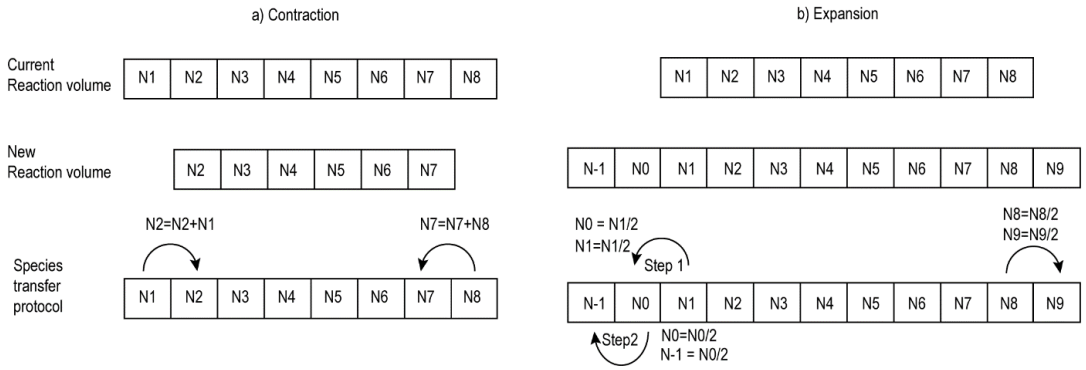

Figure A- 13 Schematic is explaining the flexible volume protocol employed to simulate treadmilling bundles. Reaction volume discretized into compartments is shown. Copy number of diffusing species (N) in the compartment (i) is represented as Ni. Scenarios where reaction volume has contracted (a) and expanded (b) at the end of chemical evolution, and mechanical equilibration are shown. Diffusing species are redistributed to account for the change in reaction volume. This protocol helps us explore filament dynamics without the influence of boundaries along the filament axis.

Appendix B. Supporting Information for Chapter 3

Supplementary Table

Parameter	Symbol	Value	Reference
Geometric parameters			
Compartment size	L_{comp}	500nm	[89]
Number of compartments in each dimension	Nx,Ny,Nz	4,4,15	-
Length of a cylinder	L_{cyl}	40	-
Minifilament binding distance	$d_{NMII,bind}$	175-225nm	[89]
α-actinin binding distance	$d_{\alpha,bind}$	30-40nm	[89]
Diffusion rates			
Actin	$k_{actin,diff}$	$20\mu m^2/s$ [80 s^{-1}]	[89]
α-actinin	$k_{\alpha,diff}$	$k_{actin,diff}/10$	[89]
Myosin minifilament	$k_{NMII,diff}$	$k_{actin,diff}/100$	[89]
Enabled	$k_{Ena,diff}$	$k_{actin,diff}/100$	-
Arp2/3	$k_{Arp,diff}$	$k_{actin,diff}/100$	-
Kinetic rate constants			
Actin polymerization at plus end	$k_{actin\ poly,+}$	11.6 $(\mu M.s)^{-1}$ [0.154s^{-1}]	[96]
Actin **de**polymerization at plus end	$k_{actin\ depoly,+}$	1.3 $(\mu M.s)^{-1}$ [0.017s^{-1}]	[96]
Actin polymerization at minus-end	$k_{actin\ poly,-}$	1.4 s^{-1}	[96]
Actin **de**polymerization at minus end	$k_{actin\ depoly,-}$	0.8 s^{-1}	[96]
α-actinin binding	$k_{\alpha,bind}$	0.7 $(\mu M.s)^{-1}$ [0.009 s^{-1}]	[254]
α-actinin unbinding (F=0pN)	$k_{\alpha,unbind}$	0.3 s^{-1}	[254]
NMII head binding	$k_{NMII,bind}$	0.2s^{-1}	[251]
NMII head unbinding (F=0pN)	$k_{NMII,unbind}$	1.0s^{-1}	**a**
Arp2/3 binding	$k_{Arp,bind}$	0.0017s^{-1}	**b**[205]
Arp2/3 unbinding (F=0pN)	$k_{Arp,unbind}$	0.02s^{-1}	**c**[205]
Mechanochemical constants			
NMII/α-actinin binding pitch on actin filament	-	27nm	[89]
NMII head step size	d_{step}	6.0nm	**d**[255][256]
NMII minifilament range of number of heads on each side of bipolar minifilament	N_{min}-N_{max}	15-30	**e**[257,258]

NMII minifilament stall force	$F_{NMII,stall}$	300pN for minifilament	**f**
NMII per head unbinding Force	$F_{NMII,\ unbind}$	12.62pN per head	[62]
Tunable parameters	β	0.2	[89]
	γ	$0.05pN^{-1}$	[89]
	ζ	0.1	[89]
Linker unbinding force	$F_{\alpha,\ unbind}$	17.2pN	[259]
Characteristic force of Brownian ratchet	$F_{ratchet}$	1.5pN	[260]
Mechanical constants			
Actin filament stretching constant	$K_{fil,str}$	100pN/nm	[89]
Actin filament bending energy	ε_{bend}	2690pN.nm	[89]
Cylinder-Cylinder Excluded volume constant	K_{vol}	10^5pN/nm	[89]
Myosin cross-bridge stiffness	$K_{NMII,str}$	2.5pN/nm	[256]
α-actinin stiffness	$K_{\alpha,str}$	8pN/nm	[261]
Boundary repulsion energy	$\varepsilon_{boundary}$	$10k_BT$	-
Boundary repulsion screening length	Λ	2.7nm	-
Minimization parameters			
Length of the chemical step	$\delta_{chemistry}$	25ms	-
Force tolerance for mechanical minimization	F_T	10pN	-

Table B- 1 Table of simulation parameters used in MEDYANv4.1 to simulate dendritic actin networks.

aObtained by assuming a duty ratio of 17%, which is the average of the 11% duty ratio corresponding to NMIIA and 23% duty ratio corresponding to NMIIB.[251]

bSlope of Figure 2D.

cBased on ATP actin parent filaments.

dValue chosen is close to the *Dictyostelium* step size of 7.3±0.4nm

e Experimental results suggest the total number of heads in NMIIA- 56[258], 58[257], NMIIB-60[257], and NMIIC-28[257]. Here, we use a wide range to account for multiple binding modes of myosin isoforms.

fConsidering the myosin-actin cross-bridge stiffness of k_{mhead} = 2.5pN/nm [256], the stall force of a single head F_{head} = $k_{mhead}xd_{step}$=15pN. If 15 heads are bound, the $F_{stall,15}$=225pN, while 30 bound heads result in $F_{stall,30}$=450pN. As our simulations dynamically choose myosin heads at binding, a stall force of about 300pN was chosen.

Supplementary Figures

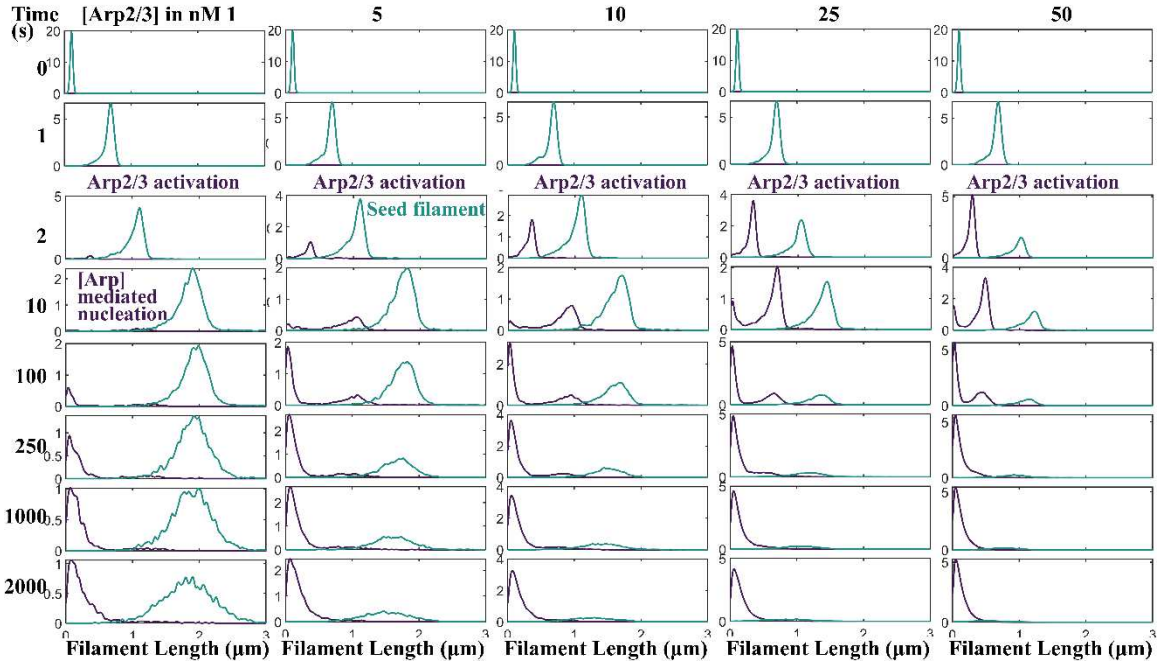

Figure B- 1 Arp2/3 nucleated filaments reach sub-micron length scales. Filament length distributions are shown at different time points (down each column) of the MEDYAN generated trajectories at various Arp2/3 concentrations (left to right in each row). Arp2/3 concentrations are mentioned on the top, while simulation time in seconds is mentioned to the left of the figure. Arp2/3 activation at 1s is also shown. At any given Arp2/3 concentration and time (in other words, in any given panel), the length distribution of seed filaments is shown in green, while length distributions of Arp2/3 nucleated filaments are shown in purple.

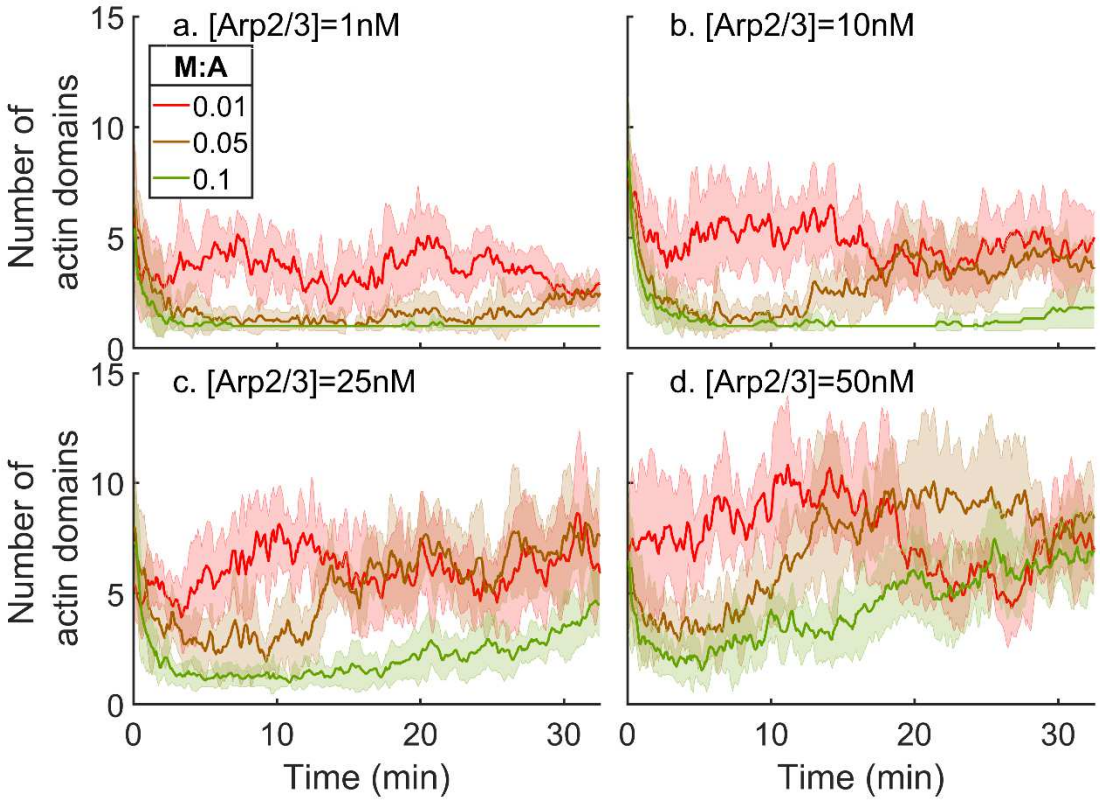

Figure B- 2 Influence of myosin in contractile dynamics of a dendritic network. a) Plot shows the number of domains in the actin density field obtained at a threshold concentration of 40μM at a) 1nM, b) 10nM, c) 25nM, and d) 50nM Arp2/3 concentration under three different myosin concentrations. Myosin mole ratios are mentioned in the legend. The solid line represents the mean, and the shaded area represents the standard deviation in the number of actin domains.

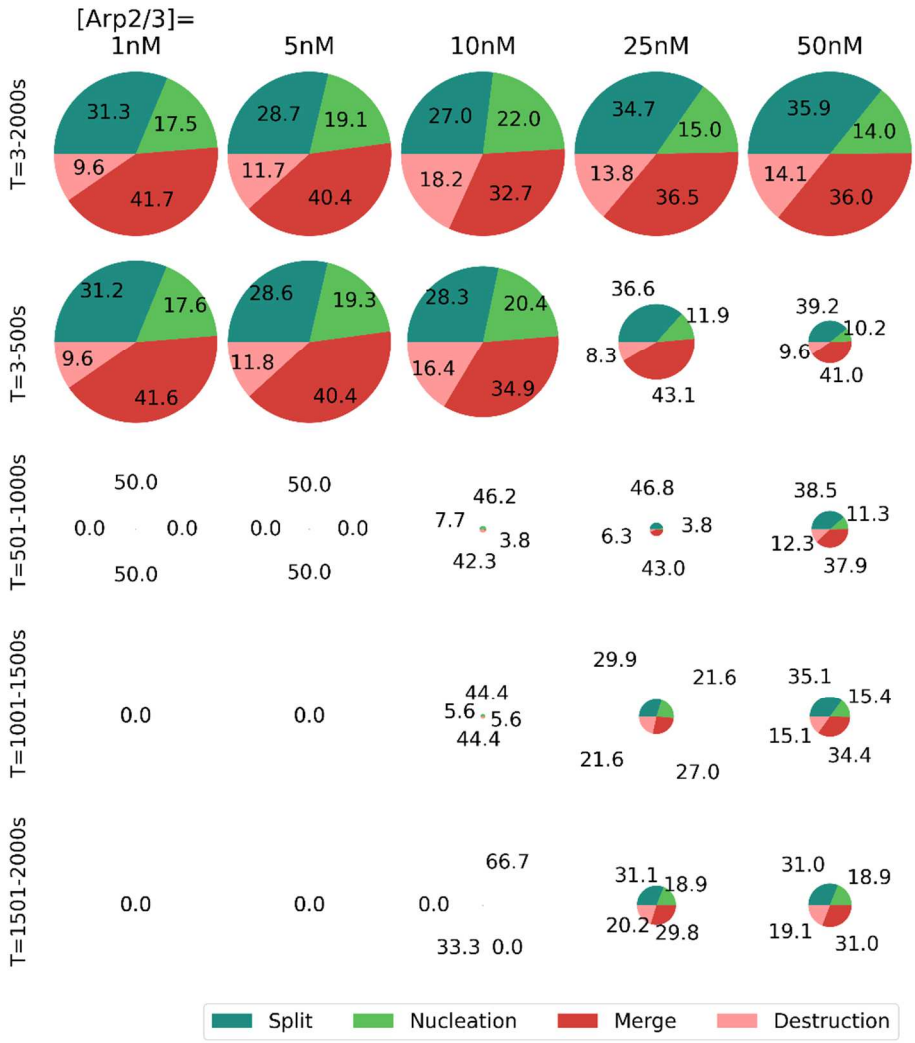

Figure B- 3 Distribution of different mechanisms that affect the number of high-density actin domains. Pie charts show the percentage of events that lead to birth or loss of domains. The Arp2/3 concentrations are mentioned on the top, while the time ranges over which the data was collected are mentioned to the left. Pie chart radii along each column are scaled to reflect the fraction of events during the entire trajectory (row 1). For example, under Arp2/3 concentrations of 1, 5, and 10nM, most of the birth/death events occur in the initial 500s of the trajectories.

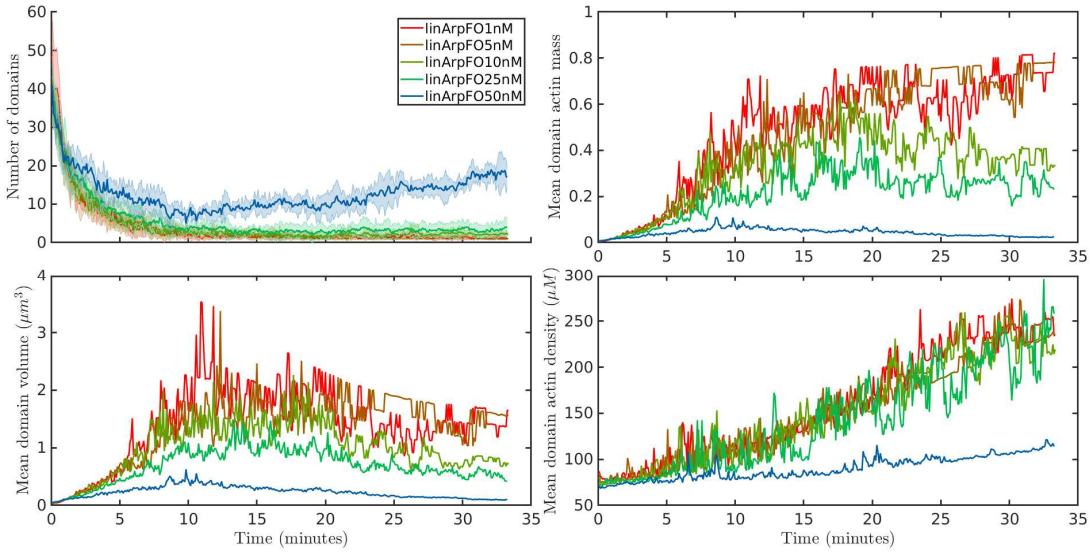

Figure B- 4 Linear nucleators with Arp2/3 kinetic parameters reproduces fragmentation patterns. Time profiles of number of domains, mean domain mass, mean domain volume, and mean actin density in domains are plotted. Solid lines in top left panel represent mean while shaded area represents standard deviation. Time profiles in all four panels are colored based on linear nucleators concentration shown in legend (top-left).

Supplementary Results

B.1. The dynamic evolution of actin domains is independent of threshold actin concentration

To ensure that the domain architecture observed in the actin density fields at 40μM threshold concentration is not limited by choice of threshold concentration, we also studied the actin dynamics at 20μM and 30μM thresholds (Figure B-4). We see that while the threshold concentration affects the number of high-density actin domains observed, it does not drastically alter the dynamics of actin domains. Thus, our observations reported in the main text are robust to the choice of F-actin concentration. It is worth noting that extremely high threshold concentrations will result in a different picture of actin organization (Figure 2.2B) but will be a misleading picture as it will include only a tiny fraction of total actin in the network (Figure 2.2C).

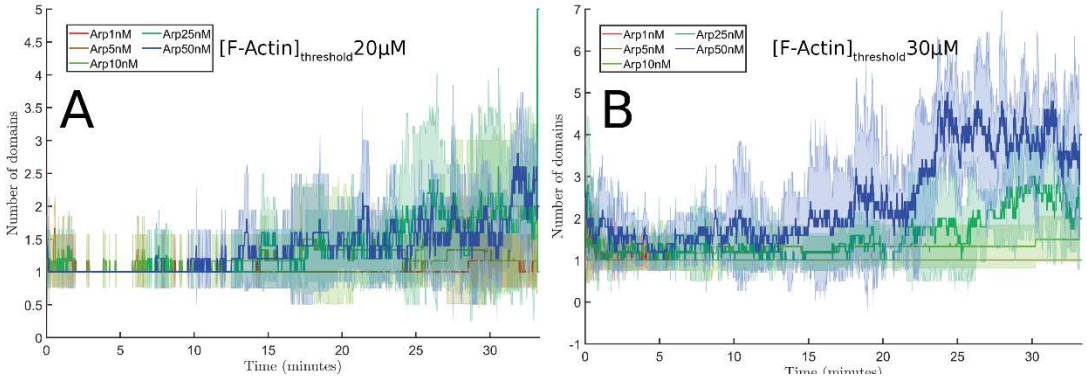

Figure B- 5. Arp2/3 dependant actin organization is independent of threshold concentration. The time profile of the number of high-density actin domains found by varying Arp2/3 concentration is shown. High-density domains were detected at A. 20 μM and 30 μM local actin concentration thresholds. The solid line and shaded area represent mean and standard deviation, respectively.

B.2. Estimation of drift and diffusion from domain count time-series data

To understand this, we modeled the time series of domain counts from the trajectories at high Arp2/3 concentrations as a stochastic Ito process given by,

$$dN = A(N,t)dt + B(N,t)dW \quad (1)$$

where the number of clusters at time t (N) depends on effective drift term (A) and diffusion coefficient (B). We estimated the effective drift and diffusive terms numerically as,

$$A(n,t) = \lim_{\Delta t \to 0} \frac{\langle N(t+\Delta t) - n \rangle}{\Delta t}\Big|_{N(t)=n} \quad (2)$$

$$B(n,t) = \lim_{\Delta t \to 0} \frac{\langle [N(t+\Delta t) - n]^2 \rangle}{\Delta t}\Big|_{N(t)=n} \quad (3)$$

Parameters A and B were estimated at different N(t) values for Δt=1s.

Appendix C. Supporting Information for Chapter 4

Supplementary Table

Parameter	Symbol	Value	Reference
Geometric parameters			
Compartment size	L_{comp}	500nm	[89]
Number of compartments in each dimension	Nx,Ny,Nz	4,4,15	-
Length of a cylinder	L_{cyl}	40	-
Minifilament binding distance	$d_{NMII,bind}$	175-225nm	[89]
α-actinin binding distance	$d_{\alpha,bind}$	30-40nm	[89]
Diffusion rates			
Actin	$k_{actin,diff}$	$20\mu m^2/s$ [80 s^{-1}]	[89]
α-actinin	$k_{\alpha,diff}$	$k_{actin,diff}/10$	[89]
Myosin minifilament	$k_{NMII,diff}$	$k_{actin,diff}/100$	[89]
Enabled	$k_{Ena,diff}$	$k_{actin,diff}/100$	-
Arp2/3	$k_{Arp,diff}$	$k_{actin,diff}/100$	-
Kinetic rate constants			
Actin polymerization at plus end	$k_{actin\ poly,+}$	11.6 $(\mu M.s)^{-1}$ [0.154s^{-1}]	[96]
Actin **de**polymerization at plus end	$k_{actin\ depoly,+}$	1.3 $(\mu M.s)^{-1}$ [0.017s^{-1}]	[96]
Actin polymerization at minus-end	$k_{actin\ poly,-}$	1.4 s^{-1}	[96]
Actin **de**polymerization at minus end	$k_{actin\ depoly,-}$	0.8 s^{-1}	[96]
α-actinin binding	$k_{\alpha,bind}$	0.7 $(\mu M.s)^{-1}$ [0.009 s^{-1}]	[254]
α-actinin unbinding (F=0pN)	$k_{\alpha,unbind}$	0.3 s^{-1}	[254]
NMII head binding	$k_{NMII,bind}$	0.2s^{-1}	[251]
NMII head unbinding (F=0pN)	$k_{NMII,unbind}$	1.0s^{-1}	**a**
Arp2/3 binding	$k_{Arp,bind}$	0.0017s^{-1}	**b**[205]
Arp2/3 unbinding (F=0pN)	$k_{Arp,unbind}$	0.02s^{-1}	**c**[205]
Ena binding	$k_{Ena,bind}$	75 $(\mu M.s)^{-1}$ [0.996s^{-1}]	[24]
Ena unbinding	$k_{Ena,unbind}$	0.69s^{-1}	[24]
Ena enhanced polymerization	$k_{Ena,poly}$	29.38 $(\mu M.s)^{-1}$ [0.39s^{-1}]	**d**
Mechanochemical constants			

NMII/α-actinin binding pitch on actin filament	-	27nm	[89]
NMII head step size	d_{step}	6.0nm	**e**[255][256]
NMII minifilament range of number of heads on each side of bipolar minifilament	N_{min}-N_{max}	15-30	**f**[257,258]
NMII minifilament stall force	$F_{NMII,stall}$	300pN for minifilament	**g**
NMII per head unbinding Force	$F_{NMII,\ unbind}$	12.62pN per head	[62]
Tunable parameters	β	0.2	[89]
	γ	$0.05pN^{-1}$	[89]
	ζ	0.1	[89]
Linker unbinding force	$F_{α,\ unbind}$	17.2pN	[259]
Characteristic force of Brownian ratchet	$F_{ratchet}$	1.5pN	[260]
Mechanical constants			
Actin filament stretching constant	$K_{fil,str}$	100pN/nm	[89]
Actin filament bending energy	$ε_{bend}$	2690pN.nm	[89]
Cylinder-Cylinder Excluded volume constant	K_{vol}	10^5pN/nm	[89]
Myosin cross-bridge stiffness	$K_{NMII,str}$	2.5pN/nm	[256]
α-actinin stiffness	$K_{α,str}$	8pN/nm	[261]
Boundary repulsion energy	$ε_{boundary}$	$10k_BT$	-
Boundary repulsion screening length	Λ	2.7nm	-
Minimization parameters			
Length of the chemical step	$δ_{chemistry}$	25ms	-
Force tolerance for mechanical minimization	F_T	10pN	-

Table C- 1 Table of simulation parameters used in MEDYANv4.1 to simulate dendritic actin networks.

aObtained by assuming a duty ratio of 17%, which is the average of the 11% duty ratio corresponding to NMIIA and 23% duty ratio corresponding to NMIIB.[251]

bSlope of Figure 2D.

cBased on ATP actin parent filaments.

d Refer Appendix C1

eValue chosen is close to the *Dictyostelium* step size of 7.3±0.4nm

f Experimental results suggest total number of heads in NMIIA- 56[258], 58[257], NMIIB-60[257], and NMIIC-28[257]. Here, we use a wide range to account for multiple binding modes of myosin isoforms.

gConsidering the myosin-actin cross-bridge stiffness of k_{mhead} = 2.5pN/nm [256], the stall force of a single head $F_{head} = k_{mhead} x d_{step}$=15pN. If 15 heads are bound, the $F_{stall,15}$=225pN, while 30 bound heads result in $F_{stall,30}$=450pN. As our simulations dynamically choose myosin heads at binding, a stall force of about 300pN was chosen.

Perturbation study paramters	Symbol	Value	Reference
Myosin walking driven perturbation of network			
Length of the chemical step	$\delta_{chemistry}$	10ms	-
Snapshot time step	$\Delta_{snapshot}$	100ms	-
Width of the active zone where myosin is activated	$d_{activezone}$	500nm	-
Functionalized AFM probe mimic simulations			
Number of compartments in each dimension	Nx,Ny,Nz	4,4,20	-
The time scale of the chemical step	$\delta_{chemistry}$	25ms	-
AFM tip motion at the end of the chemical cycle	d_{AFM}	5nm	[233]
Total number of AFM tip displacements	$N_{AFMsteps}$	100	-
Effective AFM tip velocity	v_{AFM}	200nm/s	-
AFM tip radius	R_{AFM}	250nm	[233]
Number of filaments attached to AFM tip	$N_{filaments,AFM}$	50	[233]
Length of filaments attached to AFM tip	$L_{filaments,AFM}$	540nm	-

Table C- 2 Table of additional simulation parameters used in MEDYANv4.1 to study responses of actin networks to perturbations.

Supplementary Figures

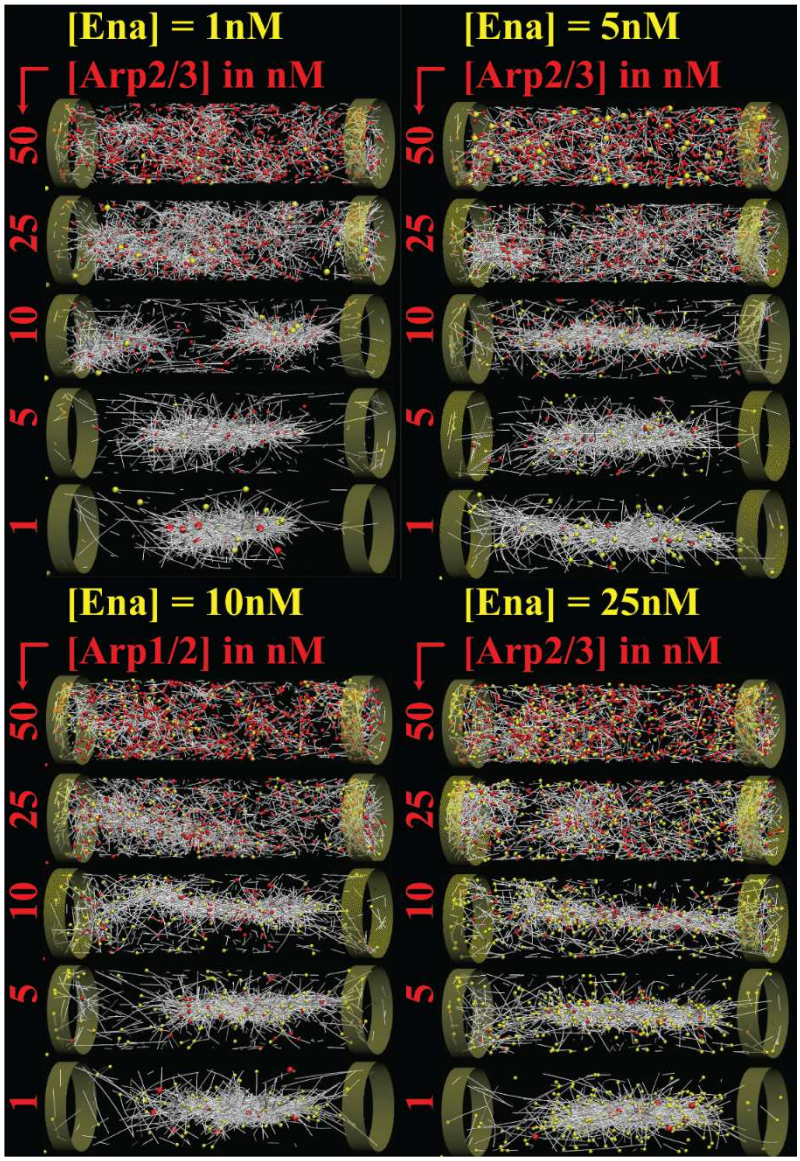

Figure C- 1 Representative final snapshots showing actin networks at various [Arp2/3] concentrations at [Ena]=1nM, 5nM, 10nM and 25nM. Actin filaments, Arp2/3, and Ena are shown as white filaments, red spheres, and yellow spheres, respectively.

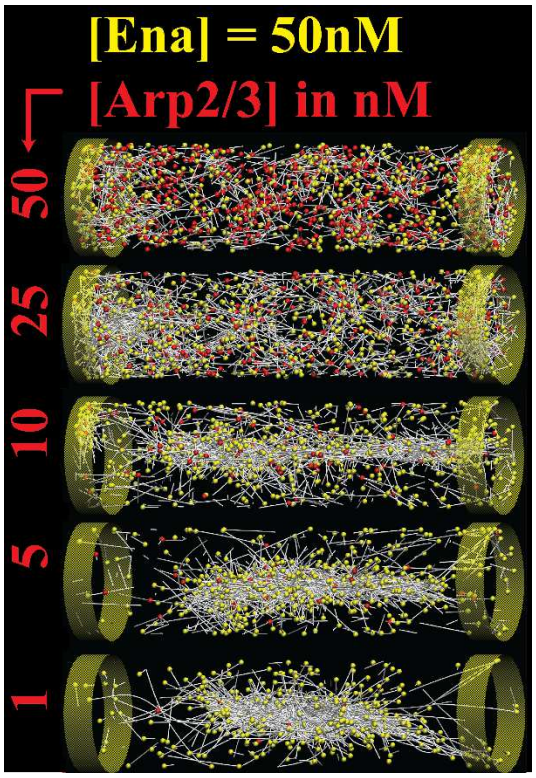

Figure C- 2 Representative final snapshots showing actin networks at various [Arp2/3] concentrations at [Ena]=50nM. Actin filaments, Arp2/3, and Ena are shown as white filaments, red spheres, and yellow spheres, respectively.

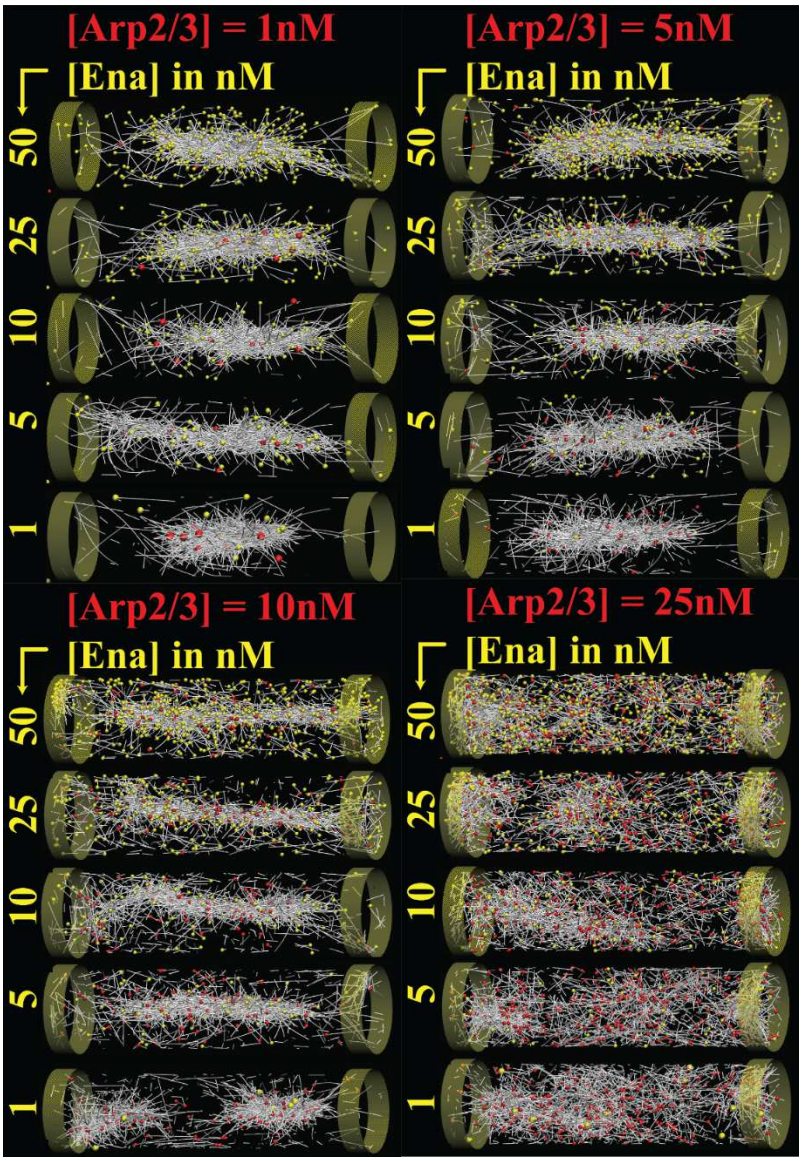

Figure C- 3 Representative final snapshots showing actin networks at various [Ena] concentrations at [Arp2/3]=1nM, 5nM, 10nM and 25nM. Actin filaments, Arp2/3, and Ena are shown as white filaments, red spheres, and yellow spheres, respectively.

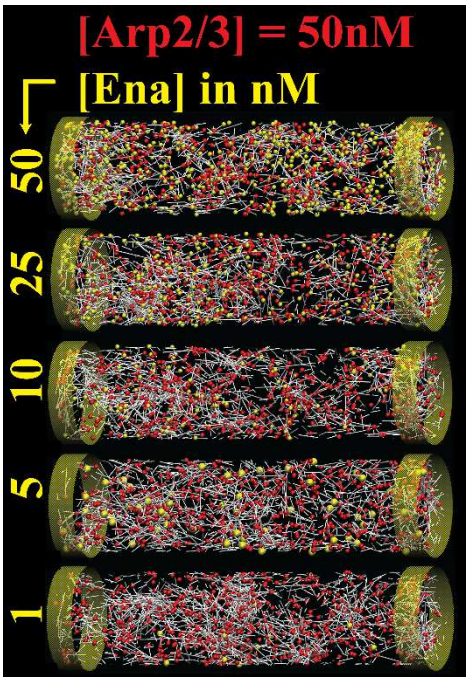

Figure C- 4 Representative final snapshots showing actin networks at various [Ena] concentrations at [Arp2/3]=50nM. Actin filaments, Arp2/3, and Ena are shown as white filaments, red spheres, and yellow spheres, respectively.

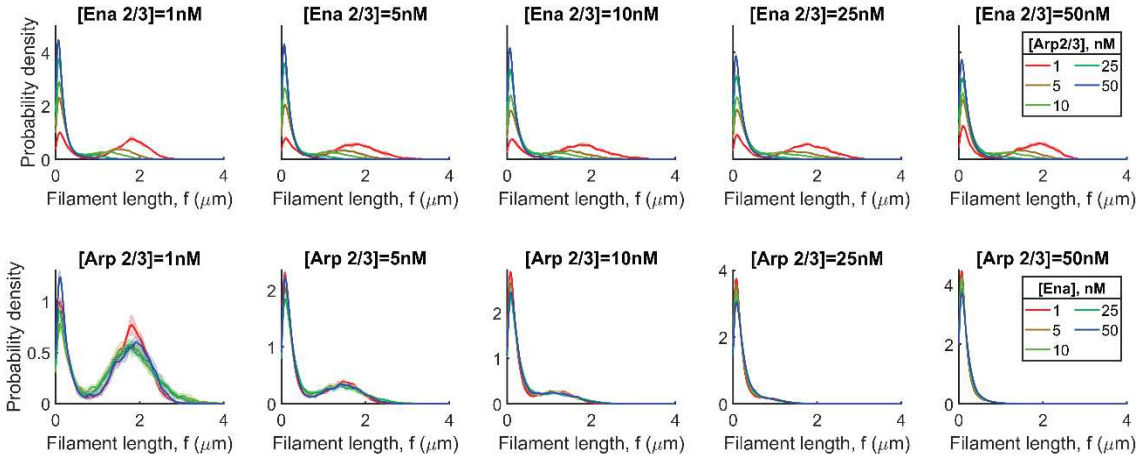

Figure C- 5 Effect of Arp2/3 and Ena on filament length distributions. Probability density function profiles of filament length distributions are shown by varying [Ena] concentration along the top row and by varying [Arp2/3] concentration along the bottom row. Each panel in the top row shows profiles from different Arp2/3 concentrations (shown in legend), while each panel in the bottom row shows profiles from varying Ena concentrations. Solid lines and shaded areas represent mean and standard deviation, respectively.

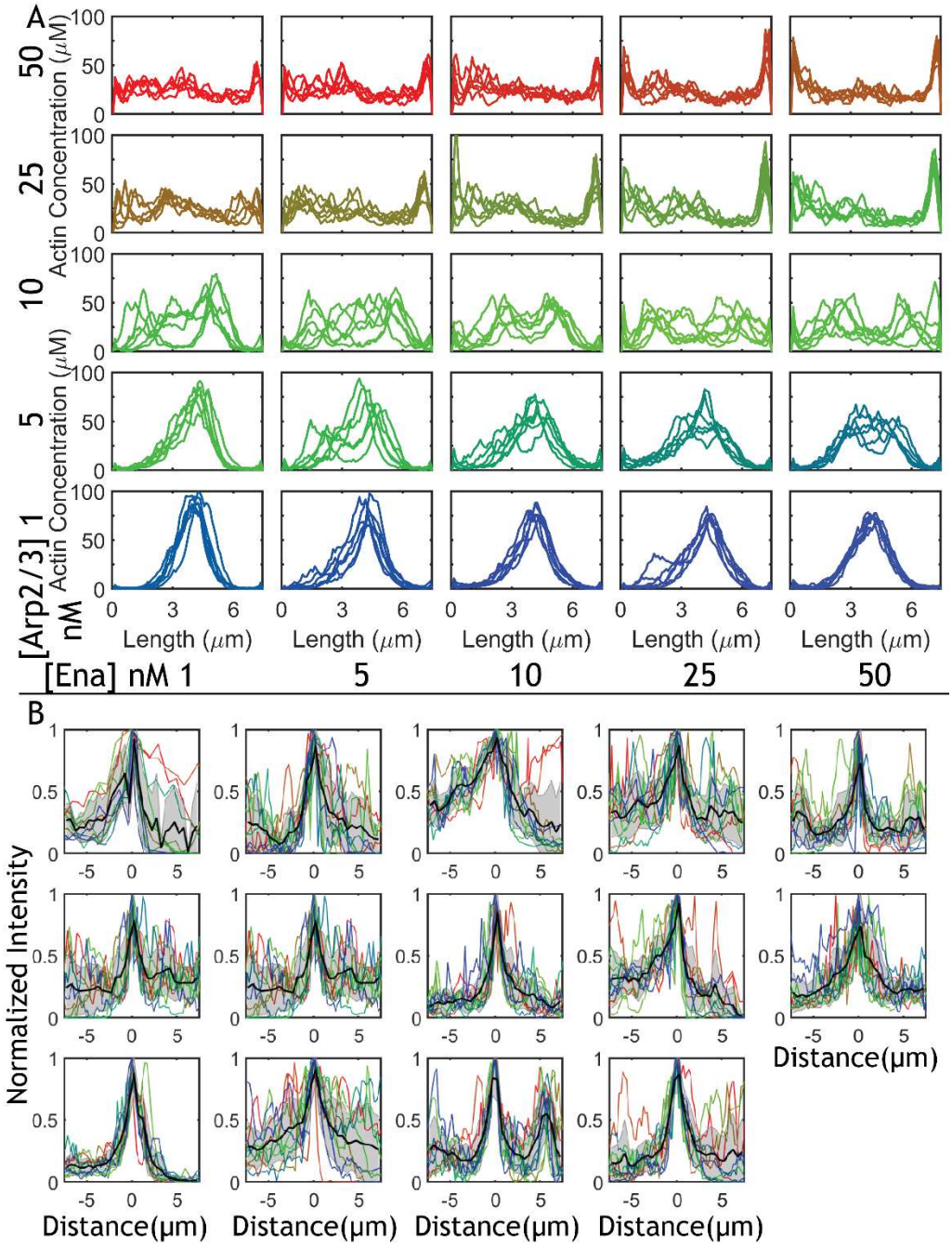

Figure C- 6 In-silico mimics of Abl share similar properties with *in vivo* growth cones. A. Axial actin distribution from the final snapshot of simulations is shown at various Arp/3 and Ena concentrations. Each panel shows actin peak-aligned actin profiles from 6 replicates. B. Peak-aligned, normalized actin intensity profiles from WT Abl axons is shown. The actin profiles are truncated based on an experimentally determined average growth cone span of 15μm. Each panel shows actin profiles from the first 30 minutes of imaging (sampling

frequency=3min) as solid lines. In all 14 cells imaged, the median and median absolute deviation of the actin intensity profiles are shown as solid black lines and shaded areas.

Supplementary Methods

C.1. Determination of Enabled-enhanced polymerization rate

In our simulations, we model Enabled as a molecule that can bind free barbed ends to stabilize them from depolymerization. Additionally, Ena also enhances the polymerization rate of filaments. As Ena polymerization rates are not readily available, we used data from Winkelman et al.[23] to determine rate constants. Under 0.924μM actin, 5nM of Ena extends actin filaments at the rate of 27.1 subunits/(filament.s) in the first 150s. The filament extension rate ($\frac{dN_{EV}^{+}}{dt}$) of Ena bound filaments, can be written as,

$$\frac{dN_{EV}^{+}}{dt} = k_{EV,poly}^{+} C_A^o$$

Thus, the Ena driven elongation rate of barbed ends is given as, $k_{EV,poly}^{+} = 29.38 \mu M^{-1} s^{-1}$.

C.2. A deterministic model for actin filament dynamics in the presence of Arp2/3 and Ena

Please refer to Appendix Table C-1 for a list of notations used. The following table gives the concentration of species

Concentration of	**Symbol**
F-actin	[FA]
Minus End	[M]
Plus End	[P]

Filament bound Arp2/3	[B]
Ena bound plus end	[EP]
Diffusing Actin	[AD]
Diffusing Arp2/3	[BD]
Diffusing Ena	[ED]

Table C- 3 Table of concentrations used in the deterministic model of actin dynamics.

The following kinetic equations give the dynamics of actin under the presence of Arp2/3 and Ena.

$$\frac{d[FA]}{dt} = k_{Arp,bind}\frac{1}{n}[FA][AD][BD] + k_{poly,+}[AD][P] + k_{poly,-}[AD][M]$$
$$- k_{depoly,-}[AD][M] - k_{depoly,+}[P] - k_{depoly,-}[M]$$
$$+ k_{poly,Ena}[EP][AD]$$

$$\frac{d[AD]}{dt} = -\frac{d[FA]}{dt}$$

$$\frac{d[EP]}{dt} = k_{bind,Ena}[P][ED] - k_{unbind,Ena}[EP]$$

$$\frac{d[P]}{dt} = -\frac{d[EP]}{dt} + k_{Arp,bind}\frac{1}{n}[FA][AD][BD]$$

$$\frac{d[M]}{dt} = k_{Arp,unbind}[B]$$

$$\frac{d[B]}{dt} = k_{Arp,bind}\frac{1}{n}[FA][AD][BD] - k_{Arp,unbind}[B]$$

$$\frac{d[BD]}{dt} = -\frac{d[B]}{dt}$$

The equations were solved simultaneously in MATLAB® using the ode45 function to generate numerical profiles of average filament length and Ena-driven actin turnover.

C.3. Filament-Filament contacts based community detection using Louvain Modularity

Modularity metric, Qϵ[-1,1], measures how well a set of edge-weighted nodes are organized as communities.

$$Q = \frac{1}{2m}\sum_{i,j}\left[A_{ij} - \frac{k_i k_j}{2m}\right]\delta(c_i, c_j)$$

$A_{i,j}$ represents the edge weight between nodes i and j. k_i and k_j represent the sum of weights from all nodes that are connected to i and j, respectively. ci and cj represent communities that nodes i and j are assigned to. Finally, $m = \frac{1}{2}\sum A_{ij}$. Louvain modularity optimization algorithm was implemented in MATLAB®. It involves the following steps. MEDYAN code was edited to output the total number of linkers, motors, and branchers between any two filaments. The output was used to generate a graph structure with filaments as nodes and the total number of linker, motor, and brancher contacts as the edge weight.

Optimization procedure based on Blondel et al. [236] and involves two phases. A graph structure each actin filament (graph node) is assigned to its own community. Thus, we start with as many communities as there are nodes in the network. We initiate optimization moves by randomly picking a node i belonging to community c_i. We consider neighbors {j} of node i and calculate the change in modularity when node i is assigned to each of the communities of neighbors {j}. Node i is placed in the community where the modularity gain is maximized. This procedure is repeated till no

more increase in modularity can be achieved. This marks the end of the first phase. Once completed, in the second phase, we use the community architecture at the optimal condition to generate a reduced Adjacency matrix which can be optimized further. In this graph structure, the communities from the previous iteration are defined as vertices of the graph. Edge weight between any two new vertices is defined as the sum of contacts between filaments that are part of the two communities. Connections within the same vertex lead to self-loops. By iteratively repeating phases one and two, we reduce the number of metacommunities detected. This procedure is repeated four times to understand the contact-based organization of actin filaments. Beyond four passes, we see negligible changes to the community organization of the networks studied.

Bibliography

1. Blanchoin L, Boujemaa-Paterski R, Sykes C, Plastino J. Actin dynamics, architecture, and mechanics in cell motility. Physiol Rev. 2014;94: 235–63. doi:10.1152/physrev.00018.2013
2. Gittes F, Mickey B, Nettleton J, Howard J. Flexural rigidity of microtubules and actin filaments measured from thermal fluctuations in shape. J Cell Biol. 1993;120: 923–934. doi:10.1083/jcb.120.4.923
3. Pollard TD. Actin and actin-binding proteins. Cold Spring Harb Perspect Biol. 2016;8: 1–18. doi:10.1101/cshperspect.a018226
4. Gunning PW, Ghoshdastider U, Whitaker S, Popp D, Robinson RC. The evolution of compositionally and functionally distinct actin filaments. J Cell Sci. 2015;128: 2009–2019. doi:10.1242/jcs.165563
5. Holmes KC, Popp D, Gebhard W, Kabsch W. Atomic model of the actin filament. Nature. 1990. pp. 44–49. doi:10.1038/347044a0
6. Oda T, Iwasa M, Aihara T, Maéda Y, Narita A. The nature of the globular- to fibrous-actin transition. Nature. 2009;457: 441–445. doi:10.1038/nature07685
7. Pollard TD, Blanchoin L, Mullins RD. Molecular mechanisms controlling actin filament dynamics in nonmuscle cells. Annu Rev Biophys Biomol Struct. 2000;29: 545–76. doi:10.1146/annurev.biophys.29.1.545
8. Wang X, Galletta BJ, Cooper JA, Carlsson AE. Actin-Regulator Feedback Interactions during Endocytosis. Biophys J. Biophysical Society; 2016;110:

1430–1443. doi:10.1016/j.bpj.2016.02.018

9. Konietzny A, Bär J, Mikhaylova M. Dendritic actin cytoskeleton: Structure, functions, and regulations. Front Cell Neurosci. 2017;11: 1–10. doi:10.3389/fncel.2017.00147

10. Pacheco A, Gallo G. Actin filament-microtubule interactions in axon initiation and branching. Brain Res Bull. Elsevier Inc.; 2016;126: 300–310. doi:10.1016/j.brainresbull.2016.07.013

11. Muller J, Oma Y, Vallar L, Friederich, Evelyne, Poch O, Winsor B. Sequence and Comparative Genomic Analysis of Actin-related Proteins. Mol Biol Cell. 2005;16: 5356–5372. doi:10.1091/mbc.E05

12. Rouiller I, Xu XP, Amann KJ, Egile C, Nickell S, Nicastro D, et al. The structural basis of actin filament branching by the Arp2/3 complex. J Cell Biol. 2008;180: 887–895. doi:10.1083/jcb.200709092

13. Espinoza-Sanchez S, Metskas LA, Chou SZ, Rhoades E, Pollard TD. Conformational changes in Arp2/3 complex induced by ATP, WASp-VCA, and actin filaments. Proc Natl Acad Sci U S A. 2018;115: E8642–E8651. doi:10.1073/pnas.1717594115

14. Tyler JJ, Allwood EG, Ayscough KR. WASP family proteins, more than Arp2/3 activators. Biochem Soc Trans. 2016;44: 1339–1345. doi:10.1042/BST20160176

15. Padrick SB, Rosen MK. Physical mechanisms of signal integration by WASP family proteins. Annu Rev Biochem. 2010;79: 707–735.

doi:10.1146/annurev.biochem.77.060407.135452

16. Pollard TD. Regulation of actin filament assembly by Arp2/3 complex and formins. Annu Rev Biophys Biomol Struct. 2007;36: 451–477. doi:10.1146/annurev.biophys.35.040405.101936

17. Goley ED, Welch MD. The ARP2/3 complex: An actin nucleator comes of age. Nat Rev Mol Cell Biol. 2006;7: 713–726. doi:10.1038/nrm2026

18. Dominguez R. Actin filament nucleation and elongation factors structure function relationships. Crit Rev Biochem Mol Biol. 2009;44: 351–366. doi:10.3109/10409230903277340

19. Qualmann B, Kessels MM. New players in actin polymerization - WH2-domain-containing actin nucleators. Trends Cell Biol. 2009;19: 276–285. doi:10.1016/j.tcb.2009.03.004

20. Quinlan ME, Heuser JE, Kerkhoff E, Mullins RD. Drosophila Spire is an actin nucleation factor. Nature. 2005;433: 382–388. doi:10.1038/nature03241

21. Conley CA, Fritz-Six KL, Almenar-Queralt A, Fowler VM. Leiomodins: Larger members of the tropomodulin (Tmod) gene family. Genomics. 2001;73: 127–139. doi:10.1006/geno.2000.6501

22. Fowler VM, Greenfield NJ, Moyer J. Tropomodulin contains two actin filament pointed end-capping domains. J Biol Chem. Â© 2003 ASBMB. Currently published by Elsevier Inc; originally published by American Society for Biochemistry and Molecular Biology.; 2003;278: 40000–40009. doi:10.1074/jbc.M306895200

23. Winkelman JD, Bilancia CG, Peifer M, Kovar DR. Ena/VASP Enabled is a highly processive actin polymerase tailored to self-assemble parallel-bundled F-actin networks with Fascin. Proc Natl Acad Sci. 2014;111: 4121–4126. doi:10.1073/pnas.1322093111

24. Hansen SD, Mullins RD. VASP is a processive actin polymerase that requires monomeric actin for barbed end association. J Cell Biol. 2010;191: 571–584. doi:10.1083/jcb.201003014

25. Pasic L, Kotova T, Schafer DA. Ena/VASP proteins capture actin filament barbed ends. J Biol Chem. 2008;283: 9814–9819. doi:10.1074/jbc.M710475200

26. Breitsprecher D, Kiesewetter AK, Linkner J, Vinzenz M, Stradal TEB, Small JV, et al. Molecular mechanism of Ena/VASP-mediated actin-filament elongation. EMBO J. Nature Publishing Group; 2011;30: 456–467. doi:10.1038/emboj.2010.348

27. Harker AJ, Katkar HH, Bidone TC, Aydin F, Voth GA, Applewhite DA, et al. Ena/VASP processive elongation is modulated by avidity on actin filaments bundled by the filopodia cross-linker fascin. Mol Biol Cell. 2019;30: 851–862. doi:10.1091/mbc.E18-08-0500

28. Ferron F, Rebowski G, Lee SH, Dominguez R. Structural basis for the recruitment of profilin-actin complexes during filament elongation by Ena/VASP. EMBO J. 2007;26: 4597–4606. doi:10.1038/sj.emboj.7601874

29. Barzik M, Kotova TI, Higgs HN, Hazelwood L, Hanein D, Gertler FB, et al.

Ena/VASP proteins enhance actin polymerization in the presence of barbed end capping proteins. J Biol Chem. 2005;280: 28653–28662. doi:10.1074/jbc.M503957200

30. Bear JE, Svitkina TM, Krause M, Schafer DA, Loureiro JJ, Strasser GA, et al. Antagonism between Ena/VASP proteins and actin filament capping regulates fibroblast motility. Cell. 2002;109: 509–521. doi:10.1016/S0092-8674(02)00731-6

31. Hu L, Papoian G a. How does the antagonism between capping and anti-capping proteins affect actin network dynamics? J Phys Condens Matter. 2011;23: 374101. doi:10.1088/0953-8984/23/37/374101

32. Rao JN, Madasu Y, Dominguez R. Mechanism of actin filament pointed-end capping by tropomodulin. Science (80-). 2014;345: 463–467. doi:10.1126/science.1256159

33. McCullough BR, Grintsevich EE, Chen CK, Kang H, Hutchison AL, Henn A, et al. Cofilin-linked changes in actin filament flexibility promote severing. Biophys J. Biophysical Society; 2011;101: 151–159. doi:10.1016/j.bpj.2011.05.049

34. Plastino J, Olivier S, Sykes C. Actin Filaments Align into Hollow Comets for Rapid VASP-Mediated Propulsion Julie. Curr Biol. 2004;14: ARTMED1118. doi:10.1016/j

35. Safer D, Elzinga M, Nachmias VT. Thymosin β4 and Fx, an actin-sequestering peptide, are indistinguishable. J Biol Chem. 1991;266: 4029–4032.

doi:10.1016/s0021-9258(20)64278-8

36. Carlier MF, Jean C, Rieger KJ, Lenfant M, Pantaloni D. Modulation of the interaction between G-actin and thymosin β4 by the ATP/ADP ratio: Possible implication in the regulation of actin dynamics. Proc Natl Acad Sci U S A. 1993;90: 5034–5038. doi:10.1073/pnas.90.11.5034

37. Kang F, Purich DL, Southwick FS. Profilin promotes barbed-end actin filament assembly without lowering the critical concentration. J Biol Chem. Â© 1999 ASBMB. Currently published by Elsevier Inc; originally published by American Society for Biochemistry and Molecular Biology.; 1999;274: 36963–36972. doi:10.1074/jbc.274.52.36963

38. Yarmola EG, Bubb MR. Effects of profilin and thymosin β4 on the critical concentration of actin demonstrated in vitro and in cell extracts with a novel direct assay. J Biol Chem. Â© 2004 ASBMB. Currently published by Elsevier Inc; originally published by American Society for Biochemistry and Molecular Biology.; 2004;279: 33519–33527. doi:10.1074/jbc.M404392200

39. Weber A, Pennise CR, Nachmias VT, Safer D, Pring M. Interaction of Thymosin β4 with Muscle and Platelet Actin : Implications for Actin Sequestration in Resting Platelets. Biochemistry. 1992;31: 6179–6185. doi:10.1021/bi00142a002

40. Yu FX, Lin SC, Morrison-Bogorad M, Atkinson MAL, Yin HL. Thymosin β10 and thymosin β4 are both actin monomer sequestering proteins. J Biol Chem. 1993;268: 502–509. doi:10.1016/S0021-9258(18)54179-X

41. Finkel T, Theriot JA, Dise KR, Tomaselli GF, Goldschmidt-Clermont PJ. Dynamic actin structures stabilized by profilin. Proc Natl Acad Sci U S A. 1994;91: 1510–1514. doi:10.1073/pnas.91.4.1510

42. Southwick FS, Young CL. The actin released from profilin - actin complexes is insufficient to account for the increase in F-actin in chemoattractant-stimulated polymorphonuclear leukocytes. J Cell Biol. 1990;110: 1965–1973. doi:10.1083/jcb.110.6.1965

43. Kinosian HJ, Selden LA, Gershman LC, Estes JE. Interdependence of profilin, cation, and nucleotide binding to vertebrate non-muscle actin. Biochemistry. 2000;39: 13176–13188. doi:10.1021/bi001520+

44. Xue B, Leyrat C, Grimes JM, Robinson RC. Structural basis of thymosin-β4/profilin exchange leading to actin filament polymerization. Proc Natl Acad Sci U S A. 2014;111: E4596–E4605. doi:10.1073/pnas.1412271111

45. Pring M, Weber A, Bubb MR. Profilin-Actin Complexes Directly Elongate Actin Filaments at the Barbed End. Biochemistry. 1992;31: 1827–1836. doi:10.1021/bi00121a035

46. Pernier, Julien, Shekhar S, Jegou A, Re GB renge`, Carlier M-F. Profilin Interaction with Actin Filament Barbed End Controls Dynamic Instability , Capping , Branching , Article Profilin Interaction with Actin Filament Barbed End Controls Dynamic. Dev Cell. 2016;36: 201–214. doi:10.1016/j.devcel.2015.12.024

47. Rotty JD, Wu C, Haynes EM, Suarez C, Winkelman JD, Johnson HE, et al.

Profilin-1 Serves as a gatekeeper for actin assembly by Arp2/3-Dependent and - Independent pathways. Dev Cell. Elsevier; 2015;32: 54–67. doi:10.1016/j.devcel.2014.10.026

48. Gau D, Ding Z, Baty C, Roy P. Fluorescence resonance energy transfer (FRET)-based detection of profilin-VASP interaction. Cell Mol Bioeng. 2011;4: 1–8. doi:10.1007/s12195-010-0133-z

49. Suarez C, Carroll RT, Burke TA, Christensen JR, Bestul AJ, Sees JA, et al. Profilin regulates F-Actin network homeostasis by favoring formin over Arp2/3 complex. Dev Cell. Elsevier Inc.; 2015;32: 43–53. doi:10.1016/j.devcel.2014.10.027

50. Romero S, Le Clainche C, Didry D, Egile C, Pantaloni D, Carlier MF. Formin is a processive motor that requires profilin to accelerate actin assembly and associated ATP hydrolysis. Cell. 2004;119: 419–429. doi:10.1016/j.cell.2004.09.039

51. Sanabria H, Swulius MT, Kolodziej SJ, Liu J, Waxham MN. βCaMKII regulates actin assembly and structure. J Biol Chem. 2009;284: 9770–9780. doi:10.1074/jbc.M809518200

52. Bugyi B, Carlier M-F. Control of actin filament treadmilling in cell motility. Annu Rev Biophys. 2010;39: 449–470. doi:10.1146/annurev-biophys-051309-103849

53. Kovar DR, Pollard TD. Insertional assembly of actin filament barbed ends in association with formins produces piconewton forces. Proc Natl Acad Sci.

2004;101: 14725–14730. doi:10.1073/pnas.0405902101

54. Svitkina T. The actin cytoskeleton and actin-based motility. Cold Spring Harb Perspect Biol. 2018;10: 1–22. doi:10.1101/cshperspect.a018267

55. Vignjevic D, Kojima SI, Aratyn Y, Danciu O, Svitkina T, Borisy GG. Role of fascin in filopodial protrusion. J Cell Biol. 2006;174: 863–875. doi:10.1083/jcb.200603013

56. Sjöblom B, Salmazo A, Djinović-Carugo K. α-Actinin structure and regulation. Cell Mol Life Sci. 2008;65: 2688–2701. doi:10.1007/s00018-008-8080-8

57. Pollard TD. Actin and Actin-Binding Proteins. Cold Spring Harb Perspect Biol. 2016;8: 1–18. doi:10.1101/cshperspect.a018226

58. Matsudaira P. Actin Crosslinking Proteins at the leading edge [Internet]. Seminars in cell biology. 1994. pp. 165–74. Available: http://www.ncbi.nlm.nih.gov/pubmed/7919230

59. Stricker J, Falzone T, Gardel ML. Mechanics of the F-actin cytoskeleton. J Biomech. Elsevier; 2010;43: 9–14. doi:10.1016/j.jbiomech.2009.09.003

60. De La Cruz EM, Ostap EM. Relating biochemistry and function in the myosin superfamily. Curr Opin Cell Biol. 2004;16: 61–67. doi:10.1016/j.ceb.2003.11.011

61. Sinard JH, Stafford WF, Pollard TD. The mechanism of assembly of Acanthamoeba myosin-II minifilaments: minifilaments assemble by three successive dimerization steps. J Cell Biol. 1989;109: 1537–47. doi:10.1083/jcb.109.4.1537

62. Erdmann T, Albert PJ, Schwarz US. Stochastic dynamics of small ensembles of non-processive molecular motors: The parallel cluster model. J Chem Phys. 2013;139. doi:10.1063/1.4827497

63. Kolega J. Cytoplasmic dynamics of myosin IIA and IIB: Spatial "sorting" of isoforms in locomoting cells. J Cell Sci. 1998;111: 2085–2095.

64. Mackintosh FC, Levine AJ. Nonequilibrium mechanics and dynamics of motor-activated gels. Phys Rev Lett. 2008;100: 1–4. doi:10.1103/PhysRevLett.100.018104

65. Mattila PK, Lappalainen P. Filopodia: Molecular architecture and cellular functions. Nat Rev Mol Cell Biol. 2008;9: 446–454. doi:10.1038/nrm2406

66. Svitkina TM, Bulanova EA, Chaga OY, Vignjevic DM, Kojima S ichiro, Vasiliev JM, et al. Mechanism of filopodia initiation by reorganization of a dendritic network. J Cell Biol. 2003;160: 409–421. doi:10.1083/jcb.200210174

67. Burridge K, Wittchen ES. The tension mounts: Stress fibers as force-generating mechanotransducers. Journal of Cell Biology. 2013. pp. 9–19. doi:10.1083/jcb.201210090

68. Tojkander S, Gateva G, Lappalainen P. Actin stress fibers - assembly, dynamics and biological roles. J Cell Sci. 2012;125: 1855–1864. doi:10.1242/jcs.098087

69. Hotulainen P, Lappalainen P. Stress fibers are generated by two distinct actin assembly mechanisms in motile cells. J Cell Biol. 2006;173: 383–394. doi:10.1083/jcb.200511093

70. Hu S, Dasbiswas K, Guo Z, Tee YH, Thiagarajan V, Hersen P, et al. Long-range self-organization of cytoskeletal myosin II filament stacks. Nat Cell Biol. 2017;19: 133–141. doi:10.1038/ncb3466

71. Pellegrin S, Mellor H. Actin stress fibres. J Cell Sci. 2007;120: 3491–3499. doi:10.1242/jcs.018473

72. Valerius NH, Stendahl O, Hartwig JH, Stossel TP. Distribution of actin-binding protein and myosin in polymorphonuclear leukocytes during locomotion and phagocytosis. Cell. 1981;24: 195–202. doi:10.1016/0092-8674(81)90515-8

73. Rubino S, Fighetti M, Unger E, Cappuccinelli P. Location of actin, myosin, and microtubular structures during directed locomotion of Dictyostelium amebae. J Cell Biol. 1984;98: 382–390. doi:10.1083/jcb.98.2.382

74. Svitkina TM, Borisy GG. Arp2/3 complex and actin depolymerizing factor/cofilin in dendritic organization and treadmilling of actin filament array in lamellipodia. J Cell Biol. 1999;145: 1009–1026. doi:10.1083/jcb.145.5.1009

75. Akin O, Mullins RD. Capping Protein Increases the Rate of Actin-Based Motility by Promoting Filament Nucleation by the Arp2/3 Complex. Cell. 2008;133: 841–851. doi:10.1016/j.cell.2008.04.011

76. Blair SS, Palka J. Axon guidance in cultured wing discs and disc fragments of Drosophila. Dev Biol. 1985;108: 411–419. doi:10.1016/0012-1606(85)90044-2

77. Murray MA, Schubiger M, Palka J. Neuron differentiation and axon growth in the developing wing of Drosophila melanogaster. Dev Biol. 1984;104: 259–

273. doi:10.1016/0012-1606(84)90082-4

78. Jan YN, Ghysen A, Christoph I, Barbel S, Jan LY. Formation of neuronal pathways in the imaginal discs of Drosophila melanogaster. J Neurosci. 1985;5: 2453–2464. doi:10.1523/jneurosci.05-09-02453.1985

79. Dent EW, Gertler FB. Cytoskeletal dynamics and transport in growth cone motility and guidance. Neuron. 2003;40: 209–227. doi:10.1016/S0896-6273(03)00633-0

80. Skoble J, Auerbuch V, Goley ED, Welch MD, Portnoy DA. Pivotal role of VASP in Arp2/3 complex-mediated actin nucleation, actin branch-formation, and Listeria monocytogenes motility. J Cell Biol. 2001;155: 89–100. doi:10.1083/jcb.200106061

81. Chesarone MA, Goode BL. Actin Nucleation and Elongation Factors: Mechanisms and Interplay. Cell. 2010;21: 28–37. doi:10.1016/j.ceb.2008.12.001.Actin

82. Chandrasekaran A, Upadhyaya A, Papoian GA. Remarkable structural transformations of actin bundles are driven by their initial polarity, motor activity, crosslinking, and filament treadmilling. PLoS Comput Biol. 2019;15: e1007156. doi:10.1371/journal.pcbi.1007156

83. Lan Y, Papoian G a. The stochastic dynamics of filopodial growth. Biophys J. 2008;94: 3839–3852. doi:10.1529/biophysj.107.123778

84. Zhuravlev PI, Papoian G a. Molecular noise of capping protein binding induces macroscopic instability in filopodial dynamics. Proc Natl Acad Sci U S A.

2009;106: 11570–11575. doi:10.1073/pnas.0812746106

85. Zhuravlev PI, Lan Y, Minakova MS, Papoian GA. Theory of active transport in filopodia and stereocilia. Proc Natl Acad Sci. 2012;109: 10849–10854. doi:10.1073/pnas.1200160109

86. Zhuravlev PI, Der BS, Papoian GA. Design of active transport must be highly intricate: A possible role of myosin and Ena/VASP for G-Actin transport in filopodia. Biophys J. Biophysical Society; 2010;98: 1439–1448. doi:10.1016/j.bpj.2009.12.4325

87. Zhuravlev PI, Papoian GA. Protein fluxes along the filopodium as a framework for understanding the growth-retraction dynamics. Cell Adh Migr. 2011;5: 448–456. doi:10.4161/cam.5.5.17868

88. Gibson MA, Bruck J. Efficient Exact Stochastic Simulation of Chemical Systems with Many Species and Many Channels. J Phys Chem A. 2000;104: 1876–1889. doi:10.1021/jp993732q

89. Popov K, Komianos J, Papoian GA. MEDYAN : Mechanochemical Simulations of Contraction and Polarity Alignment in Actomyosin Networks. PLoS Comput Biol. 2016;12: e1004877. doi:10.1371/journal.pcbi.1004877

90. Falzone TT, Blair S, Robertson-Anderson RM. Entangled F-actin displays a unique crossover to microscale nonlinearity dominated by entanglement segment dynamics. Soft Matter. Royal Society of Chemistry; 2015;11: 4418–4423. doi:10.1039/c5sm00155b

91. Rickman J, Nédélec F, Surrey T. Effects of spatial dimensionality and steric

interactions on microtubule-motor self-organization. Phys Biol. 2019;16: 046004. doi:10.1088/1478-3975/ab0fb1

92. Bun P, Dmitrieff S, Belmonte JM, Nédélec FJ, Lénárt P. A disassembly-driven mechanism explains F-actin-mediated chromosome transport in starfish oocytes. Elife. 2018;7: 1–27. doi:10.7554/elife.31469

93. Freedman SL, Banerjee S, Hocky GM, Dinner AR. A Versatile Framework for Simulating the Dynamic Mechanical Structure of Cytoskeletal Networks. Biophys J. Biophysical Society; 2017;113: 448–460. doi:10.1016/j.bpj.2017.06.003

94. Kim T. Determinants of contractile forces generated in disorganized actomyosin bundles. Biomech Model Mechanobiol. 2015;14: 345–355. doi:10.1007/s10237-014-0608-2

95. Kampen VNG. Stochastic Processes in Physics and Chemistry. Stochastic Processes in Physics and Chemistry. 2007. doi:10.1016/B978-0-444-52965-7.X5000-4

96. Fujiwara I, Vavylonis D, Pollard TD. Polymerization kinetics of ADP- and ADP-Pi-actin determined by fluorescence microscopy. Proc Natl Acad Sci. 2007;104: 8827–8832. doi:10.1073/pnas.0702510104

97. Peskin CS, Odell GM, Oster GF. Cellular motions and thermal fluctuations: the Brownian ratchet. Biophys J. 1993; doi:10.1016/S0006-3495(93)81035-X

98. Letort G, Politi A, Ennomani H, Thery M, Nedelec F, Blanchoin L. Geometrical and Mechanical Properties Control Actin Filament Organization.

Biophys J. 2014;106: 568a-569a. doi:10.1016/j.bpj.2013.11.3153

99. Floyd C, Jarzynski C, Papoian G. Low-dimensional manifold of actin polymerization dynamics. New J Phys. IOP Publishing; 2017;19. doi:10.1088/1367-2630/aa9641

100. Floyd C, Papoian GA, Jarzynski C. Quantifying Dissipation in Actomyosin Networks. Interface Focus. 2019;9: 201800781–10. doi:https://doi.org/10.1098/rsfs.2018.0078

101. Ott A, Magnasco M, Simon A, Libchaber A. Measurement of the persistence length of polymerized actin using fluorescence microscopy. Phys Rev E. 1993;48. doi:10.1103/PhysRevE.48.R1642

102. Nédélec F. Computer simulations reveal motor properties generating stable antiparallel microtubule interactions. J Cell Biol. 2002;158: 1005–1015. doi:10.1083/jcb.200202051

103. Skau CT, Waterman CM. Specification of Architecture and Function of Actin Structures by Actin Nucleation Factors. Annu Rev Biophys. 2015;44: 285–310. doi:10.1146/annurev-biophys-060414-034308

104. Sanger JW, Sanger JM, Jockusch BM. Differences in the stress fibers between fibroblasts and epithelial cells. J Cell Biol. 1983;96: 961–9. doi:10.1083/jcb.96.4.961

105. Livne A, Geiger B. The inner workings of stress fibers - from contractile machinery to focal adhesions and back. J Cell Sci. 2016;129: 1293–1304. doi:10.1242/jcs.180927

106. Hashimoto Y, Skacel M, Adams JC. Roles of fascin in human carcinoma motility and signaling: Prospects for a novel biomarker? Int J Biochem Cell Biol. 2005;37: 1787–1804. doi:10.1016/j.biocel.2005.05.004

107. Jacinto A, Wood W, Balayo T, Turmaine M, Martinez-Arias A, Martin P. Dynamic actin-based epithelial adhesion and cell matching during Drosophila dorsal closure. Curr Biol. 2000;10: 1420–1426. doi:10.1016/S0960-9822(00)00796-X

108. Applewhite, Derek A, Barzik, Melanie, Kojima, Shin-ichiro, Svitkina, Tatyana M, Gertler, Frank B, Borisy GG. Ena/VASP proteins have an anti-capping independent function in filopodia formation. Mol Biol Cell. 2007;18: 2579–2591. doi:10.1091/mbc.E06

109. Lewis GT, Hole W, Biology C, Republic F, Biology C, Tilney MS, et al. Preliminary biochemical characterization of the stereocilia and cuticular plate of hair cells of the chick cochlea. J Cell Biol. 1989;109: 1711–1723.

110. Hudspeth AJ, Jacobs R. Stereocilia mediate transduction in vertebrate hair cells (auditory system/cilium/vestibular system). Proc Natl Acad Sci. 1979;76: 1506–1509. doi:10.1073/pnas.76.3.1506

111. Narayanan P, Chatterton P, Ikeda A, Ikeda S, Corey DP, Ervasti JM, et al. Length regulation of mechanosensitive stereocilia depends on very slow actin dynamics and filament-severing proteins. Nat Commun. Nature Publishing Group; 2015;6: 1–8. doi:10.1038/ncomms7855

112. Croce A, Cassata G, Disanza A, Gagliani MC, Tacchetti C, Malabarba MG, et

al. A novel actin barbed-end-capping activity in EPS-8 regulates apical morphogenesis in intestinal cells of Caenorhabditis elegans. Nat Cell Biol. 2004;6: 1173–1179. doi:10.1038/ncb1198

113. Revenu C, Athman R, Robine S, Louvard D. The co-workers of actin filaments: from cell structures to signals. Nat Rev Mol Cell Biol. 2004;5: 635–646. doi:10.1038/nrm1437

114. Mseka T, Coughlin M, Cramer LP. Graded actin filament polarity is the organization of oriented actomyosin II filament bundles required for fibroblast polarization. Cell Motil Cytoskeleton. 2009;66: 743–753. doi:10.1002/cm.20403

115. Resolution H, Microscopy E, Meyer RK, Aebi U. Bundling of actin filaments by alpha-actinin depends on its molecular length. J Cell Biol. 1990;110: 2013–24. doi:10.1083/jcb.110.6.2013

116. Xu J, Wirtz D, Pollard TD. Dynamic cross-linking by α-actinin determines the mechanical properties of actin filament networks. J Biol Chem. 1998;273: 9570–9576. doi:10.1074/jbc.273.16.9570

117. Medeiros NA, Burnette DT, Forscher P. Myosin II functions in actin-bundle turnover in neuronal growth cones. Nat Cell Biol. 2006;8: 215–226. doi:10.1038/ncb1367

118. Friedrich BM, Fischer-Friedrich E, Gov NS, Safran SA. Sarcomeric pattern formation by actin cluster coalescence. PLoS Comput Biol. 2012;8: 1–10. doi:10.1371/journal.pcbi.1002544

119. Théry M, Pépin A, Dressaire E, Chen Y, Bornens M. Cell distribution of stress fibres in response to the geometry of the adhesive environment. Cell Motil Cytoskeleton. 2006;63: 341–355. doi:10.1002/cm.20126

120. Harker AJ, Katkar HH, Bidone TC, Aydin F, Voth GA, Applewhite DA, et al. Ena/VASP processive elongation is modulated by avidity on actin filaments bundled by the filopodia crosslinker fascin. Mol Biol Cell. 2019;30: mbc.E18-08-0500. doi:10.1091/mbc.e18-08-0500

121. Shimmen T, Yokota E. Cytoplasmic streaming in plants. Curr Opin Cell Biol. 2004;16: 68–72. doi:10.1016/j.ceb.2003.11.009

122. Yokota E, Vidali L, Tominaga M, Tahara H, Orii H, Morizane Y, et al. Plant 115-kDa Actin-Filament Bundling Protein, P-115-ABP, is a Homologue of Plant Villin and is Widely Distributed in Cells. Plant Cell Physiol. 2003;44: 1088–1099. doi:10.1093/pcp/pcg132

123. Yokota E, Shimmen T. The 135-kDa actin-bundling protein from lily pollen tubes arranges F-actin into bundles with uniform polarity. Planta. 1999;209: 264–266. doi:10.1007/s004250050631

124. Bachewich C, Heath IB. Radial F-actin arrays precede new hypha formation in Saprolegnia: implications for establishing polar growth and regulating tip morphogenesis. J Cell Sci. 1998;111: 2005–16. Available: http://www.ncbi.nlm.nih.gov/pubmed/9645948

125. Yang S, Huang FK, Huang J, Chen S, Jakoncic J, Leo-Macias A, et al. Molecular mechanism of fascin function in filopodial formation. J Biol Chem.

2013;288: 274–284. doi:10.1074/jbc.M112.427971

126. Tojkander S, Gateva G, Schevzov G, Hotulainen P, Naumanen P, Martin C, et al. A molecular pathway for myosin II recruitment to stress fibers. Curr Biol. Elsevier Ltd; 2011;21: 539–550. doi:10.1016/j.cub.2011.03.007

127. Verkhovsky AB, Borisy GG. Non-sarcomeric mode of myosin II organization in the fibroblast lamellum. J Cell Biol. 1993;123: 637–652.

128. Reymann A-C, Boujemaa-Paterski R, Martiel J-L, Guerin C, Cao W, Chin HF, et al. Actin Network Architecture Can Determine Myosin Motor Activity. Science (80-). 2012;336: 1310–1314. doi:10.1126/science.1221708

129. Vicente-Manzanares M, Ma X, Adelstein RS, Horwitz AR. Non-muscle myosin {II} takes centre stage in cell adhesion and migration. Nat Rev Mol Cell Biol. Nature Publishing Group; 2009;10: 778–790. doi:10.1038/nrm2786

130. Sayyad W a., Amin L, Fabris P, Ercolini E, Torre V. The role of myosin-II in force generation of DRG filopodia and lamellipodia. Sci Rep. 2015;5: 7842. doi:10.1038/srep07842

131. Cramer LP, Siebert M, Mitchison TJ. Identification of novel graded polarity actin filament bundles in locomoting heart fibroblasts: Implications for the generation of motile force. J Cell Biol. 1997;136: 1287–1305. doi:10.1083/jcb.136.6.1287

132. Laporte D, Ojkic N, Vavylonis D, Wu J-Q. α-Actinin and fimbrin cooperate with myosin II to organize actomyosin bundles during contractile-ring assembly. Mol Biol Cell. 2012;23: 3094–3110. doi:10.1091/mbc.E12-02-0123

133. Craig EM, Dey S, Mogilner A. The emergence of sarcomeric , graded-polarity and spindle-like patterns in bundles of short cytoskeletal polymers and two opposite molecular motors. J Phys Condens Matter. 2011;23: 3741021–10. doi:10.1088/0953-8984/23/37/374102

134. Kruse K, Jülicher F. Actively contracting bundles of polar filaments. Phys Rev Lett. 2000;85: 1778–1781. doi:10.1103/PhysRevLett.85.1778

135. Kruse K, Jülicher F. Self-organization and mechanical properties of active filament bundles. Phys Rev E - Stat Physics, Plasmas, Fluids, Relat Interdiscip Top. 2003;67: 16. doi:10.1103/PhysRevE.67.051913

136. Kreten FH, Hoffmann C, Riveline D, Kruse K. Active bundles of polar and bipolar filaments. Phys Rev E. American Physical Society; 2018;98: 012413. doi:10.1103/PhysRevE.98.012413

137. Zemel, Assaf, Mogilner A. Motor-induced sliding of microtubule and actin bundles. Phys Chem Chem Phys. 2009;11: 4800. doi:10.1039/b901646e

138. Dasanayake NL, Carlsson AE. Stress generation by myosin minifilaments in actin bundles. Phys Biol. 2013;10: 036006. doi:10.1088/1478-3975/10/3/036006

139. Bidone TC, Jung W, Maruri D, Borau C, Kamm RD, Kim T. Morphological Transformation and Force Generation of Active Cytoskeletal Networks. PLoS Comput Biol. Public Library of Science; 2017;13. doi:10.1371/journal.pcbi.1005277

140. Verkhovsky AB, Svitkina TM, Borisy GG. Polarity sorting of actin filaments

in cytochalasin-treated fibroblasts. J Cell Sci. 1997;110 (Pt 1: 1693–1704.

141. Wilson CA, Tsuchida MA, Allen GM, Barnhart EL, Applegate KT, Yam PT, et al. Myosin II contributes to cell-scale actin network treadmilling through network disassembly. Nature. Nature Publishing Group; 2010;465: 373–377. doi:10.1038/nature08994

142. Fritzsche M, Lewalle A, Duke T, Kruse K, Charras G. Analysis of turnover dynamics of the submembranous actin cortex. Mol Biol Cell. 2013;24: 757–67. doi:10.1091/mbc.E12-06-0485

143. van Goor D, Hyland C, Schaefer AW, Forscher P. The role of actin turnover in retrograde actin network flow in neuronal growth cones. PLoS One. 2012;7. doi:10.1371/journal.pone.0030959

144. Bernstein BW, Bamburg JR. ADF/Cofilin: A functional node in cell biology. Trends Cell Biol. Elsevier Ltd; 2010;20: 187–195. doi:10.1016/j.tcb.2010.01.001

145. Bamburg JR, McGough A, Ono S. Putting a new twist on actin: ADF/cofilins modulate actin dynamics. Trends Cell Biol. 1999;9: 364–370. doi:10.1016/S0962-8924(99)01619-0

146. Bravo-Cordero JJ, Magalhaes MAO, Eddy RJ, Hodgson L, Condeelis J. Functions of cofilin in cell locomotion and invasion. Nat Rev Mol Cell Biol. Nature Publishing Group; 2013;14: 405–417. doi:10.1038/nrm3609

147. Shekhar S, Pernier J, Carlier M-F. Regulators of actin filament barbed ends at a glance. J Cell Sci. 2016;129: 1085–1091. doi:10.1242/jcs.179994

148. Chen H, Bernstein BW, Bamburg JR. Regulating actin-filament dynamics in vivo. Trends Biochem Sci. 2000;25: 19–23. doi:10.1016/S0968-0004(99)01511-X

149. Fritzsche M, Li D, Colin-York H, Chang VT, Moeendarbary E, Felce JH, et al. Self-organizing actin patterns shape membrane architecture but not cell mechanics. Nat Commun. 2017;8: 17–19. doi:10.1038/ncomms14347

150. Muller-Taubenberger A, Diez S, Bretschneider T, Anderson K, Gerisch G. Subsecond reorganization of the actin network in cell motility and chemotaxis. Proc Natl Acad Sci. 2005;102: 7601–7606. doi:10.1073/pnas.0408546102

151. Humphrey D, Duggan C, Saha D, Smith D, Käs J. Active fluidization of polymer networks through molecular motors. Nature. 2002;416: 413–416. doi:10.1038/416413a

152. Salbreux G, Charras G, Paluch E. Actin cortex mechanics and cellular morphogenesis. Trends Cell Biol. Elsevier Ltd; 2012;22: 536–545. doi:10.1016/j.tcb.2012.07.001

153. Kim T, Gardel ML, Munro ED. Determinants of fluidlike behavior and effective viscosity in cross-linked actin networks. Biophys J. Biophysical Society; 2014;106: 526–534. doi:10.1016/j.bpj.2013.12.031

154. Meyer RK, Aebi U. Bundling of actin filaments by alpha-actinin depends on its molecular length. J Cell Biol. 1990;110: 2013–2024. doi:10.1083/jcb.110.6.2013

155. Schaus TE, Taylor EW, Borisy GG. Self-organization of actin filament

orientation in the dendritic-nucleation/array-treadmilling model. Proc Natl Acad Sci U S A. 2007;104: 7086–7091. doi:10.1073/pnas.0701943104

156. Lin J. Divergence Measures Based on the Shannon Entropy. IEEE Trans Inf Theory. 1991;37: 145–151. doi:10.1109/18.61115

157. Defays D. An efficient algorithm for a complete link method. Comput J. 1977;20: 364–366. doi:10.1093/comjnl/20.4.364

158. Freedman SL, Hocky GM, Banerjee S, Dinner AR. Nonequilibrium phase diagrams for actomyosin networks. Soft Matter. Royal Society of Chemistry; 2018;14: 7740–7747. doi:10.1039/c8sm00741a

159. Freedman SL, Suarez C, Winkelman JD, Kovar DR, Voth GA, Dinner AR, et al. Mechanical and kinetic factors drive sorting of F-actin crosslinkers on bundles. bioRxiv. 2018; 493841. doi:10.1101/493841

160. Komianos JE, Papoian GA. Stochastic Ratcheting on a Funneled Energy Landscape Is Necessary for Highly Efficient Contractility of Actomyosin Force Dipoles. Phys Rev X. 2018;8: 0210061–16. doi:10.1103/PhysRevX.8.021006

161. Dobramysl U, Papoian GA, Erban R. Steric Effects Induce Geometric Remodeling of Actin Bundles in Filopodia. Biophys J. Biophysical Society; 2016;110: 2066–2075. doi:10.1016/j.bpj.2016.03.013

162. Heidemann SR, Kirschner MW. Aster formation in eggs of xenopus laevis. 1975;67: 105–117.

163. Mullins RD. Cytoskeletal mechanisms for breaking cellular symmetry. Cold

Spring Harb Perspect Biol. 2010;2: 1–17. doi:10.1101/cshperspect.a003392

164. Ennomani H, Letort G, Guérin C, Martiel JL, Cao W, Nédélec F, et al. Architecture and Connectivity Govern Actin Network Contractility. Curr Biol. 2016;26: 616–626. doi:10.1016/j.cub.2015.12.069

165. Backouche F, Haviv L, Groswasser D, Bernheim-Groswasser a. Active gels: dynamics of patterning and self-organization. Phys Biol. 2006;3: 264–73. doi:10.1088/1478-3975/3/4/004

166. Soares e Silva M, Depken M, Stuhrmann B, Korsten M, MacKintosh FC, Koenderink GH. Active multistage coarsening of actin networks driven by myosin motors. Proc Natl Acad Sci U S A. 2011;108: 9408–9413. doi:10.1073/pnas.1016616108

167. Takiguchi K. Heavy meromyosin induces sliding movements between antiparallel actin filaments. J Biochem. 1991;109: 520–7.

168. Arai R, Mabuchi I. F-actin ring formation and the role of F-actin cables in the fission yeast Schizosaccharomyces pombe. J Cell Sci. 2002;115: 887–898.

169. Dudin O, Bendezú FO, Groux R, Laroche T, Seitz A, Martin SG. A formin-nucleated actin aster concentrates cell wall hydrolases for cell fusion in fission yeast. J Cell Biol. 2015;208: 897–911. doi:10.1083/jcb.201411124

170. Tang H, Laporte D, Vavylonis D. Actin cable distribution and dynamics arising from cross-linking, motor pulling, and filament turnover. Mol Biol Cell. 2014;25: 3006–16. doi:10.1091/mbc.E14-05-0965

171. Reymann AC, Martiel JL, Cambier T, Blanchoin L, Boujemaa-Paterski R,

Théry M. Nucleation geometry governs ordered actin networks structures. Nat Mater. Nature Publishing Group; 2010;9: 827–832. doi:10.1038/nmat2855

172. Craig EM, Dey S, Mogilner A. The emergence of sarcomeric, graded-polarity and spindle-like patterns in bundles of short cytoskeletal polymers and two opposite molecular motors. J Phys Condens Matter. 2011;23: 3741021–10. doi:10.1088/0953-8984/23/37/374102

173. Courson DS, Nagy S, Ricca BL, Smithback PA, Rock RS, Brawley CM, et al. A myosin motor that selects bundled actin for motility. Proc Natl Acad Sci. 2008;105: 9616–9620. doi:10.1073/pnas.0802592105

174. Lenartowska M, Michalska A. Actin filament organization and polarity in pollen tubes revealed by myosin II subfragment 1 decoration. Planta. 2008;228: 891–896. doi:10.1007/s00425-008-0802-5

175. Costa KD, Hucker WJ, Yin FCP. Buckling of actin stress fibers: A new wrinkle in the cytoskeletal tapestry. Cell Motil Cytoskeleton. 2002;52: 266–274. doi:10.1002/cm.10056

176. Alvarado J, Sheinman M, Sharma A, MacKintosh FC, Koenderink GH. Force percolation of contractile active gels. Soft Matter. 2017;13: 5624–5644. doi:10.1039/c7sm00834a

177. Weirich KL, Banerjee S, Dasbiswas K, Witten TA, Vaikuntanathan S, Gardel ML. Liquid behavior of cross-linked actin bundles. Proc Natl Acad Sci U S A. 2017;114: 2131–2136. doi:10.1073/pnas.1616133114

178. Weirich KL, Dasbiswas K, Witten TA, Vaikuntanathan S, Gardel ML. Self-

organizing motors divide active liquid droplets. Proc Natl Acad Sci U S A. 2019;166: 11125–11130. doi:10.1073/pnas.1814854116

179. Bendix PM, Koenderink GH, Cuvelier D, Dogic Z, Koeleman BN, Brieher WM, et al. A Quantitative Analysis of Contractility in Active Cytoskeletal Protein Networks. Biophys J. Elsevier; 2008;94: 3126–3136. doi:10.1529/biophysj.107.117960

180. Koenderink GH, Paluch EK. Architecture shapes contractility in actomyosin networks. Curr Opin Cell Biol. Elsevier Ltd; 2018;50: 79–85. doi:10.1016/j.ceb.2018.01.015

181. Soares E Silva M, Depken M, Stuhrmann B, Korsten M, MacKintosh FC, Koenderink GH. Active multistage coarsening of actin networks driven by myosin motors. Proc Natl Acad Sci U S A. 2011;108: 9408–9413. doi:10.1073/pnas.1016616108

182. Stam S, Freedman SL, Banerjee S, Weirich KL, Dinner AR, Gardel ML. Filament rigidity and connectivity tune the deformation modes of active biopolymer networks. Proc Natl Acad Sci U S A. 2017;114: E10037–E10045. doi:10.1073/pnas.1708625114

183. Schaller V, Schmoller KM, Karaköse E, Hammerich B, Maier M, Bausch AR. Crosslinking proteins modulate the self-organization of driven systems. Soft Matter. 2013;9: 7229–7233. doi:10.1039/c3sm50506e

184. Alvarado J, Sheinman M, Sharma A, Mackintosh FC, Koenderink GH. Molecular motors robustly drive active gels to a critically connected state. Nat

Phys. 2013;9: 591–597. doi:10.1038/nphys2715

185. Viamontes J, Tang JX. Continuous isotropic-nematic liquid crystalline transition of F-actin solutions. Phys Rev E - Stat Physics, Plasmas, Fluids, Relat Interdiscip Top. 2003;67: 4. doi:10.1103/PhysRevE.67.040701

186. Oakes PW, Viamontes J, Tang JX. Growth of tactoidal droplets during the first-order isotropic to nematic phase transition of F-actin. Phys Rev E - Stat Nonlinear, Soft Matter Phys. 2007;75: 1–11. doi:10.1103/PhysRevE.75.061902

187. Coppin CM, Leavis PC. Quantitation of liquid-crystalline ordering in F-actin solutions. Biophys J. 1992;63: 794–807. doi:10.1016/S0006-3495(92)81647-8

188. Alvarado J, Mulder BM, Koenderink GH. Alignment of nematic and bundled semiflexible polymers in cell-sized confinement. Soft Matter. 2014;10: 2354–2364. doi:10.1039/c3sm52421c

189. Falzone TT, Lenz M, Kovar DR, Gardel ML. Assembly kinetics determine the architecture of α-actinin crosslinked F-actin networks. Nat Commun. Nature Publishing Group; 2012;3: 861. doi:10.1038/ncomms1862

190. Lieleg O, Kayser J, Brambilla G, Cipelletti L, Bausch AR. Slow dynamics and internal stress relaxation in bundled cytoskeletal networks. Nat Mater. Nature Publishing Group; 2011;10: 236–242. doi:10.1038/nmat2939

191. Lieleg O, Claessens MM a. E, Bausch AR. Structure and dynamics of cross-linked actin networks. Soft Matter. 2010;6: 218. doi:10.1039/b912163n

192. Mulla Y, Mackintosh FC, Koenderink GH. Origin of Slow Stress Relaxation in the Cytoskeleton. Phys Rev Lett. American Physical Society; 2019;122:

218102. doi:10.1103/PhysRevLett.122.218102

193. Mulla Y, Wierenga H, Alkemade C, Ten Wolde PR, Koenderink GH. Frustrated binding of biopolymer crosslinkers. Soft Matter. Royal Society of Chemistry; 2019;15: 3036–3042. doi:10.1039/c8sm02429d

194. Mulla Y, Koenderink GH. Crosslinker mobility weakens transient polymer networks. Phys Rev E. American Physical Society; 2018;98: 1–8. doi:10.1103/PhysRevE.98.062503

195. Lenz M, Gardel ML, Dinner AR. Requirements for contractility in disordered cytoskeletal bundles. New J Phys. 2012;14. doi:10.1088/1367-2630/14/3/033037

196. Mullins RD, Heuser JA, Pollard TD. The interaction of Arp2/3 complex with actin: Nucleation, high affinity pointed end capping, and formation of branching networks of filaments. Proc Natl Acad Sci. 1998;95: 6181–6186. doi:10.1073/pnas.95.11.6181

197. Pollitt AY, Insall RH. WASP and SCAR/WAVE proteins: The drivers of actin assembly. J Cell Sci. 2009;122: 2575–2578. doi:10.1242/jcs.023879

198. Molinie N, Gautreau A. The Arp2/3 regulatory system and its deregulation in cancer. Physiol Rev. 2018;98: 215–238. doi:10.1152/physrev.00006.2017

199. Rotty JD, Wu C, Bear JE. New insights into the regulation and cellular functions of the ARP2/3 complex. Nat Rev Mol Cell Biol. Nature Publishing Group; 2013;14: 7–12. doi:10.1038/nrm3492

200. Swaney KF, Li R. Function and regulation of the Arp2/3 complex during cell

migration in diverse environments. Curr Opin Cell Biol. Elsevier Ltd; 2016;42: 63–72. doi:10.1016/j.ceb.2016.04.005

201. Ni Q, Papoian GA. Turnover versus Treadmilling in Actin Network Assembly and Remodeling. Cytoskeleton. Wiley Online Library; 2019;

202. Liman J, Bueno C, Eliaz Y, Schafer NP, Neal Waxham M, Wolynes PG, et al. The role of the Arp2/3 complex in shaping the dynamics and structures of branched actomyosin networks. Proc Natl Acad Sci U S A. 2020;117: 10825–10831. doi:10.1073/pnas.1922494117

203. Fujiwara I, Suetsugu S, Uemura S, Takenawa T, Ishiwata S. Visualization and force measurement of branching by Arp2/3 complex and N-WASP in actin filament. Biochem Biophys Res Commun. 2002;293: 1550–1555. doi:10.1016/S0006-291X(02)00421-7

204. Pandit NG, Cao W, Bibeau J, Johnson-chavarria EM, Taylor EW. Force and phosphate release from Arp2 / 3 complex promote dissociation of actin filament branches. Proc Natl Acad Sci. 2020; doi:10.1073/pnas.1911183117

205. Mahaffy RE, Pollard TD. Kinetics of the formation and dissociation of actin filament branches mediated by Arp2/3 complex. Biophys J. Elsevier; 2006;91: 3519–3528. doi:10.1529/biophysj.106.080937

206. Paciolla M, Arismendi-Arrieta DJ, Moreno AJ. Coarsening kinetics of complex macromolecular architectures in bad solvent. Polymers (Basel). 2020;12: 1–20. doi:10.3390/polym12030531

207. Testard V, Berthier L, Kob W. Intermittent dynamics and logarithmic domain

growth during the spinodal decomposition of a glass-forming liquid. J Chem Phys. 2014;140. doi:10.1063/1.4871624

208. Hu S, Dasbiswas K, Guo Z, Tee YH, Thiagarajan V, Hersen P, et al. Long-range self-organization of cytoskeletal myosin II filament stacks. Nat Cell Biol. 2017;19: 133–141. doi:10.1038/ncb3466

209. Soares E Silva M, Depken M, Stuhrmann B, Korsten M, MacKintosh FC, Koenderink GH. Active multistage coarsening of actin networks driven by myosin motors. Proc Natl Acad Sci U S A. 2011;108: 9408–9413. doi:10.1073/pnas.1016616108

210. Araújo SJ, Tear G. Axon guidance mechanisms and molecules: Lessons from invertebrates. Nat Rev Neurosci. 2003;4: 910–922. doi:10.1038/nrn1243

211. Dent EW, Gupton SL, Gertler FB. The Growth Cone Cytoskeleton in Axon outgrowth and guidance.pdf. Cold Spring Harb Perspect Biol. 2011;3: 1–40. doi:10.1101/cshperspect.a001800

212. Huber AB, Kolodkin AL, Ginty DD, Cloutier JF. Signaling at the growth cone: Ligand-receptor complexes and the control of axon growth and guidance. Annu Rev Neurosci. 2003;26: 509–563. doi:10.1146/annurev.neuro.26.010302.081139

213. Feinstein J, Ramkhelawon B. Netrins & Semaphorins: Novel regulators of the immune response. Biochim Biophys Acta - Mol Basis Dis. 2017;1863: 3183–3189. doi:10.1016/j.bbadis.2017.09.010

214. Hinck L. The versatile roles of “axon guidance” cues in tissue morphogenesis.

Dev Cell. 2004;7: 783–793. doi:10.1016/j.devcel.2004.11.002

215. Seiradake E, Jones EY, Klein R. Structural Perspectives on Axon Guidance. Annual Review of Cell and Developmental Biology. 2016. doi:10.1146/annurev-cellbio-111315-125008

216. Gallo G, Letourneau PC. Regulation of Growth Cone Actin Filaments by Guidance Cues. J Neurobiol. 2004;58: 92–102. doi:10.1002/neu.10282

217. Giniger E. How do Rho family GTPases direct axon growth and guidance? A proposal relating signaling pathways to growth cone mechanics. Differentiation. International Society of Differentiation; 2002;70: 385–396. doi:10.1046/j.1432-0436.2002.700801.x

218. Turney SG, Ahmed M, Chandrasekar I, Wysolmerski RB, Goeckeler ZM, Rioux RM, et al. Nerve growth factor stimulates axon outgrowth through negative regulation of growth cone actomyosin restraint of microtubule advance. Mol Biol Cell. 2016;27: 500–517. doi:10.1091/mbc.E15-09-0636

219. Kahn OI, Baas PW. Microtubules and Growth Cones: Motors Drive the Turn. Trends Neurosci. Elsevier Ltd; 2016;39: 433–440. doi:10.1016/j.tins.2016.04.009

220. Witte H, Bradke F. The role of the cytoskeleton during neuronal polarization. Curr Opin Neurobiol. 2008;18: 479–487. doi:10.1016/j.conb.2008.09.019

221. Strasser GA, Rahim NA, Vanderwaal KE, Gertler FB, Lanier LM. Arp2/3 is a negative regulator of growth cone translocation. Neuron. 2004;43: 81–94. doi:10.1016/j.neuron.2004.05.015

222. Tamariz E, Varela-Echavarría A. The discovery of the growth cone and its influence on the study of axon guidance. Front Neuroanat. 2015;9: 1–9. doi:10.3389/fnana.2015.00051

223. Lowery LA, Vactor D Van. The trip of the tip: Understanding the growth cone machinery. Nat Rev Mol Cell Biol. 2009;10: 332–343. doi:10.1038/nrm2679

224. O'Connor TP, Duerr JS, Bentley D. Pioneer growth cone steering decisions mediated by single filopodial contacts in situ. J Neurosci. 1990;10: 3935–3946. doi:10.1523/jneurosci.10-12-03935.1990

225. Clarke A, McQueen PG, Fang HY, Kannan R, Wang V, McCreedy E, et al. Dynamic morphogenesis of a pioneer axon in Drosophila and its regulation by Abl tyrosine kinase. Mol Biol Cell. 2020;31: 452–465. doi:10.1091/mbc.E19-10-0563

226. Grabham PW, Reznik B, Goldberg DJ. Microtubule and Rac 1-depen- dent F-actin in growth cones. J. J Cell Sci. 2003;116: 3739–3748. doi:10.1242/jcs.00686

227. Omotade OF, Pollitt SL, Zheng JQ. Actin-based growth cone motility and guidance. Mol Cell Neurosci. Elsevier Inc.; 2017;84: 4–10. doi:10.1016/j.mcn.2017.03.001

228. Jones SB, Lu HY, Lu Q. Abl tyrosine kinase promotes dendrogenesis by inducing actin cytoskeletal rearrangements in cooperation with Rho family small GTPases in hippocampal neurons. J Neurosci. 2004;24: 8510–8521. doi:10.1523/JNEUROSCI.1264-04.2004

229. Clarke A, McQueen PG, Fang HY, Kannan R, Wang V, McCreedy E, et al. Abl signaling directs growth of a pioneer axon in Drosophila by shaping the intrinsic fluctuations of actin. Mol Biol Cell. 2020;31: 466–477. doi:10.1091/mbc.E19-10-0564

230. Kannan R, Song J-K, Karpova T, Clarke A, Shivalkar M, Wang B, et al. The Abl pathway bifurcates to balance Enabled and Rac signaling in axon patterning in Drosophila. Development. 2017;144: 487–498. doi:10.1242/dev.143776

231. Kannan R, Giniger E. New perspectives on the roles of Abl tyrosine kinase in axon patterning. Fly (Austin). Taylor & Francis; 2017;0: 1–11. doi:10.1080/19336934.2017.1327106

232. Ni Q. Turnover Dynamics of Dendritic Actin Networks In Silico. 2016; Available: http://www.cpe.rutgers.edu/q-bio/docs/Qin-Ni.pdf

233. Li X, Ni Q, He X, Kong J, Lim S-M, Papoian GA, et al. Tensile force-induced cytoskeletal remodeling: Mechanics before chemistry. PLOS Comput Biol. 2020;16: e1007693. doi:10.1371/journal.pcbi.1007693

234. Eliaz Y, Nedelec F, Morrison G, Levine H, Cheung MS. Insights from graph theory on the morphologies of actomyosin networks with multilinkers. Phys Rev E. American Physical Society; 2020;102: 1–14. doi:10.1103/PhysRevE.102.062420

235. Floyd C, Papoian GA, Jarzynski C. Quantifying Dissipation in Actomyosin Networks. 2019; doi:10.1016/j.bpj.2018.11.1383

236. Blondel VD, Guillaume JL, Lambiotte R, Lefebvre E. Fast unfolding of communities in large networks. J Stat Mech Theory Exp. 2008;2008. doi:10.1088/1742-5468/2008/10/P10008

237. Linsmeier I, Banerjee S, Oakes PW, Jung W, Kim T, Murrell MP. Disordered actomyosin networks are sufficient to produce cooperative and telescopic contractility. Nat Commun. Nature Publishing Group; 2016;7: 12615. doi:10.1038/ncomms12615

238. Gateva G, Tojkander S, Koho S, Carpen O, Lappalainen P. Palladin promotes assembly of non-contractile dorsal stress fibers through VASP recruitment. J Cell Sci. 2014;127: 1887–1898. doi:10.1242/jcs.135780

239. Lecuit T, Lenne P-F, Munro E. Force Generation, Transmission, and Integration during Cell and Tissue Morphogenesis. Annu Rev Cell Dev Biol. 2011;27: 157–184. doi:10.1146/annurev-cellbio-100109-104027

240. Iber D, Campbell ID. Integrin activation - The importance of a positive feedback. Bull Math Biol. 2006;68: 945–956. doi:10.1007/s11538-005-9049-5

241. Parsons JT. Focal adhesion kinase: the first ten years. J Cell Sci. 2003;116: 1409–1416. doi:10.1242/jcs.00373

242. Kuramoto Y. Effects of Diffusion on the Fluctuations in Open Chemical Systems. Progress Theor Phys. 1974;52: 711–713. doi:10.1143/PTP.52.711

243. Kampen VNG. Fluctuations in continuous systems. AIP Conf Proc. 1976;27: 153–186. doi:10.1063/1.30357

244. Kampen VNG. The equilibrium distribution of a chemical mixture. Phys Lett

A. 1976;59: 333–334. doi:10.1016/0375-9601(76)90398-4

245. Lecca P, Laurenzi I, Jordan F. Deterministic Versus Stochastic Modelling in Biochemistry and Systems Biology [Internet]. Deterministic Versus Stochastic Modelling in Biochemistry and Systems Biology. 2013. doi:10.1533/9781908818218.348

246. Verkhovsky AB, Svitkina TM, Borisy Gary G. Myosin II filament assemblies in the active lamella of fibroblasts their morphogenesis and role in the formation of actin filament bundles. J Cell Biol. 1995;131: 989–1002.

247. Kurtz TG. The Relationship between Stochastic and Deterministic Models for Chemical Reactions. J Chem Phys. 1972;57: 2976. doi:10.1063/1.1678692

248. Gardiner CW. Handbook of stochastic methods. The effects of brief mindfulness intervention on acute pain experience: An examination of individual difference. 2015. doi:10.1017/CBO9781107415324.004

249. McQuarrie DA. Stochastic approach to chemical kinetics. J Appl Probab. 1967;4: 413–478. doi:10.2307/3212214

250. Gillespie DT. A general method for numerically simulating the stochastic time evolution of coupled chemical reactions. J Comput Phys. 1976;22: 403–434. doi:10.1016/0021-9991(76)90041-3

251. Kovács M, Wang F, Hu A, Zhang Y, Sellers JR. Functional divergence of human cytoplasmic myosin II. Kinetic characterization of the non-muscle IIA isoform. J Biol Chem. 2003;278: 38132–38140. doi:10.1074/jbc.M305453200

252. Stam S, Alberts J, Gardel ML, Munro E. Isoforms confer characteristic force

generation and mechanosensation by myosin II filaments. Biophys J. Biophysical Society; 2015;108: 1997–2006. doi:10.1016/j.bpj.2015.03.030

253. Hill A V. The possible effects of the aggregation of the molecule of hemoglobin on its dissociation curves. J Physiol. 1910;40: iv–vii. doi:10.1017/CBO9781107415324.004

254. Wachsstock DH, Schwartz WH, Pollard TD. Affinity of alpha-actinin for actin determines the structure and mechanical properties of actin filament gels. Biophys J. 1993;65: 205–14. doi:10.1016/S0006-3495(93)81059-2

255. Murphy CT, Rock RS, Spudich J a. A myosin II mutation uncouples ATPase activity from motility and shortens step size. Nat Cell Biol. 2001;3: 311–315. doi:10.1038/35060110

256. Vilfan A, Duke T. Instabilities in the transient response of muscle. Biophys J. 2003;85: 818–827. doi:10.1016/S0006-3495(03)74522-6

257. Billington N, Wang A, Mao J, Adelstein RS, Sellers JR. Characterization of three full-length human nonmuscle myosin II paralogs. J Biol Chem. Â© 2013 ASBMB. Currently published by Elsevier Inc; originally published by American Society for Biochemistry and Molecular Biology.; 2013;288: 33398–33410. doi:10.1074/jbc.M113.499848

258. Niederman R, Pollard TD. Human Platelet Myosin II . In Vitro Assembly and Structure of Myosin Filaments Formation of Platelet Myosin and Myosin Rod Filaments Determination of Platelet Myosin Solubility. J Cell Biol. 1975;67: 72–92.

259. Ferrer JM, Lee H, Chen J, Pelz B, Nakamura F, Kamm RD, et al. Measuring molecular rupture forces between single actin filaments and actin-binding proteins. Proc Natl Acad Sci U S A. 2008;105: 9221–6. doi:10.1073/pnas.0706124105

260. Footer MJ, Kerssemakers JWJ, Theriot JA, Dogterom M. Direct measurement of force generation by actin filament polymerization using an optical trap. Proc Natl Acad Sci. National Acad Sciences; 2007;104: 2181–2186.

261. Didonna BA, Levine AJ. Unfolding cross-linkers as rheology regulators in F-actin networks. Phys Rev E - Stat Nonlinear, Soft Matter Phys. 2007;75: 1–10. doi:10.1103/PhysRevE.75.041909